

CORTICAL CONTROL OF FORELIMB AND LINGUAL KINEMATIC PRIMITIVES IN
MICE

A Dissertation

Presented to the Faculty of the Graduate School
of Cornell University

In Partial Fulfillment of the Requirements for the Degree of
Doctor of Philosophy

by

Teja Pratap Bollu

May, 2020

© 2020 Teja Pratap Bollu

CORTICAL CONTROL OF FORELIMB AND LINGUAL KINEMATIC PRIMITIVES IN MICE

Teja Pratap Bollu, Ph.D.

Cornell University 2020

Motor sequences are constructed from primitives, hypothesized building blocks of movement, but mechanisms of primitive generation remain unclear. To dissect the neural circuits underlying generation of movement primitives, I designed two behavioral paradigms for mice.

First, using a novel forelimb sensor, I trained freely-moving mice to initiate forelimb sequences with clearly resolved submillimeter-scale micromovements followed by millimeter-scale reaches to learned spatial targets. Hundreds of thousands of trajectories were decomposed into millions of kinematic primitives, while closed-loop photoinhibition was used to test roles of motor cortical areas. Second, I imaged the mouse tongue at 1kHz during a cued directional lick task, and using a novel deep-learning based artificial neural network for semantic segmentation we resolved tens of thousands of mouse tongue trajectories with a precision of $\sim 60\mu\text{m}$. Cue-evoked licks exhibited previously unobserved fine-scale movements which, like a hand searching for an unseen object, were produced after misses and were directionally biased towards remembered locations.

Photoinhibition of contralateral “forelimb” motor cortex (CFA) during the forelimb task and bilateral “tongue” motor cortex (ALM) in a directional licking task led to both shared and distinct phenotypes. Inactivations reduced peak speed and pathlengths of primitives in both tongue and forelimb trajectories. However, while CFA inactivations did not substantially affect primitive direction, termination, or complexity, resulting in isomorphic, spatially contracted forelimb

trajectories. ALM inactivations specifically abolished the fine-scale adjustments in the tongue trajectories, reducing the complexity of movements. These findings identify conditions where loss of motor cortical drive leads to distinct behavioral deficits. The combination of high precision forelimb and tongue kinematics with automated training and neural manipulation provides a system for studying how motor sequences are constructed from elemental building blocks.

BIOGRAPHICAL SKETCH

Teja Pratap Bollu was born to Venkateswara Rao and Padmalekha Bollu in Tenali, Andhra Pradesh, India in 1988. Teja grew up in Bangalore, Karnataka and Secunderabad, Andhra Pradesh and graduated from Kendriya Vidyalaya, Picket in 2005. Teja earned his Bachelor of Technology degree from Vellore Institute of Technology, Vellore, Tamil Nadu, India. He majored in Electronics and Communication Engineering with a focus on biomedical signal processing. In 2013 he graduated with a Master's of Engineering in Biomedical Engineering from Cornell University, where he performed the mathematical modelling of blood flow in the microvasculature of the brain under the supervision of Dr. Chris Schaffer and Dr. Peter Doerschuk. In 2014 he began his doctoral studies at Department of Neurobiology and Behavior, Cornell University. He has since been conducting research in the laboratory of Dr. Jesse Goldberg on the mechanisms underlying the neural control of movement.

Dedicated to my parents who always encouraged me to ask ‘why?’, and to Laura who has become my ‘why’.

ACKNOWLEDGMENTS

This thesis would not have been possible without the kindness, support and guidance of many people. First, I would like first thank my doctoral advisor and mentor, Jesse Goldberg. Throughout my entire time at Cornell, Jesse has been an indefatigable champion for me and my work. Jesse's enthusiasm for science is infectious, his commitment to his trainees undeniable, and finally, his zeal and passion for understanding is something I aspire to. I have been incredibly fortunate to have a mentor like Jesse.

I would like to thank the members of my doctoral committee Joe Fetcho, Melissa Warden and Itai Cohen for their constant guidance and for inspiring me to always think about framing and contextualizing my work as answers to the big mysteries of our natural world.

I would like to thank Sam Whitehead who has been an excellent and supportive collaborator and a joy to work with. I would like to thank all postdoctoral fellows and the graduate students in the Goldberg lab that I've had the privilege to work alongside with, including Vikram Gadagkar, Morgane Pidoux, Ruidong Chen, Pavel Puzerey, Andrea Roeser and Brendan Ito. I am also grateful for the excellent technicians and undergraduates who have contributed to these projects, including Tori Riccelli, Nikil Prasad, Jackson Walker, Raghav Subramaiam, Mei Liu and Brian Kardon. I would also like to thank the administrative staff at NBB, specifically Sandra Anderson, Kathie Ely and Sara Eddleman.

I am deeply grateful to Peter Doerschuk, Chris Schaffer and Nozomi Nishimura for their mentorship since I first arrived at Cornell. I am also grateful for the mentorship of Robert Raguso and Ron Harris-Warrick.

Thanks to the many friends and colleagues across the Cornell community who made Ithaca such a wonderful place for me. There are many people without whom living in Ithaca would have

been dull, including Alaric Young, Joel and Hannah Tripp, Irene Ballagh, Rose Tartarsky, Ryan Post, Akash Guru, Changwoo Seo, Joe Di Pietro, Hailey Scofield, Shane Peace, Mitch Pender, Jason Jones and many others.

Finally I would like to thank my family who have always been there for me and have supported me through the many ups and downs during my time in graduate school. Thank you to my parents who have constantly cared for me and put in an enormous amount of time and effort into my wellbeing. Thank you to my aunt and uncle, Srilakshmi and Venkata Atluri who were my rock of support since I first moved to the United States. My wife Laura has been an incredible and understanding partner throughout graduate school, she has been a source of great strength. Without her patience and heart, I would be adrift.

TABLE OF CONTENTS

Biographical sketch	iii
Dedication	iv
Acknowledgements	v
Table of Contents	vii
List of Figures	viii
List of Tables	x
List of Abbreviations	xi
Chapter 1 Introduction	
<i>Chapter Text</i>	1
<i>References</i>	3
Chapter 2 Motor cortex inactivation reduces gain of kinematic primitives in mice performing a center-out reach	
<i>Introduction</i>	4
<i>Results</i>	8
<i>Discussion</i>	30
<i>Materials and Methods</i>	38
<i>References</i>	53
<i>Appendix</i>	61
Chapter 3 Tongue kinematics reveal cortex dependent corrections as the mouse tongue reaches for, and misses, targets	
<i>Introduction</i>	89
<i>Results</i>	90
<i>Discussion</i>	103
<i>Methods</i>	106
<i>References</i>	115
<i>Appendix</i>	118
Chapter 4 Conclusion	
<i>Chapter Text</i>	133
<i>References</i>	142

LIST OF FIGURES

- Figure 2.1 Primate hand trajectories can be decomposed into kinematic primitives
- Figure 2.2 Automated homecage training of mice in a hold-still-center-out reach task.
- Figure 2.3 Mice learn hold-in-center requirement by producing decamicron-scale micromovements.
- Figure 2.4 Mice learn to reach to spatial targets
- Figure 2.5 The Shape of the stabilogram diffusion function (SDF) during the hold is largely preserved during cortical inactivations.
- Figure 2.6 Effect of cortical inactivations on trajectory kinematics.
- Figure 2.7 Effect of cortical inactivations on trajectory direction
- Figure 2.8 Motor cortical inactivations do not affect complexity of kinematic primitives.
- Figure 2.9 Effect of cortical inactivations on primitive kinematics.
- Figure 2.10 Primitive kinematic distributions from CFAc1 inactivated dataset can be transformed into intact distributions by a single multiplicative gain factor.
- Figure 2.S1 Mice learn to contact the joystick after the nosepoke.
- Figure 2.S2 Example trajectories forelimb trajectories.
- Figure 2.S3 Trajectory patterns exhibited by mice during all-directions-rewarded stage of training.
- Figure 2.S4 Effect of motor cortical inactivations on the ‘submovement’ class of kinematic primitives.
- Figure 2.S5 Segment pathlength is predicted by its peak speed
- Figure 2.S6 Impact of cortical inactivations on segment directions.
- Figure 3.1 Machine vision based tracking of lingual kinematics identifies intra-lick movements important for spout contact.

LIST OF FIGURES (continued)

- Figure 3.2. Photoinactivation of ALM impairs spout contact by abolishing intra-lick movements.
- Figure 3.3 Directionally biased tongue protrusions persist during ALM inactivation.
- Figure 3.4 Intra-lick movements are directionally biased towards remembered spout locations.
- Figure 3.S1 Method for extracting 3D tongue tip kinematics.
- Figure 3.S2 Water retrieval and cue-evoked licks exhibit distinct kinematics
- Figure 3.S3 Tongue tip positions at the moment of retraction onset and spout contact
- Figure 3.S4 The number of acceleration peaks per lick predicts latency to spout contact
- Figure 3.S5 Spout contact transforms the kinematics of subsequent licks.
- Figure 3.S6 Inactivation of PMM does not impact task performance or lick kinematics
- Figure 3.S7 ALM photoinhibition results in hypometric retrieval licks
- Figure 3.S8 Proximal spout placement rescues ALM inactivation-associated spout contact deficits

LIST OF TABLES

Table 2.1	Probability of a successful hold (LME)
Table 2.2	Slope of SDF function
Table 2.3	Transition point of SDF function
Table 2.4	Offsets of SDF function (log)
Table 2.5	Probability of transecting outer radius (4mm)
Table 2.6	Peak Speed of trajectories (mm/s)
Table 2.7	Angle of trajectory (degrees)
Table 2.8	StdDev of Reach Angle for trajectory
Table 2.9	Duration of segments (milliseconds)
Table 2.10	Peak speed of segments (mm/s)
Table 2.11	Path length of segments (mm)
Table 2.12	Segment direction
Table 2.13	Segment tortuosity
Table 2.14	Segment number of acceleration peaks
Table 2.15	Fraction of overlapping submovements (OSMs)
Table 2.16	Submovement duration
Table 2.17	Submovement velocity
Table 2.18	Submovement pathlength
Table 2.19	Submovement direction
Table 3.1	Kinematics of cue evoked and water retrieval licks
Table 3.2	Kinematics of cue evoked licks with ALM inactivation
Table 3.3	Kinematics of cue evoked licks with PMM inactivation
Table 3.4	Kinematics of retrieval licks with ALM inactivation
Table 3.5	Direction bias of ILM initial velocity vectors

LIST OF ABBREVIATIONS

CFA	Caudal Forelimb Area
RFA	Rostral Forelimb Area
SDF	Stabilogram Diffusion Function
ALM	Anterior Lateral Motor Cortex
PMM	Poster Medial Motor Cortex
ILM	Intra-Lick Movements

CHAPTER 1

INTRODUCTION

Virtually all human behaviors are acquired through the gradual process of trial-and-error learning. It has long been known that this involves generation of exploratory actions coupled with evaluation of the resulting performance, but it remains unknown how these processes are implemented in the brain. How do we try new things? How do we get better with practice? The main obstacle to addressing these questions is the multi-layered complexity of the mammalian motor system. It consists of a distributed group of interconnected brain regions, which in turn consist of specific cell types arranged in complex microcircuits. The rapid development of genetic tools has provided the ability to perturb precise neural populations and their projection targets in mammals (Gerfen et al., 2013). Identifying the specific roles of these neural populations requires complementary behavioral paradigms to specify the effects of perturbations (Krakauer et al., 2017).

In my dissertation work, I developed and characterized two high precision behavioral platforms to enable rapid interrogation of neural circuits responsible for forelimb and tongue movements. I subsequently used these platforms to identify the role of motor cortex in planning and executing skilled movements.

In Chapter 2, I describe the apparatus I developed to perform causal experiments that enables high throughput dissection of mammalian forelimb motor circuits, (1) I invented a joystick specifically for mice forepaws that has micron-millisecond precision (2) Developed a real-time, fully automated system with closed loop optogenetics to train mice in center-out reach task and (3) Developed the algorithms and analysis tools to analyze ~2 million trajectories from 11 mice. (Bollu et al., 2019b) Using this system, I identified the putative building blocks of forelimb movement called ‘kinematic primitives’ (Giszter, 2015), and showed that inactivation of the

forelimb motor cortex (CFA, for Caudal Forelimb Area) (Tennant et al., 2010) reduced the ‘gain’ of these primitives, while leaving the rest of the movement unaltered.

In Chapter 3, I describe efforts aimed at determining the generality of this discovery to tongue movements. Here I investigated if the motor cortex played a similar role in controlling a different effector, the mouse tongue. The tongue is a complex group of muscles capable of producing precisely timed and directed movements. Animals rely on this precision for vocalizations, prey capture, nectar extraction, echolocation, swallowing, food manipulation and licking. (Guenther, 1995; Kier and Smith, 1985). To record and characterize tongue movements, I combined kilohertz frame-rate imaging and a deep-learning based artificial neural network to track tongue kinematics at decamicrosecond, millisecond precision as mice performed a directed lick task (Bollu et al., 2019a). With this paradigm, I identified that mice exhibit at least two kinds of lingual movements, a) Dexterous exploratory movements that are variable, have complex speed profiles and are utilized for localizing the spout position and b) Consummatory movements that are highly stereotyped in time and are used to retrieve water from the spout. I showed that inactivation of a cortical area (ALM, Antero Lateral Motor Cortex) (Komiya et al., 2010) eliminates the exploratory movements and reduces the amplitude of all other movements.

Therefore, photoinhibition of contralateral “forelimb” motor cortex (CFA) during the forelimb task and bilateral “tongue” motor cortex (ALM) in a directional licking task led to shared and distinct phenotypes. Namely, photoinhibition of Motor Cortex across behavioral paradigms and effectors consistently showed a reduction in amplitude of the movements, consistent with loss of one of the many motor controllers as discussed in Chapter 2. However, photoinhibition of the motor cortex in the directed licking task led to a loss in exploratory movements in addition to the

reduction in amplitude of the movements. In Chapter 4, I discuss interpretations of these differences and propose experiments to reconcile these results.

The combination of high precision forelimb and tongue kinematics with automated training and neural manipulation provides a system for studying how motor sequences are constructed from elemental building blocks.

REFERENCES

- Bollu, T., Whitehead, S.C., Kardon, B., Redd, J., Liu, M.H., and Goldberg, J.H.J.b. (2019a). Tongue Kinematics. Cortex-dependent corrections as the mouse tongue reaches for, and misses, targets. 655852.
- Bollu, T., Whitehead, S.C., Prasad, N., Walker, J., Shyamkumar, N., Subramaniam, R., Kardon, B., Cohen, I., and Goldberg, J.H.J.o.n. (2019b). Automated home cage training of mice in a hold-still center-out reach task. 121, 500-512.
- Gerfen, C.R., Paletzki, R., and Heintz, N. (2013). GENSAT BAC cre-recombinase driver lines to study the functional organization of cerebral cortical and basal ganglia circuits. *Neuron* 80, 1368-1383.
- Giszter, S.F. (2015). Motor primitives--new data and future questions. *Curr Opin Neurobiol* 33, 156-165.
- Guenther, F.H. (1995). Speech sound acquisition, coarticulation, and rate effects in a neural network model of speech production. *Psychol Rev* 102, 594-621.
- Kier, W.M., and Smith, K.K. (1985). Tongues, tentacles and trunks: the biomechanics of movement in muscular-hydrostats. *Zoological journal of the Linnean Society* 83, 307-324.
- Komiyama, T., Sato, T.R., O'Connor, D.H., Zhang, Y.X., Huber, D., Hooks, B.M., Gabitto, M., and Svoboda, K. (2010). Learning-related fine-scale specificity imaged in motor cortex circuits of behaving mice. *Nature* 464, 1182-1186.
- Krakauer, J.W., Ghazanfar, A.A., Gomez-Marin, A., MacIver, M.A., and Poeppel, D.J.N. (2017). Neuroscience needs behavior: correcting a reductionist bias. 93, 480-490.
- Tennant, K.A., Adkins, D.L., Donlan, N.A., Asay, A.L., Thomas, N., Kleim, J.A., and Jones, T.A. (2010). The Organization of the Forelimb Representation of the C57BL/6 Mouse Motor Cortex as Defined by Intracortical Microstimulation and Cytoarchitecture. *Cerebral Cortex* 21, 865-876.

CHAPTER 2

MOTOR CORTICAL INACTIVATION REDUCES THE GAIN OF KINEMATIC PRIMITIVES IN MICE PERFORMING A HOLD-STILL CENTER-OUT REACH

Abstract

Motor sequences are constructed from primitives, hypothesized building blocks of movement, but mechanisms of primitive generation remain unclear. Using automated homecage training and a novel forelimb sensor, we trained freely-moving mice to initiate forelimb sequences with clearly resolved submillimeter-scale micromovements followed by millimeter-scale reaches to learned spatial targets. Hundreds of thousands of trajectories were decomposed into millions of kinematic primitives, while closed-loop photoinhibition was used to test roles of motor cortical areas. Inactivation of contralateral motor cortex reduced primitive peak speed but, surprisingly, did not substantially affect primitive direction, initiation, termination, or complexity, resulting in isomorphic, spatially contracted trajectories that undershot targets. Our findings demonstrate separable loss of a single kinematic parameter, speed, and identify conditions where loss of cortical drive reduces the gain of motor primitives but does not affect their generation, timing or direction. The combination of high precision forelimb sensing with automated training and neural manipulation provides a system for studying how motor sequences are constructed from elemental building blocks.

* Published in part as Bollu, T., Whitehead, S. C., Prasad, N., Walker, J., Shyamkumar, N., Subramaniam, R.,Kardon B.,Cohen, I., & Goldberg, J. H. (2019). Automated home cage training of mice in a hold-still center-out reach task. *Journal of neurophysiology*, 121(2), 500-512.

Introduction

An infamous problem in motor control is ‘the curse of dimensionality:’ a hand in motion sweeps through a near infinite continuum of possible trajectories, making motor control seem intractably

high-dimensional (Bernstein, 1967; Shadmehr and Wise, 2005; Woodworth, 1899). One solution is to construct movement from a discrete set of elementary building blocks, or motion primitives (Flash and Hochner, 2005; Mussa-Ivaldi et al., 1994). For example, when you draw the letter “N” you carve a complex path through space, but “N” can be decomposed into three distinct strokes, or kinematic primitives, each with only a few parameters such as direction, speed and duration (Flash and Hogan, 1985; Milner, 1992; Viviani and Terzuolo, 1982)(Figure 2.1A-C). Motor primitives are abnormally generated and sequenced in disorders such as stroke, dystonia and Parkinson’s (Desmurget et al., 2004; Inzelberg et al., 1995; Majsak et al., 1998; Rohrer et al., 2004), yet precise circuits that generate primitives, determine their kinematics, and sequence them into a trajectory are poorly understood (Giszter, 2015).

One challenge is that kinematic representations and initiation signals are not regionally localized but are instead distributed throughout cortical, cerebellar, and basal ganglia circuits (Fortier et al., 1989; Fu et al., 1997; Schwartz, 2007; Scott, 2003; Shenoy et al., 2013; Turner and Anderson, 1997; Wong et al., 2014), complicating the identification of structure-function relationships and motivating causal experiments to provide at least some constraints on theories of motor control (Omrani et al., 2017; Pruszynski et al., 2011; Wolff and Ölveczky, 2018). For example, two extreme and opposite views of primitive generation are both compatible with distributed kinematic representations. Distinct kinematic parameters could differentially depend on distinct and separable neural circuits (Favilla et al., 1989; Flanders and Soechting, 1990), in which case a regional brain inactivation could affect one specific parameter (e.g. speed) and not others (e.g. direction, duration). Alternatively, kinematic parameters could be encoded interdependently (Shenoy et al., 2013), in which case a regional inactivation could affect multiple kinematic parameters at once (Figure 2.1D-E).

Genetic tools in mice enable temporally precise circuit manipulations (Guo et al., 2014), but forelimb kinematics have not been analyzed to extract primitives as in Figure 2.1, in part because trajectory segmentation requires sensitivity to resolve the rapid, tiny details of motion that occur at sharp turns. To address this issue, we designed ultra-low torque touch- sensing joysticks that resolve mouse forelimb kinematics with micron-millisecond spatiotemporal resolution and built an automated homecage system to train mice in a hold-still-center-out reach task. To complete the task, mice learned to first actively maintain the joystick in a small center position and then to produce an outward reach to learned spatial targets. The resultant trajectories carved complex paths in space. Algorithms previously used in primates were effective in decomposing forelimb trajectories into kinematic primitives, enabling us to test hypotheses of primitive generation. Inactivation of contralateral motor cortex reduced the peak speeds of primitives of all magnitudes, but did not affect their direction, initiation, duration, or complexity. As a result, forelimb trajectories exhibited isomorphic hypometria, i.e. they retained their basic shapes but were spatially contracted, or ‘shrunk,’ as if your letter “N” was a miniaturized “N”.

Methodologically, we demonstrate the utility of an automated system for high-throughput dissection of neural circuits that control basic building blocks of forelimb movement in mice. Conceptually, our findings identify conditions where the loss of cortical drive reduces the gain of motor primitives.

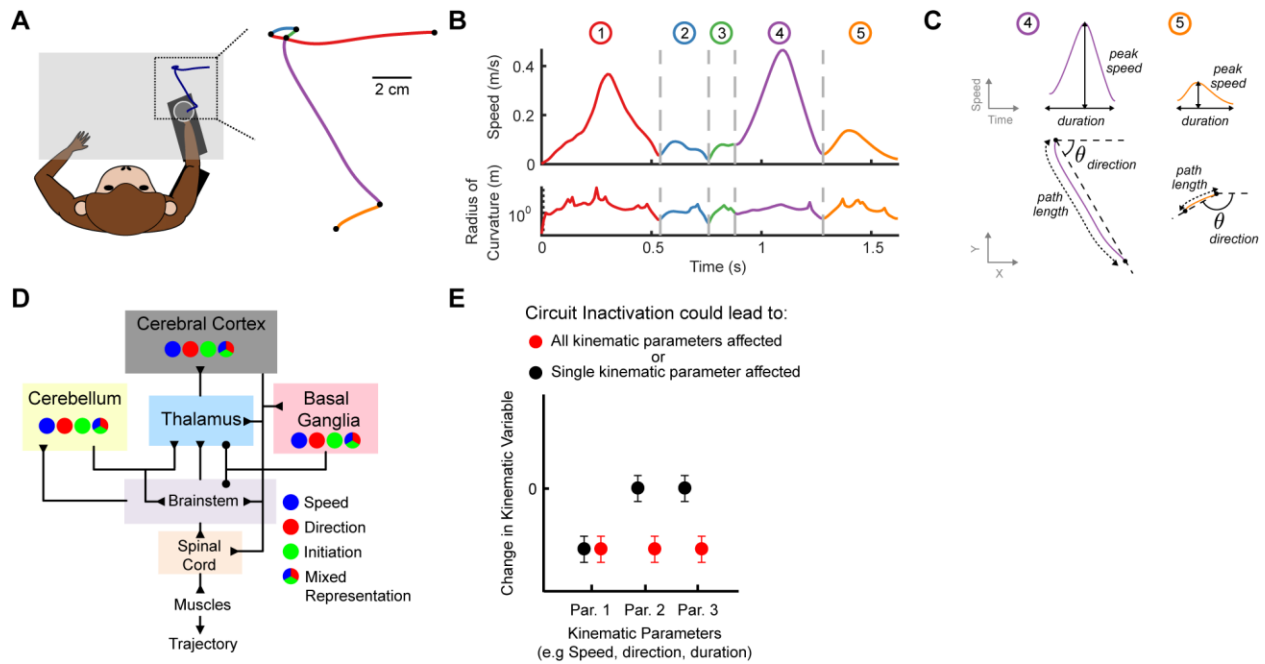


Figure 2.1. Primate hand trajectories can be decomposed into kinematic primitives. (A) Schematic of a hand trajectory during a sequential reach task (left) with primate kinematic data from a previous study (Gowda et al, 2015). Black dots denote boundaries separating discrete segments. (B). Speed (top) and radius of curvature (bottom) are plotted as a function of time in the trajectory from A. Segment boundaries (gray dashed lines) are detectable as temporally coincident minima. (C) The speed (top) and path (bottom) of the last two segments from the trajectory in A-B. Individual segments are described by kinematic parameters such as peak speed, duration, direction and pathlength. (D) Schematic of mammalian motor system, highlighting the existence of distributed kinematic representations. (E) Possible outcomes of inactivation experiments on primitive kinematics. Inactivation of a brain region could affect one (black) or multiple (red) kinematic parameters.

Results

A novel sensor quantifies mouse forelimb kinematics with micron-millisecond spatiotemporal precision

Joysticks can be used in rodents to resolve forelimb kinematics during reach tasks (Francis and Chapin, 2004; Kimura et al., 2012; Mathis et al., 2017; Miri et al., 2017; Morandell and Huber, 2017; Panigrahi et al., 2015; Sanders and Kepecs, 2012; Slutzky et al., 2010; Wagner et al., 2017). To obtain raw trajectory data suitable for decomposition into primitives, we implemented a novel joystick design to increase spatial precision, reduce displacement force and ensure an isometric force profile. We designed a capacitive touch-sensing joystick that used contactless magnetic field sensing to detect motion, endowing it with micron-scale resolution (Figure 2.2 A-D, average spatial resolution: 320 ± 35 nm, $n=5$ joysticks). We also replaced the standard two axis spring re-centering mechanism with a single pair of magnets, resulting in a stable, uniform force-displacement relationship and a 10-100 fold reduction in displacement force (Figure 2.2E, stiffness: 8.11 mN/mm (or 0.82 gf/mm), $r^2=0.99$, see Methods). These modifications were necessary to resolve tiny details of mouse forelimb motion for trajectory decomposition, as outlined in more detail below.

To stabilize body posture, the joystick was integrated into a narrow ‘reward port’ consisting of five parts: (1) The joystick, which detects right paw contact and x-y movements; (2) A touch-sensing fixed post positioned for the left paw; (3) two side-walls that constrain the animal’s body position and orientation; (4) an IR-sensing nosepoke; and (5) a solenoid-controlled water dispensation spout within tongue’s reach of the nosepoke sensor. The requirement that animals engage the joystick, fixed post, and nosepoke contacts constrained the animal’s posture and ensured joystick manipulation with the right forepaw (Figure 2.2F).

Automated homecage training of mice in a hold-still-center-out reach task

Automated training facilitates high-throughput experimentation on rodents in sophisticated learning tasks (Erlich et al., 2015; Murphy et al., 2016; Poddar et al., 2013; Woodard et al., 2017). We incorporated the joystick-reward port into rack-mountable, fully automated mouse homecages (Figure 2.2G-L). Mice enjoyed continuous, ad lib access to the joystick for their daily water, resulting in thousands of trajectories per animal per day (2792 ± 362 trials per day, mean \pm sem, $n=11$ animals). We built a three-stage signal processing system pipeline to automate training and data acquisition: (1) an FPGA implemented millisecond timescale real-time analysis of all sensors, including joystick position, for closed-loop control of reward dispensation and of laser pulses for optogenetic experiments; (2) a real-time processor implemented second-timescale analysis for selective acquisition of trajectory and sensor data associated with eligible trials; (3) a host PC implemented day-timescale analysis of recent joystick manipulation patterns for automated contingency updates underlying training (Figure 2.2H, see Methods, Supplemental Methods).

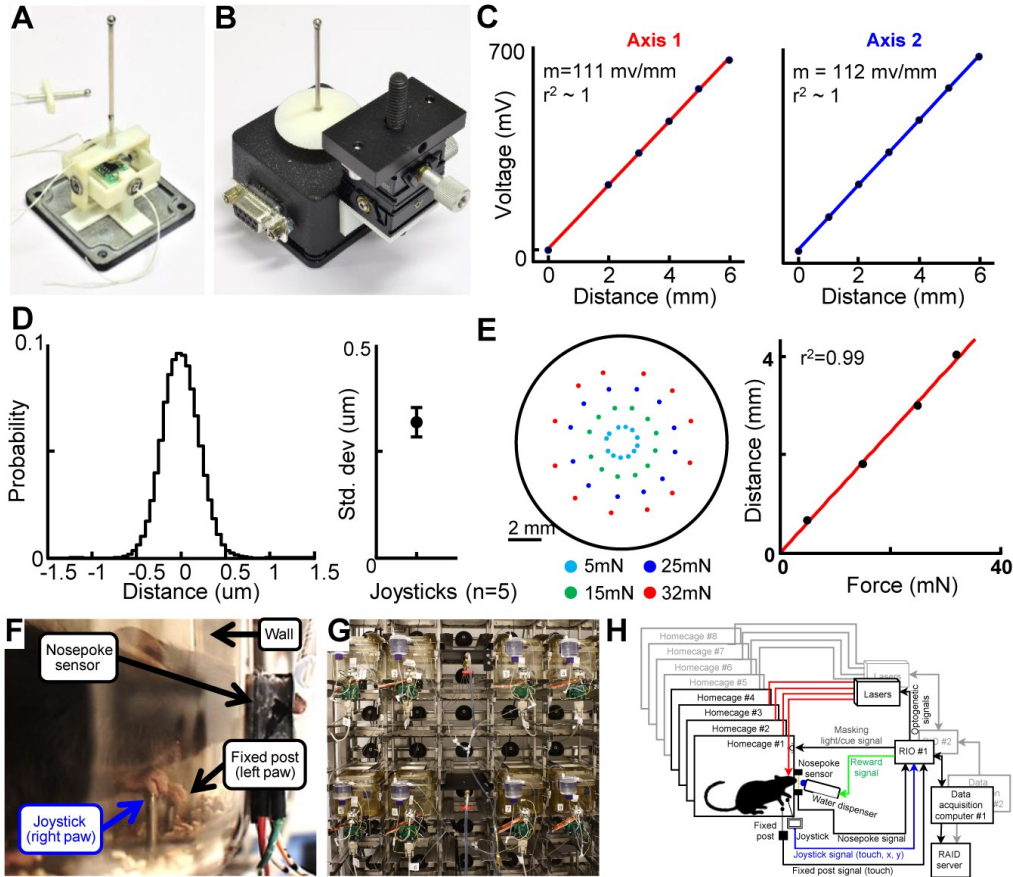
A sequence of fully automated reward contingency updates shaped right forelimb trajectories in a direction-specific center-out reach task (Figure 2.2I, see Methods). First, mice were trained to contact the joystick after the nosepoke and fixed-post to ensure that joystick movement was attributable to right paw (Figure 2.S1A,B). The timing of joystick contact became stereotyped with experience (Figure 2.S1C,D; joystick contact onset: 184 ± 14.5 ms after nosepoke; entropy of JS contact onset after nosepoke: 7.32 ± 0.13 (day 1) vs 7.05 ± 0.15 (criterion day), $p < 0.001$, paired t-test). Next mice were trained to hold the joystick within an inner radius of 2 mm for 100 milliseconds prior to reaching past an outer radius of 4 mm (Figure 2.2J). This ‘hold period,’ defined as the latency from joystick contact to the moment of inner-radius transection,

was implemented to study neural basis of maintaining stability and also to impose a delay in outward reaching that would allow for cortical photoinhibition to take effect before reach onset.

Mice learn to hold still before reaching out

Due to the joystick's low stiffness, the hold-in-center requirement approximates an inverted pendulum problem, in which a control policy is required to produce corrective micromovements to prevent rapid deviations from center position (Anderson, 1989; Bhounsule et al., 2015; Cabrera and Milton, 2002). Consistent with this, whereas early in training trajectories exhibited rapid displacements from the center position, later in training mice produced a clearly resolved sequence of 'micromovements' that maintained the joystick within the inner radius for longer periods of time (Figure 2.3 and Figure 2.S2) (Mean hold time: 57 ± 6 ms (first 100 trials) vs. $93 \text{ ms} \pm 14 \text{ ms}$ (at criterion), $p < 0.01$, $n = 11$ animals).

To test if micromovements produced during the 'hold' reflected an active control policy for maintaining position, we computed stabilogram diffusion functions (SDFs). SDFs plot mean square displacement for all pairs of points in a trajectory as a function of time interval Δt (Collins and De Luca, 1993; Peterka, 2000) (Methods, Figure 2.3H). This analysis effectively distinguishes between different types of motion. For example, the SDF of a classic random walk exhibits a slope of 1. Persistent motion biased towards increased time-dependent displacement exhibits a slope greater than 1. Finally, anti-persistent motion biased towards stabilizing position exhibits a slope less than 1 (Figure 2.3G). SDFs of trajectories acquired during the hold-period exhibited at least two regimes. At short latencies, the time-dependent displacement adhered to a



I

Day 1,2	3-4	5-6	8-11	12-15	15-21	21-31	31-37
Water spout acclimation	Contact joystick after nosepoke and post	Move joystick to outer threshold	'Hold' joystick in the middle before moving out	Set first reach angle rule	First CFA and RFA inactivations	Shape reach angle dist. to move by -60 deg	Second CFA and RFA inactivations

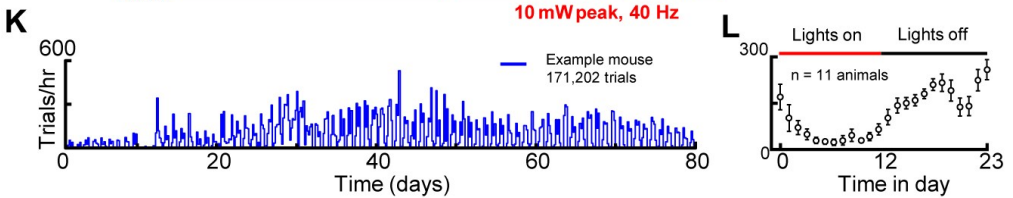
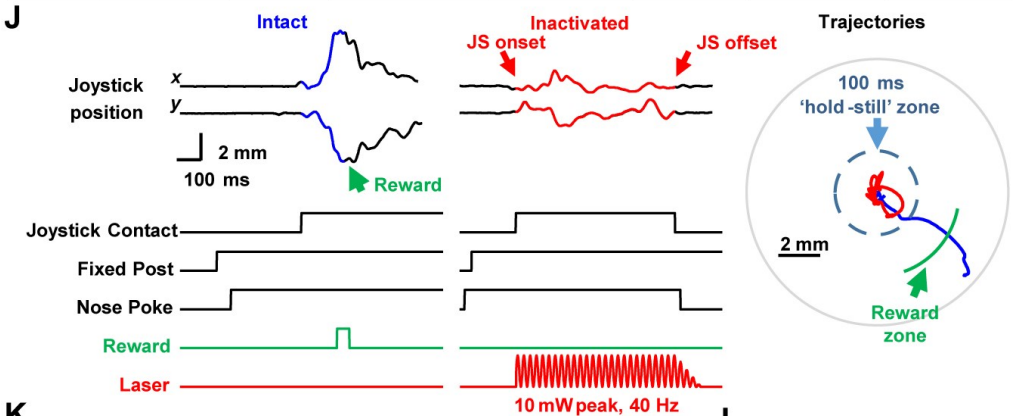


Figure 2.2. Automated homecage training of mice in a hold-still-center-out reach task. (A-E) Characterization of the joystick. (A-B) The joystick was a manipulandum capped with a capacitive touch sensor and mounted on a modified Gimbal assembly equipped with a 2-axis Hall sensor. (C-E) Hall sensor voltage measured as a function of distance across two non-orthogonal radial axes. (D) Spatial resolution characterization: measured probability distribution of a single joystick displacement for a single joystick (left) and mean \pm SEM standard deviation of the distribution across 5 joysticks (right). (E) Example of force-displacement characterization for a single joystick. Each dot indicates the measured displacement by a fixed force, color coded at bottom (left). Average joystick displacement as a function of force. (F) Still frame of mouse engaged in the task. (G) Photograph of homecage training room in mouse facility. (H) Schematic of signal processing pipeline for each homecage. (I) Timeline of behavioral shaping and photoinhibition experiments (J) Example trajectories and sensor data from a control (left) and CFAC1 inactivated (middle) trial. (K) Trials per hour exhibited by an example animal for 80 days. (L) Trials per hour as a function of time in day (mean \pm SEM, n=11 animals).

power law with a slope >1 (mean slope of log-log: 1.957 ± 0.0028), reflecting a regime of rapid deviations consistent with the absence of a corrective process at those latencies. A second mode appeared after a brief delay (mean transition point: 27.59 ± 1.56 ms), reflecting the onset of a distinct process that curtails deviations away from a position (Figure 2.3G). SDFs acquired during human standing exhibit a similar shape, with a transition point reflecting the onset of an active control process to maintain balance (Peterka, 2002). These findings suggest that an active control policy, potentially similar to one used during the distinct inverted pendulum problem of maintaining of upright balance, was implemented to achieve the hold-still component of the task.

Mice learn to reach in different rewarded directions

Once the contact, hold-still, and reach sequence was learned, all outward reach directions were rewarded, enabling each animal's natural reach direction and variability to be quantified (Figure 2.S3). Mice learned to execute the 'contact', 'hold-still' and reach sequence approximately one week after being placed into a homecage (Figure 2.3C-E, 8.5 ± 1.05 days, $n=11$ animals, see Methods). Reach directions, defined as the angle at which the outer radius was transected, were next rotated clockwise (CW) or counterclockwise (CCW) by contingency updates that rewarded the 15th (for CW) or 85th (for CCW) percentile of their reach direction distribution (Figure 2.4). All mice learned to change their reach directions commensurate with rewarded contingency changes and changed their reach direction at a rate of 6.8 ± 2.3 (CW) and 4.6 ± 1.46 (CCW) degrees/day (mean \pm sem) (Figure 2.4C-D).

Roles of different motor cortical areas in holding still and reaching to target locations

By design, our task structure resolved many aspects of movement: from posture-maintaining micromovements for holding still in center to larger amplitude reaches aimed at

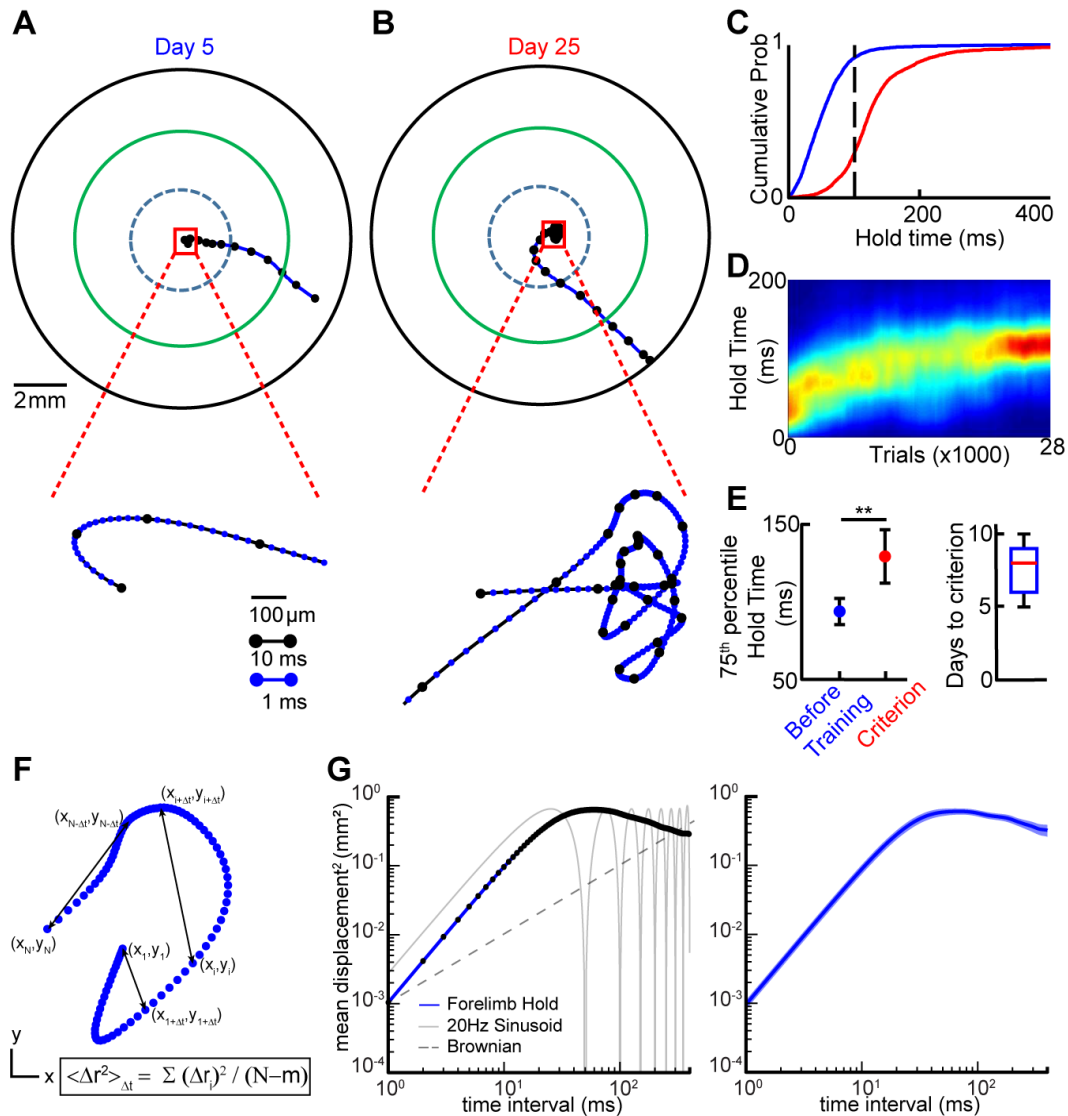


Figure 2.3. Mice learn hold-in-center requirement by producing decam micron-scale micromovements. (A) Example trajectory produced at day 5 since homepage introduction. Blue dashed circle indicates inner ‘hold’ region; green circle indicates reward zone; black circle indicates joystick boundaries. Black dots denote 10 millisecond intervals in the trajectory. Note distinct displacement scale bar for the expanded view of movement inside the hold region (bottom). (B) Data plotted as in A for a trajectory produced by the same mouse 20 days later. Expanded view at bottom plots details of micromovements produced to maintain hold requirement. (C) Cumulative probability of the hold time of trajectories before (blue) and after (red) training for the example mouse. (D) Heatmap showing the probability density plot of hold times as a function of trial number for the mouse show in in A-C. (E) 75th percentile hold-time before training and at

criterion for all mice (left), number of days to criterion (right) (data are mean \pm SEM across 11 animals). (F) Schematic describing calculation of the stabilogram diffusion function (SDF) of a short trajectory segment (G) Example SDF from a single animal (left, blue line) and across all animals (right; n=7, line and shading represent mean \pm SEM of SDF). Example SDF's of a purely brownian motion (left, dashed gray) and a pure sinusoid (left, solid gray) are shown for comparison.

learned spatial targets. We wondered how different motor cortical areas contribute to these processes. Suppressing an area required to stabilize posture or keep the brakes on movement will lead to an inability to hold still and a premature outward reach (Ebbesen and Brecht, 2017; Shadmehr, 2017; Velliste et al., 2014). Suppressing activity in a cortical area that promotes movement will reduce the probability of reaching out (Guo et al., 2015; Miri et al., 2017; Morandell and Huber, 2017; Peters et al., 2014). Suppressing activity in an area that controls reach direction could lead to inaccurate or highly variable movements (Mason et al., 1998).

Finally, inactivating an area that is unrelated to forelimb movement should not affect performance.

To distinguish these outcomes, we used joystick contact-triggered photoinhibition on randomly interleaved trials, using methods in VGAT-hChr2 mice described previously (see Methods, Movie S2) (Guo et al., 2014). We targeted four motor cortical regions previously implicated in forelimb control (ipsi- and contralateral rostral and caudal forelimb areas of mouse motor cortex: CFAcl, CFail, RFAcl and RFAil, see Methods) (Brown and Teskey, 2014; Harrison et al., 2012; Rouiller et al., 1993; Wang et al., 2017).

In no case did a cortical inactivation impair the ability to execute the learned hold; in fact inactivation CFAcl significantly increased the probability of satisfying the hold criterion (Figure 2.S2 and Table 2.1, $p(\text{hold}=\text{success})$ 0.38 ± 0.07 (control) vs 0.49 ± 0.09 (CFAcl Inactivated), $p<0.05$). During the hold, CFAcl inactivation did not affect the shape of the SDF. However, CFAcl inactivation significantly but subtly, altered the slope (intact: 1.957 ± 0.0028 vs inactivated: 1.966 ± 0.0027 , $p<0.01$ paired t-test), the transition point (intact: $27.59\pm 1.57\text{ms}$ vs inactivated: $32.45\pm 1.77\text{ms}$, $p<0.001$ paired t-test) and the offset (intact: $8.12\text{e-}04\text{ mm}^2/\text{s}$ vs

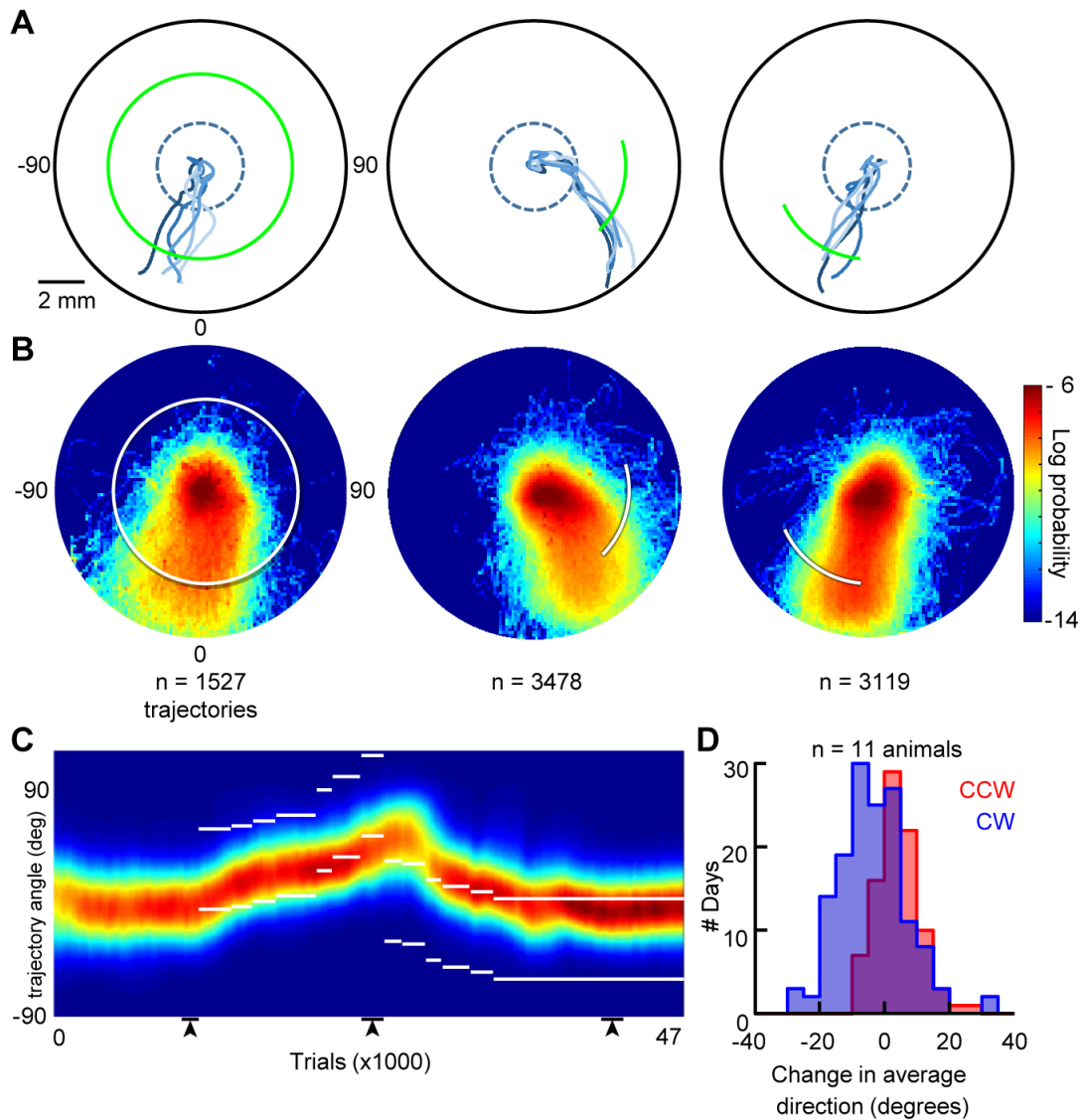


Figure 2.4. Mice learn to reach to spatial targets (A) Example trajectories from three non-consecutive days (5 trajectories plotted per day). Green line indicates the reward zone. (B) 2D-probability distributions of all trajectories for the mouse on days from which trajectories were sampled from in (A), white bar indicates the reward zone. Number of trajectories denoted at bottom. (C) Probability distribution of reach direction as a function of trial number for an example mouse, white bars indicate the rewarded zone boundaries. Black bars at bottom indicate data from the three non-consecutive days plotted in A-B (left to right order preserved). (D) Histogram showing change in reach direction per day as reward zones were rotated clockwise (negative angle change, blue) or counter-clockwise (positive angle change, red).

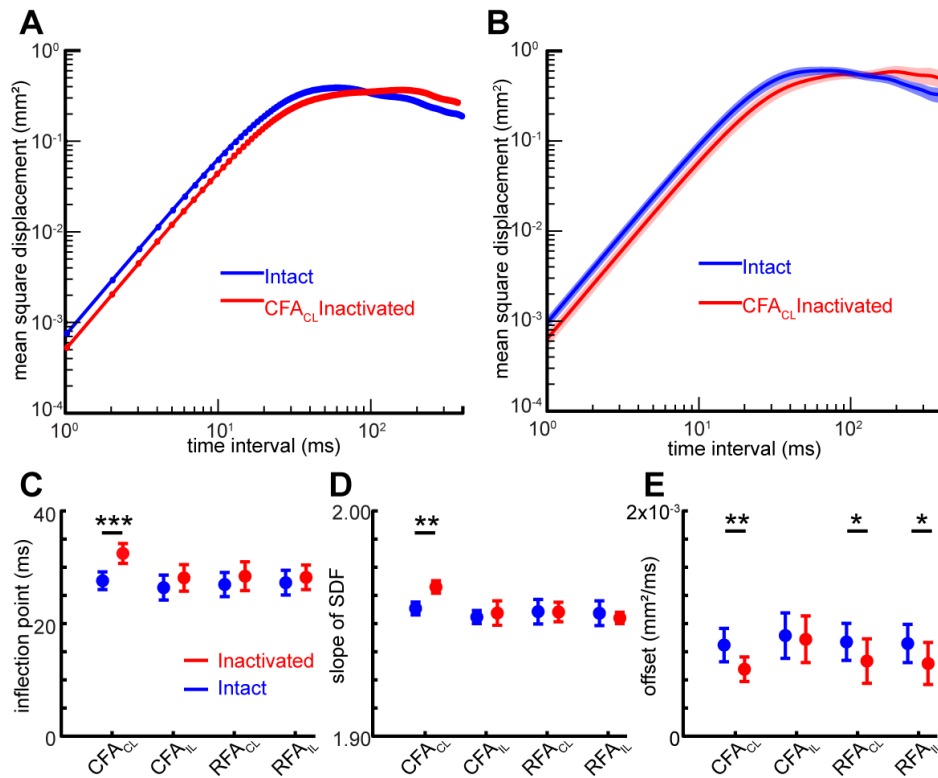


Figure 2.5. The Shape of the stabilogram diffusion function (SDF) during the hold is largely preserved during cortical inactivations. (A) SDF of the hold component of the trajectories with CFA_{cl} intact (blue) and inactivated from an example animal. (B) SDFs of trajectories with CFA_{cl} intact and inactivated across animals (n=7) (C) mean±SEM of transition points, (D) mean±SEM of slopes, and (E) mean±SEM of offsets of SDF's between intact and inactivated trials across various motor cortical areas. ***denotes p<0.001, **denotes p<0.01 and *denotes p<0.05, for a paired t-test (see Tables 2.2-2.4).

inactivated: $5.98e-04$ mm²/s, $p < 0.01$ paired t-test) of the stabilogram diffusion function. (Figure 2.5).

CFAcl inactivation also reduced peak trajectory speed and impaired outward reaching (Figure 2.6, Tables 5-6) (Peak trajectory speed: 115.98 ± 7.82 mm/s (control) vs 94.92 ± 8.03 (CFAcl), $p < 0.001$; Probability that a trajectory would transect outer radius: Control: $67.42 \pm 25.4\%$ vs. CFAcl: $48.02 \pm 3.43\%$, $p < 0.001$, linear mixed effects (LME) models, $n = 7$ animals, see Methods). In contrast, inactivation of CFAil or either RFA only modestly affected peak trajectory speed and did not affect the likelihood of reaching out (Figure 2.6, Tables 5-6).

To test how cortical inactivations influenced reach direction, we inactivated each cortical site as mice reached to at least two different targets. Surprisingly, cortical inactivations did not significantly affect reach direction (Figure 2.7A-F, Table 2.7, $p > 0.05$ all conditions, LME, see Methods). Inactivations also did not have a significant effect on the trial-to-trial variability of the direction of outward reaches (Figure 2.7G, Table 2.8, all conditions, $p > 0.05$).

The roles of different cortical areas in controlling primitive kinematics

The joystick's high spatiotemporal precision allowed us to analyze kinematic patterns of movement beyond the relatively coarse trajectory-level metrics described above. Trajectories exhibited complex, multi-peaked speed profiles, suggesting that they were composed of a sequence of discrete segments (Figures 1A-C and 9A-C). We tested the utility of two distinct decomposition algorithms commonly used in primate studies. One algorithm assumes that trajectories are derived from minimum-jerk basis functions with only three parameters: peak speed, duration, and the time in the sequence at which it is generated (see methods) (Gowda et al., 2015; Rohrer and Hogan, 2003; Viviani and Flash, 1995). This method was effective in decomposing mouse forelimb trajectories, in part because trajectories were composed of primate-

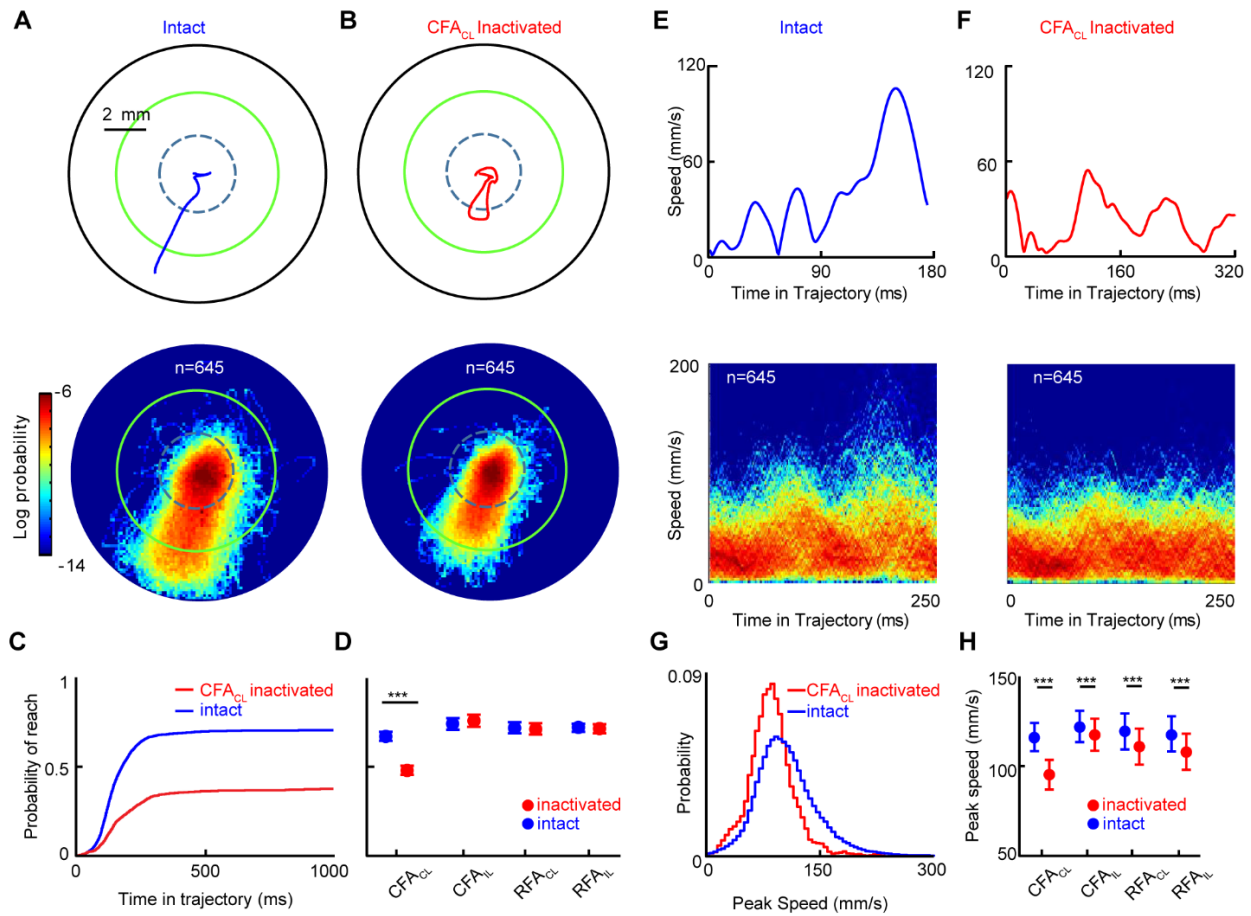


Figure 2.6. Effect of cortical inactivations on trajectory kinematics. (A-B) Example trajectories (top) and 2D spatial probability distributions (bottom) of trajectories during intact trials (A) and during randomly interleaved CFA_{CL}-inactivated trials (B). Data in A-B are from same mouse and same day. (C) Cumulative probability that a trajectory would transect the outer radius as a function of time during control (blue) and CFA_{CL} inactivated (red) trials. (D) Mean±SEM of probability of transecting the outer radius with or without inactivation of various motor cortical areas (n=7 mice). (E-F) Examples (top) and 2D distributions (bottom) of the speed profiles of the trajectories from (A-B). (G) Distributions of trajectory peak speed during the intact (blue) and CFA_{CL}-inactivated (red) trials shown in A-B. (H) Mean±SEM of the peak speeds with or without inactivation of various motor cortical areas (n=7 mice). *** denotes $p < 0.001$ LME (see Tables 2.5 and 2.6).

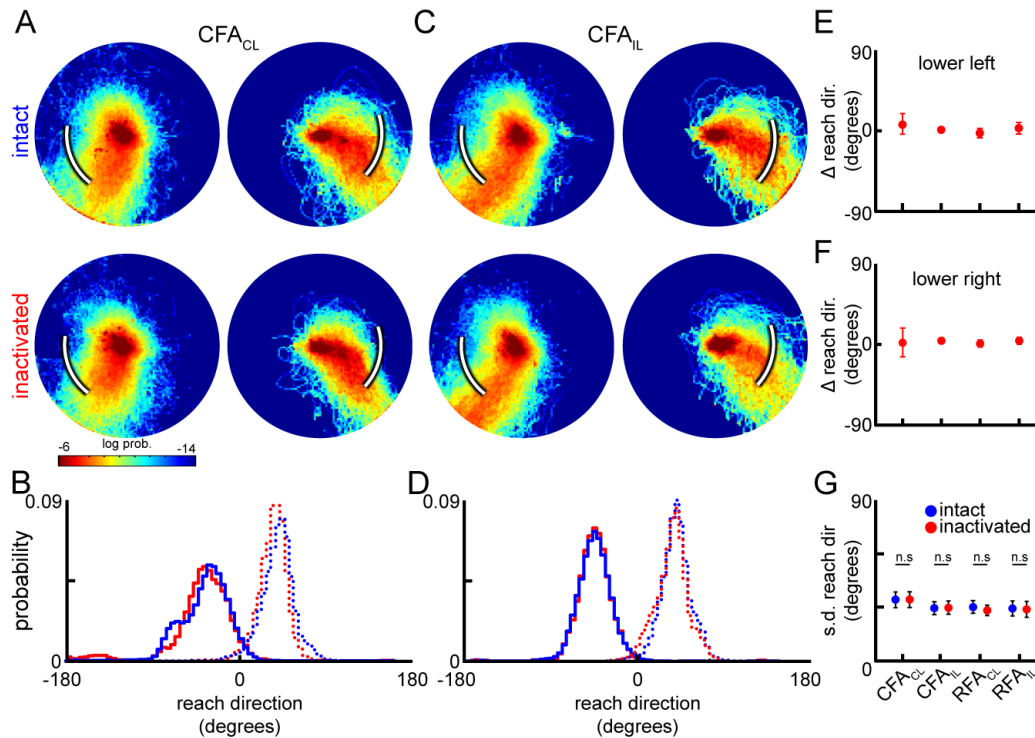


Figure 2.7. Effect of cortical inactivations on trajectory direction (A) 2D distributions of trajectories from intact (top) and CFAcl inactivated (bottom) trials when an example mouse was reaching to different rewarded locations, indicated by white bars. (B) Reach direction distributions for intact (blue) and CFAcl inactivated (red) trajectories when the reward zone was lower left (solid lines) or lower right (dotted lines). (C-D) Data plotted as in A-B from a different day when CFAil was inactivated. (E-F) mean±SEM of difference in reach angle between intact and inactivated trajectories across various motor cortical areas when the mice are reaching to lower left (E) or lower right (F). (G) mean±SEM of standard deviation of reach angle between intact and inactivated trials across various motor cortical areas (n=7 mice).

like superpositions of bell-shaped velocity curves (Figure 2.S4A-B), previously observed in mice (Azim et al., 2014; Mathis et al., 2017; Panigrahi et al., 2015). Following convention in primates we termed this class of kinematic primitives ‘submovements’. We also used a second decomposition algorithm that imposes segment boundaries at movement discontinuities revealed by temporally coincident minima in the radius of curvature and speed (Figure 2.1, Figure 2.9A-B) (Viviani and Terzuolo, 1982). This method essentially functions as a ‘sharp turn detector’ and identifies segments bounded by moments in a trajectory when a new force was imposed on the forelimb and, in a task that lacks external perturbations, also defines moments when an efferent neural command signal must have been generated by the central nervous system (Milner, 1992). We term this class of kinematic primitives ‘segments’.

Decomposition enabled each trajectory to be analyzed as a sequence of discrete primitives - each of which differed in kinematic parameters such as duration, complexity, speed, pathlength and direction (Figure 2.1C). Cortical inactivations could affect any or all of these parameters, and potentially in an amplitude-dependent way, i.e. differentially affecting hold-still versus reach components of the task. As expected, the durations, peak speeds, and pathlengths of primitives produced during hold-still periods were significantly smaller than during reaches ($p < 0.001$, LME, Tables 9-11). Notably, the difference in segment durations between hold and reach was subtle compared to differences in segment speed and pathlength (ratio of reach versus hold value for duration: 1.86 ± 0.04 ; peak speed: 2.54 ± 0.19 ; path length: 4.19 ± 0.35 , LME, Fig 7J-L). In fact, segment path length was more strongly predicted by its peak speed ($R^2 = 0.77 \pm 0.04$) than by its duration (0.58 ± 0.13 , $n=7$ animals, Figure 2.S5), suggesting an adherence to the isochrony principle, previously observed in primate reach and human handwriting tasks, in

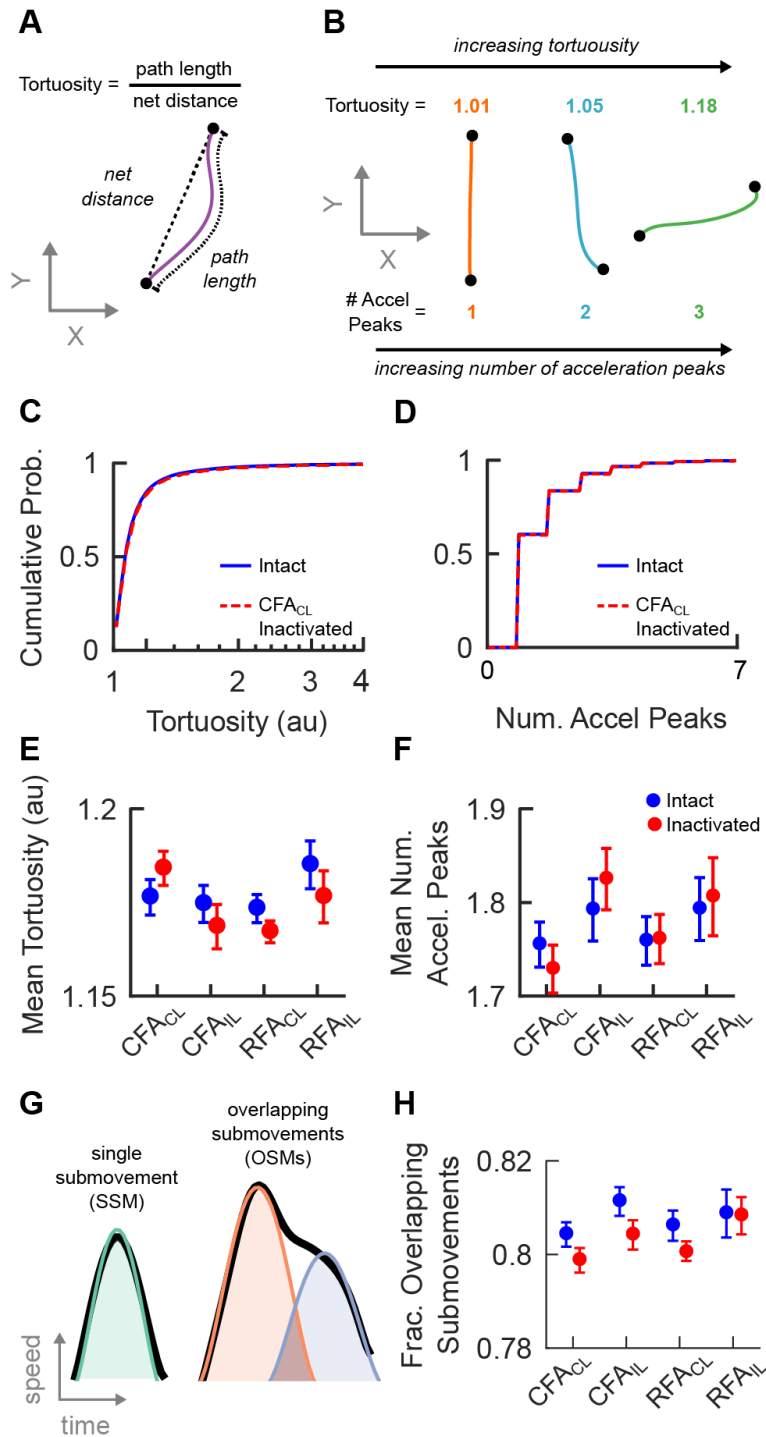


Figure 2.8. Motor cortical inactivations do not affect complexity of kinematic primitives. (A) Schematic defining the tortuosity of a segment. (B) Examples of segments with increasing complexity, as measured by increasing tortuosity (top) and number of acceleration peaks (bottom). (C) Cumulative probability distribution of the tortuosity values of segments in intact (blue) and

CFAcI inactivated (red dashed line) trials. (D) Cumulative distribution of the number of acceleration peaks of segments in intact and CFAcI inactivated trials. (E) Mean \pm SEM of segment tortuosity with (red) and without (blue) inactivation of various motor cortical areas. (F) Mean \pm SEM of number of acceleration peaks in a segment with (red) and without (blue) inactivation of various motor cortical areas. (G) A complementary complexity analysis for submovement sequencing. Schematic showing a single submovement produced in isolation (left) and two submovements that overlapped (right). (H) Mean \pm SEM of the fraction of overlapping submovements with (red) and without (blue) inactivation of various motor cortical areas.

which a segment's pathlength is more strongly predicted by its peak speed than by its duration (Viviani and Flash, 1995; Viviani and McCollum, 1983).

We leveraged our large dataset to obtain highly resolved distributions of kinematic parameters under cortex-intact and inactivated conditions (4,473,441 primitives (19.3% inactivated) from 131,092 trajectories (21.7% inactivated) from 7 mice). We first wondered if cortex might contribute to primitive complexity. Importantly, making primitive-level comparisons between cortex-intact and inactivated trials requires that segments retain their shape and complexity regardless of condition. For example segments could be either simple point-to-point reaches or more complex, tortuous curves (Figure 2.8A-B). Cortical inactivations did not affect three independent measures of primitive complexity: segment tortuosity ($p > 0.05$ across all brain areas, LME, Table 2.13), the number of acceleration peaks per segment ($p > 0.05$ across all brain areas, LME, Table 2.14), or the probability that decomposed, minimum jerk submovements would overlap ($p > 0.05$ across all brain areas, Wilcoxon rank sum test on fraction of overlapping submovements, Table 2.15), (Figure 2.8C-H) (Novak et al., 2002; Rohrer et al., 2004). This lack of effect of cortical inactivations on primitive complexity was striking and further justified direct comparisons of primitive kinematics across conditions. If cortical activity contributes to the neural command to generate a primitive, for example by redirecting the limb at a sharp turn, then silencing that area should alter primitive duration distributions (or equivalently, inter-segment onset intervals). Surprisingly, cortical inactivations did not change segment or submovement duration distributions for holds or for reaches (segment duration: $p > 0.05$ across all conditions, LME, Table 2.9; submovement duration: $p > 0.05$ across all conditions, Wilcoxon rank sum test, Table 2.15) (Figure 2.9D,G, Figure 2.S4D,G), ruling against a primary role of motor cortex in generating or timing primitives in our task.

CFAcl inactivation caused a significant reduction in segment speed and, because primitive durations were not affected, caused an associated reduction in segment pathlength (Figure 2.9D-L). This result was similarly observed for segments produced during both holds and reaches (peak speed during hold: 34.50 ± 3.76 mm/s (control) vs 25.89 ± 4.16 mm/s (CFAcl), $p < 0.001$; peak speed during reach: 94.04 ± 4.16 mm/s (control) vs 81.78 ± 5.20 mm/s (CFAcl), $p < 0.001$; path length during hold: 0.84 ± 0.15 mm (control) vs 0.62 ± 0.19 mm (CFAcl), $p < 0.05$; path length during reach: 3.83 ± 0.19 mm (control) vs 3.07 ± 0.27 mm (CFAcl) $p < 0.001$, LME, Tables 10-11). In contrast, inactivation of other motor cortical areas (RFAcl and RFAil) affected primitives executed during reaches but not holds (peak speed during reach: 93.02 ± 5.89 mm/s (control) vs 83.05 ± 7.29 mm/s (RFAcl), $p < 0.01$; path length during reach: 3.79 ± 0.23 mm (control) vs 3.27 ± 0.30 mm (RFAcl), $p < 0.01$; peak speed during reach: 93.05 ± 5.71 mm/s (control) vs 80.20 ± 7.47 mm/s (RFAil), $p < 0.01$; path length during reach: 3.85 ± 0.20 mm (control) vs 3.33 ± 0.29 mm (RFAil), $p < 0.05$; all other brain area/condition combinations for peak speed and path length: $p > 0.05$, LME, Tables 10-11).

Finally, we analyzed how kinematic primitives were directed in space. Rather than assigning each trajectory a single direction value based on where it transected the outer radius (as in Figure 2.4), here each primitive in a trajectory was assigned a single direction value based on its peak velocity vector (see Methods). Inactivation of CFAcl had a statistically significant but extremely subtle effect on primitive direction distributions, in line with the absence of an effect at the trajectory level (hold, lower right reward zone: $p = 1.15e-4$; hold, lower left reward zone: $p = 0.0057$; reach, both reward zones: $p > 0.05$, Watson U^2 test, Table 2.12) (Figure 2.9). Other cortical inactivations had no effect ($p > 0.05$ for all other brain areas/conditions, Watson U^2 test, Table 2.12) (Figure 2.S6).

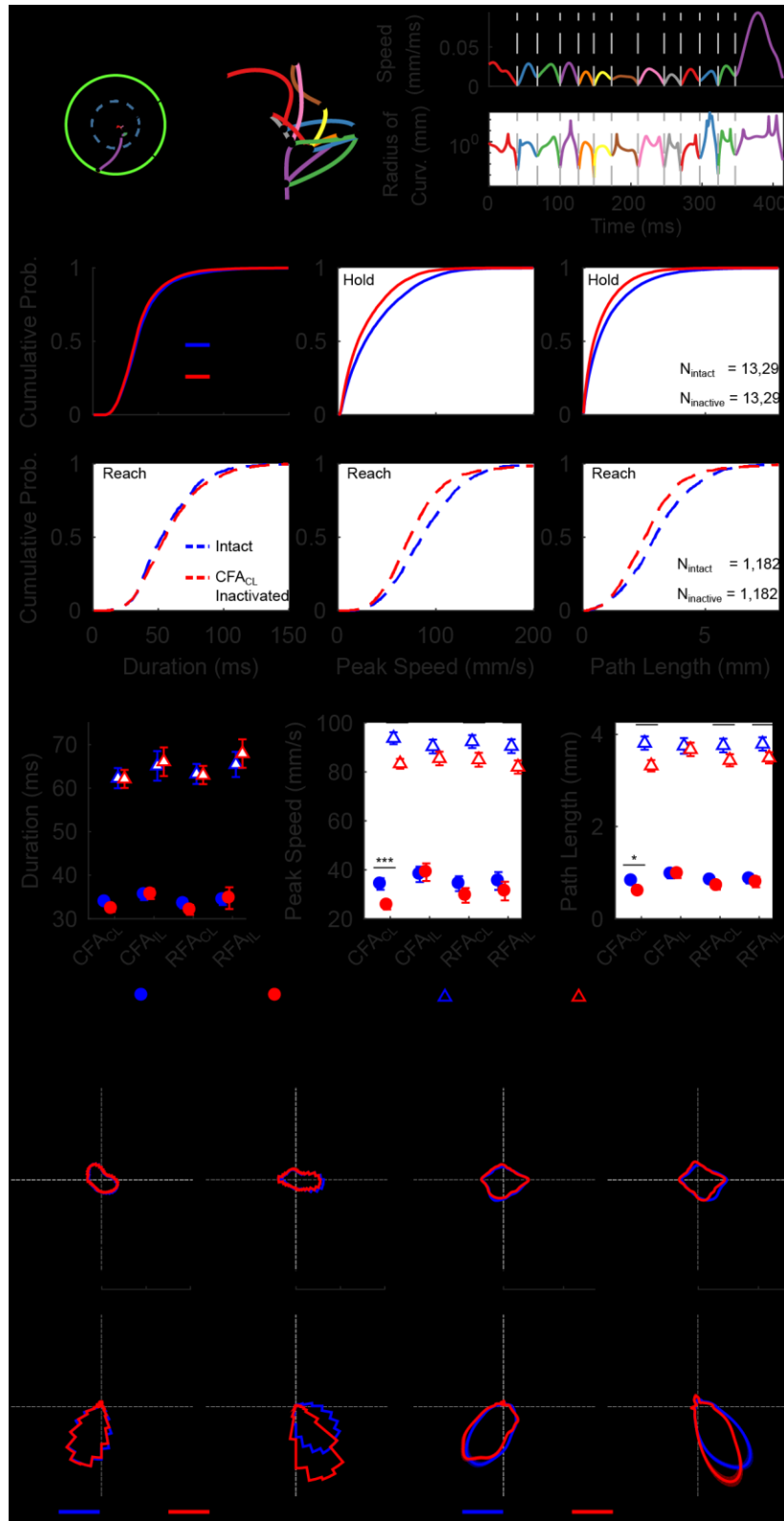


Figure 2.9. Effect of cortical inactivations on primitive kinematics. (A-C) Data plotted as in Figure 2.1A-B for a mouse forelimb trajectory. (A) Example mouse forelimb trajectory with black dots denoting boundaries separating decomposed segments. (B) Expanded view zooming in on micromovements produced during the hold period of the trajectory; different segments are color-coded. (C) Speed (top) and radius of curvature (bottom) are plotted as a function of time in the trajectory from A-B. Segment boundaries (gray dashed lines) are detectable as temporally coincident minima in speed and radius of curvature (see methods). (D-F) Cumulative probability distributions of durations (D), peak speeds (E) and pathlengths (F) of segments produced within the hold zone. Blue and red traces indicate data intact CFAc1 inactivated trials, respectively. (J-I) Distributions plotted as in D-F for the single segment in a trajectory that transected the outer radius (i.e. the reach segment). (J-L) Mean \pm SEM of duration (J), peak speed (K) and pathlength (L) with (red) and without (blue) inactivation of various motor cortical areas for hold (circle) and reach (triangle) segments. (M) Direction distributions of hold (top) and reach (bottom) segments for an example mouse in intact (blue) and CFAc1 inactivated (red) trials. (N) Data plotted as in M with average direction distributions across animals (n=7). See Figure 2.S4 for similar analyses on the submovement class of kinematic primitives decomposed using a minimum jerk model.

All results on primitive duration, speed, pathlength and direction were independently replicated when we instead decomposed trajectories into submovements using a minimum jerk model (Figure 2.S4 D-N, Tables 16-19).

Cortical inactivation reduced the gain of kinematic primitives

The observation that CFAcl inactivations similarly affected ~0.1 mm scale primitives executed during the hold and millimeter-scale ones executed during reaches suggests that the impact of CFAcl inactivations may follow a general rule. For example one possibility is that inactivated and intact kinematics differed by a constant value, which would be consistent with the loss of a fixed, amplitude-independent drive from the inactivated area. Alternatively, inactivated and intact kinematics could differ by a multiplicative value, which would be consistent with a decrease in gain, i.e. the loss of an amplitude-dependent drive from the inactivated area. To distinguish these possibilities, we combined hold and reach kinematic data into single distributions (Figure 2.10), and tested additive and multiplicative transformations of the inactivated data to “recover” cortex intact primitive distributions. We performed least-squares fits to determine the transformation that minimized the distance between the empirical distribution functions of the intact and the transformed-inactivated data. Intact peak speed and pathlength distributions were strikingly well fit by multiplying data from the inactivated dataset by a single ‘gain’ factor, while an additive model provided poor fits (sum of squared residuals (SSR) for duration: 0.058 ± 1.07 (additive model) vs 0.058 ± 1.07 (multiplicative model); peak speed: 388.1 ± 1.2 (additive model) vs 81.8 ± 2.0 (multiplicative model); path length: 647.3 ± 2.0 (additive model) vs 64.5 ± 1.5 (multiplicative model)) (Figure 2.10 A-I). The high quality of the multiplicative fits suggests that cortical inactivation simply reduced the gain of primitives. Consistent with this, multiplying the pathlength

of all segments produced under CFAcl inactivation by a single gain factor (see Methods), resulted in a probability of reaching out that was indistinguishable from intact trajectories (p(transecting outer radius) intact: $66.74 \pm 2.83\%$ vs FAcI inactivated and rescaled: $64.31 \pm 3.4\%$, $p > 0.05$, paired t test). Thus CFAcl inactivation-associated reduction in primitive peak speed and path length was sufficient to explain the undershooting observed at the trajectory level (Figure 2.10 J-M).

Discussion

We developed a touch-sensing, low torque joystick that resolves mouse forelimb kinematics with micron-millisecond spatiotemporal precision. We built joysticks into a computerized homecage system that automatically trains mice to produce complex, directed center-out forelimb trajectories while implementing closed-loop optogenetics. We then tested several hypotheses about how different motor cortical areas contribute to maintaining limb position and reaching to targets. We also used trajectory decomposition to test hypothesis about how kinematic parameters of primitives are controlled. We find that inactivation of contralateral CFA reduces the peak speed of kinematic primitives, but preserves their timing, complexity and direction. As a result, trajectories exhibited isomorphic hypometria, i.e. they retained their shapes and remained appropriately directed to targets but were spatially contracted. Our results identify conditions where motor cortical inactivation simply reduces the gain of motor output.

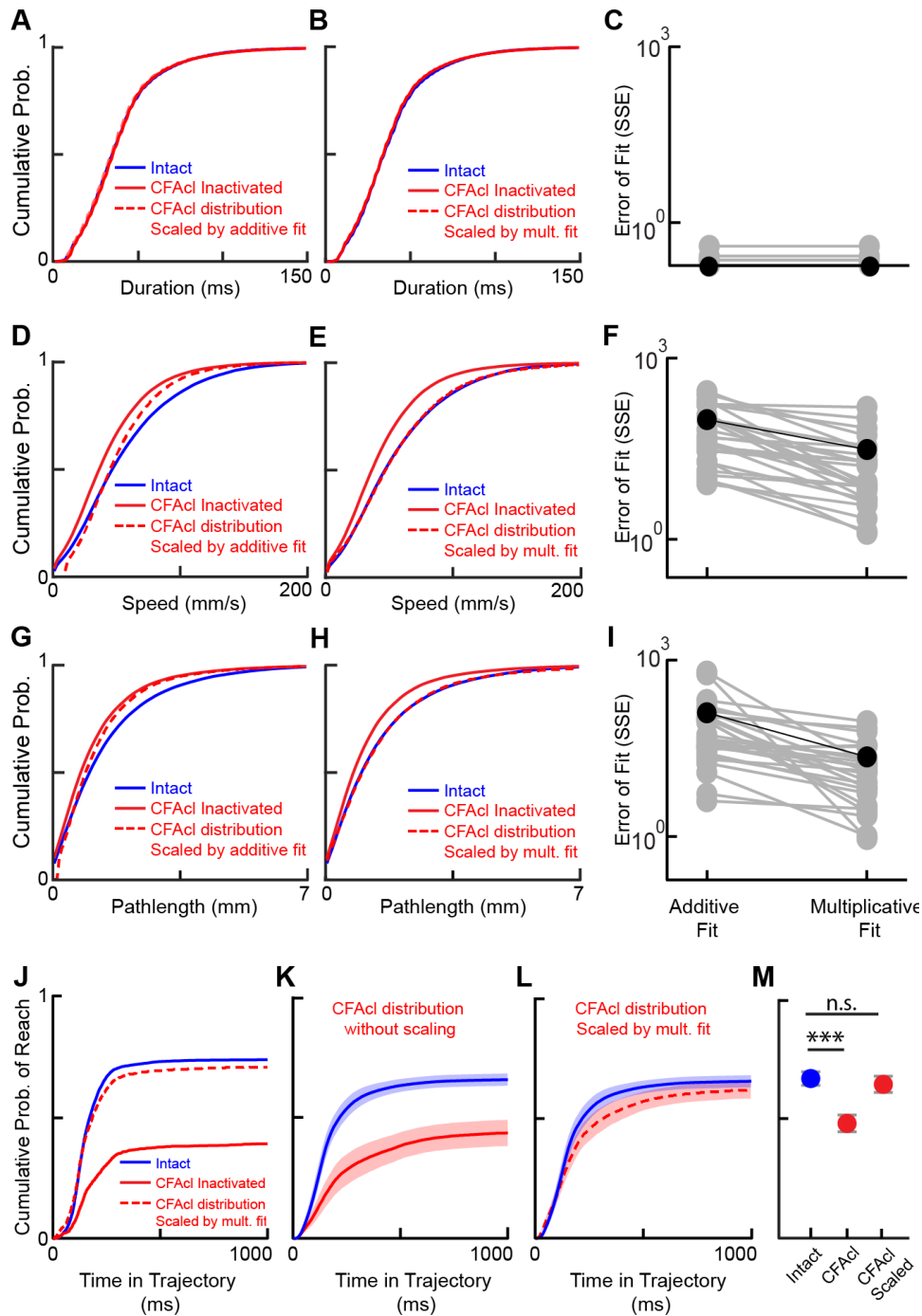


Figure 2.10. Primitive kinematic distributions from CFAcl inactivated dataset can be transformed into intact distributions by a single multiplicative gain factor. (A) Cumulative distribution of segment durations (intact, blue; CFAcl inactivated: solid red; CFAcl data rescaled by the best additive fit to match the intact distribution: dashed red). (B) Same as (A) but with

CFAcl rescaled by the best multiplicative fit (see Methods). (C) Summed squared error for the additive and multiplicative fits for all animals. (n=7). (D-I) Data plotted as in A-C for peak segment speed (D-F) and pathlength (G-I) distributions. Note the extent to which the multiplicative (but not the additive) fits match the intact data, suggesting that CFAcl inactivation is associated with the loss of an amplitude-dependent (and not fixed) premotor drive. (J) Cumulative distribution from a single mouse of the probability of reaching outer radius as a function of time in intact trials (blue), CFAcl inactivated trials (solid red) and in trials with trajectories reconstituted by multiplying all primitives by the multiplicative factor determined from fitting pathlengths (dashed red). (K) Mean \pm SEM of probability of reaching outer threshold as a function of time in intact (blue) and CFAcl inactivated (trials) across mice. (L) Same as (K) but with CFAcl inactivated trials rescaled by a multiplicative fit determined from fitting pathlengths. (M) Mean \pm SEM of probability that a trajectory would reach the outer radius, n=7 animals.

Forelimb motor control in rodents

While it is clear that rodent motor cortex is required for learning (Kawai et al., 2015; Peters et al., 2017), the roles of cortex in executing movements is complicated. First, permanent lesion, pharmacological inactivation, and photoinhibition can yield dissimilar results even during seemingly similar tasks (Otchy et al., 2015). Cortex lesions preserve ethologically relevant, potentially innate behaviors such as grooming, eating, swimming, fighting, playing and walking over obstacles, as well as producing previously learned behaviors such as grasping for pellets and producing learned lever tapping patterns (Grill and Norgren, 1978; Kawai et al., 2015; Sorenson and Ellison, 1970; Whishaw and Kolb, 1983; Whishaw et al., 1981). Yet acute inactivations impair prehension and cue-guided action selection under head-restraint (Galinanes et al., 2018; Guo et al., 2015; Miri et al., 2017; Morandell and Huber, 2017; Peters et al., 2014). Distinct task requirements in different behavioral paradigms result in different dependence on motor cortex, but core principles that dictate when a behavior will or will not require cortex remain frustratingly elusive.

To reduce task complexities and begin to dissect minimum circuits for the production and sequencing of primitives, we developed a task uncomplicated by head restraint, cues, visual guidance, or externally-induced sensory prediction errors yet rich enough to produce complex trajectories that are directed to spatial targets. Under these conditions loss of motor cortex caused a remarkably clear and specific deficit: reduced gain of movements of all amplitudes.

First, mice gradually learned to hold their right forelimb still in a small 2 mm ‘hold zone.’ Static maintenance of limb posture during appetitive tasks may require specific patterns of activity to actively suppress movement and/or actively maintain current limb position (Ebbesen and Brecht, 2017; Kaufman et al., 2014; Shadmehr, 2017). Given the joystick’s compliance, holding still while applying downward force (i.e. during gripping) created an inverted pendulum, or stick balancing, problem, in which corrective micromovements were required to maintain position

(Anderson, 1989; Bhounsule et al., 2015; Cabrera and Milton, 2002). Stabilogram diffusion analysis suggested that mice used an active control policy to maintain center-position that, interestingly, strongly resembled one used for maintenance of upright posture in humans (Peterka, 2002).

The generation, direction and timing of submillimeter-scale primitives produced during the hold were surprisingly intact during cortical inactivations, suggesting that subcortical pathways are sufficient to produce corrective movements required for postural control during holding-still (Azim et al., 2014; Murray et al., 2018; Walter et al., 2006). The slight changes in the offset, slope, and transition point of the SDF observed during motor cortical inactivation are all consistent with reduced speed, and suggests that although cortex could modulate corrective processes underlying postural stability, it is not required for the performance of the hold.

After executing the hold, mice reached out in different directions to spatial targets. CFAcl inactivation reduced both peak trajectory speed and impaired the ability to reach out. Previously, CFAcl photoinhibition resulted in halted or impaired prehension (Galinanes et al., 2018; Guo et al., 2015; Wang et al., 2017), and failure to push or pull a joystick in response to a cue (Miri et al., 2017; Morandell and Huber, 2017; Peters et al., 2014). Our novel findings emerged directly from our ability to resolve the tiny details of motion that persisted following CFAcl inactivation. First, at the trajectory level, neither reach direction nor variability were affected by cortical inactivation. Second, at the primitive level, direction, tortuosity, acceleration patterns and probability of submovement overlap were also not significantly affected. Even primitive duration distributions, which provide proxies for the rate at which the CNS sends efferent movement initiation commands to the periphery, were not affected. These data provide convergent evidence for subcortical control

of primitive generation and patterning in our task. Notably, a learned sequential tapping task in rats also implicated subcortical circuits in these functions (Kawai et al., 2015).

Motor cortex inactivation decreased gain of motor primitives

Behavioral deficits following photoinhibition do not necessarily reveal the function of the inactivated area (Otchy et al., 2015; Wolff and Ölveczky, 2018), cautioning against interpreting ‘positive’ results in our experiments as revealing the function motor cortex. Specifically, we regard it as unlikely that the sole function of motor cortex, with its complex recurrent circuitry and detailed kinematic representations (Brecht et al., 2013), is to simply to control the gain of movement. Our main discovery is not the positive result on speed in isolation; it is moreso the negative results showing that the cortical inactivation has minimum effect on primitive initiation, direction and complexity and, relatedly, on trajectory shape.

Another caveat is that mice are clearly not primates, and our task differed in several respects from canonical primate center-out reach tasks. First, whereas our task gradually shaped reach direction over day timescales, most primate reach tasks are visually guided and explicitly cue target locations on a trial-by-trial basis (Georgopoulos et al., 1988). Second, our animals were freely moving and only engaged the task of their own volition in their homecage, whereas studies in primates typically involve water/food deprivation and head restraint. Third, primates have a highly specialized forelimb motor cortex that includes multiple corticospinal regions and direct projections to motor neurons (Dum and Strick, 2002; Lemon, 2008). Finally, whereas cortex-lesioned rodents exhibit remarkably intact behavioral repertoire (Sorenson and Ellison, 1970; Whishaw and Kolb, 1983; Whishaw et al., 1981), large cortex lesions in primates are associated with more severe effects including paresis that can be refractory to recovery, especially without

subsequent training (Darling et al., 2011; Nudo, 2013; Zeiler and Krakauer, 2013). All of these considerations likely underlie important differences in cortical control of movement across species.

Caveats aside, our main result - that cortical inactivations reduce the gain of primitives, resulting in hypometric but otherwise intact trajectories - bears an uncanny resemblance to several studies in humans and non-human primates, even replicating some very specific details. Cortical stroke, GPi inactivation, Parkinsonism and even some types of cerebellar damage can result in weakness and bradykinesia but with essentially intact initiation and direction (Darling et al., 2011; Lawrence and Kuypers, 1968; Manto et al., 1998; Passingham et al., 1983). Motor cortex lesion can result ‘undershooting’ of appropriately-timed and directed wrist movements (Hoffman and Strick, 1995), or mastication patterns with normal timing and patterning yet with contracted trajectories (Larson et al., 1980). Motor cortex lesion can also diminish the amplitude of essential tremor, showing a specific case where loss of cortex decreases the gain of subcortically generated (albeit pathologic) movements (Dupuis et al., 2010; Kim et al., 2006). Inactivation of basal ganglia output and Parkinsonism also result in bradykinetic, hypometric reaches that are otherwise appropriately timed and aimed (Desmurget and Turner, 2008; Panigrahi et al., 2015), again suggesting an oddly similar phenotype. The essence of these deficits are evident in analysis of handwriting in patients with Parkinson’s: micrographia, or shrunk text, is due to normally timed and directed strokes that simply have reduced peak speed and, therefore, pathlength. Notably, the magnitude of bradykinesia and a hypometria is usually proportional to movement amplitude suggesting the loss of an amplitude-dependent drive (Broderick et al., 2009; Van Gemmert et al., 2003), exactly as we observed (Figure 2.10). Finally, hypometric reaching can also be observed following inactivation of cerebellar outputs (Cooper et al., 2000; Martin et al., 2000). Thus our

results capture essential features of conventionally distinct pathologies: motor cortex lesion, inactivation of basal ganglia or cerebellar output, and Parkinsonism.

Why are bradykinesia and hypometria such common failure modes of the motor system? The answer may not lie in the idea that disparate parts of the motor system are ‘dedicated’ to speed or gain control (Golub et al., 2014), and may instead lie in control theoretic accounts of movement (Scott, 2004; Shadmehr and Krakauer, 2008; Todorov and Jordan, 2002). The essence of this framework is that the motor system can be described as one or more feedback controllers generating movement commands while minimizing effort and maximizing target accuracy. Consistent with this idea, disrupting feedback during a goal directed reach causes oscillations around the target (Azim et al., 2014; Flament et al., 1984), similar to what occurs when feedback is disrupted in canonical feedback systems, such as PID controllers used in servo motors (Aström and Murray, 2010). However, instead of inactivating the feedback, what would happen if you inactivate the *output* of the control loops? In cases where the system is described by a single control loop, loss of output means, trivially, loss of behavior. However, in a system with multiple control loops operating in parallel, the specific behavioral deficit associated with loss of a single loop can be complicated because each controller’s contribution to behavior is task-dependent (Wolpert and Kawato, 1998). Each controller is likely to also play unique roles in learning (Doya, 1999). But for well-learned behaviors detailed kinematics of upcoming movements are represented in cortex, basal ganglia and cerebellum (Fortier et al., 1989; Fu et al., 1997; Schwartz, 2007; Scott, 2003; Shenoy et al., 2013; Turner and Anderson, 1997; Wong et al., 2014). These representations suggest that when the system is well trained multiple controllers have acquired useful models that contribute to motor output, such as initiating a primitive and directing its path to a target. It follows that transiently losing a single controller could reduce the drive of the system towards the target,

but the behavior would remain essentially intact due to the ongoing commands of the other, non-inactivated controllers. This hypothesis attempts to account for the isomorphic hypometria observed in our study (in which mice were highly trained) as well as the observation that diverse insults to the adult human motor system result in conceptually similar micrographia (Inzelberg et al., 2016). An interesting prediction of this hypothesis is that, in our well-trained center-out task, inactivating basal ganglia output, cerebellar output, or inducing Parkinsonism could all lead to similar deficits, an intriguing prediction supported by previous work (Cooper et al., 2000; Desmurget and Turner, 2008; Martin et al., 2000; Panigrahi et al., 2015) that is now easily testable with our open-sourced automated system.

Materials and Methods

Experimental model and subject details

All experiments and procedures were performed according to NIH guidelines and approved by the Institutional Animal Care and Use Committee of Cornell University.

Experimental Animals

A total of 11 adult male VGAT-ChR2-EYFP line 8 mice (B6.Cg-Tg(Slc32a1-COP4*H134R/EYFP) 8Gfng/J; Jackson Laboratories stock #014548) were used. The mice were between 18-40 weeks old for the duration of the experiment. All animals were individually housed under a 12hr light/dark cycle for the duration of the study and had continuous access to the task. The animal's daily water intake was monitored using an automated system. If the water intake was less than 1ml, the system automatically dispensed water to make up the difference.

Method details

Surgery

Under isoflurane induced anesthesia, we implanted 7 of the mice with 400um 0.43 NA fiber optic cannulas bilaterally over Caudal Forelimb Area (CFA) (0.5mm A/P, ± 1.5 mm M/L) and Rostral Forelimb Area (RFA) (2.2mm A/P, ± 1.0 mm M/L).

Principle of Operation and Signal Processing Pipeline

The joystick.

The need for a custom joystick to monitor forelimb kinematics in mice. We considered commercially available joysticks such as: HF46S10 from APEM, the 67A from grayhill and the inductive joysticks from CTI. There were five main shortcomings of these products that made them unsuitable for the study of kinematics in mice. (1) Isometric force profile: All the industrial joysticks have a recentering mechanism that relies on two compression springs set along orthogonal directions. This always leads to moving along the diagonal being up to 40% harder than along the axes of the springs. We solved that problem by using one set of centering magnets right below the joystick. (2) Low displacement force: The industrial joysticks have a displacement force of about 100-250 gf (gram force), ~ 2.5 Newtons of force, this can be reduced by having a long lever arm. For example, you can lengthen the lever arm by 10 times to get into a 0.1-0.2N range, however, this still puts a lot of load on mouse forelimb kinematics. The centering mechanism we use gives us 0.0081 N/mm, or about 32 mN to move the full range of the joystick, this allows us to get the fine details of motion even when the animal is holding still (10-100 um scale) and finer resolution when the mouse is making large (~ 1 mm scale) movements. (3) Future Force Controllability: Our design supports the dynamical control of displacement force on the joystick. By switching out the centering magnet with an electromagnet, we can dynamically control force in real time, and coupled with our real-time microsecond FPGA, we can make that

force dependent on a behavioral variable like speed. (4) Built-in touch sensor: Off the shelf joysticks do not provide a readout of when the animal is actually holding the joystick, complicating attribution of displacement by potentially confusing active (animal-induced) versus passive motion. (5) Dead Space: Some commercial joysticks are intentionally designed (in hardware) to have dead-space. I.e. there will be no reading if the joystick is moved in within a certain distance. Presumably to protect against accidental movement of the joystick.

A custom joystick that solves these problems. The core of our joystick system was a two Axis Hall Sensor (Sentron, 2SA-10G). Moving the joystick changed the angle of the incident magnetic field generated by the magnets on the hall sensor. The change in incident magnetic field provided X and Y voltage (0-5V) as a linear readout of displacement. The top of the joystick was a conductive ball which was connected to an active capacitance touch sensor (AT42QT1011) that provided instantaneous read on the joystick being contacted. To calibrate the joystick, i.e. to determine the voltage vs distance relationship, we set up the joystick in a custom, precision machined setup that allowed the manipulandum to move along a narrow channel along an outward directed radial axis. Then, using an electronic screw gauge, the joystick was displaced from the center position along the radial axis in increments of 500um. At each displacement we recorded the voltage from the joystick's hall sensor. We then repeated these measurements along a radial axis in a direction non-orthogonal to the first. To quantify spatial resolution we first measured the x, y voltages from the device when it was at rest, used the calibration to convert the signal from volts into units of distance (mm). We then calculated the standard deviation of the distance distribution over 2000 samples (2sec) for each device. To quantify stiffness of the joystick, we rotated the joystick by 90 degrees, such that the joystick manipulandum was horizontal to the

ground, and applied varying weights to the end of the joystick while measuring the displaced distance. We repeated these measurements by rotating the joystick around the axis of the manipulandum in ~30 degree increments. See supplemental methods for construction and design details.

Fixed Post

A “Fixed Post” was placed in the home-cage and it also had a conductive ball connected to an active capacitance touch sensor (AT42QT1011).

Nose Poke

The Nosepoke Sensor was a modified IR diode-phototransistor pair (LTH-301-32) from Lite-on devices. The IR LED and the phototransistor were separated and placed across the nose poke port. When the mouse put its snout through the port, it broke the IR beam and drove the signal high.

Water Delivery

The mice received water through a lick spout (H24-01-TB-01, Coulbourn Instruments) connected to a precision solenoid valve (Lee Company LHDA2433215H). The valve received water from a reservoir whose level was constantly maintained by closed loop water recirculation, providing stable microliter precision in water delivery over week timescales.

Signal Conditioning Circuitry

We built signal conditioning circuitry at each homecage to calibrate the sensors and provide noise immunity. Specifically, we (1) used unity gain buffer amplifiers (LM358, Texas Instruments) to protect the joystick signals from noise as they were routed to the computational system; and (2) calibrated the nose poke sensor by biasing the phototransistor at the edge of the linear zone to

reduce detection hysteresis, and used a comparator (TL331, Texas Instruments) to convert it to a TTL digital output.

Breakout Board and Voltage Protection System

The digital and analog sensor signals from all the behavioral boxes reached the computational unit (CU) through the breakout board. On the breakout board, for each line we used a Thermistor (PRF18BB471QB5RB) to protect the CU from high current surges and Schottky diodes (TBAT54S, Toshiba Electronics) to protect the CU from high voltages. After the voltage/current protection circuitry, analog and digital lines from each behavior box were separated and routed to the right connector.

Computational System

Hardware

The core of the computational system was a Single Board Real-time Input/Output system (sbRIO-9636, National Instruments). The sbRIO had both a Field Programmable Gate Array (FPGA) and a Real-Time Processor (RTP) on the same board. It had 16 Analog inputs, 4 analog outputs and 28 Digital I/O ports. The FPGA is programmed through LabVIEW. See supplemental methods for construction and design details.

Overview of the Software Infrastructure

There were four major components of the software architecture: (i) Every millisecond the FPGA code processed both the digital inputs (nose poke sensors, touch sensors) and analog inputs (Joystick X,Y) to determine if the trial was “live” and if the “hold” and reach-out contingency was met. The FPGA code also directly interacts with the digital outputs. It controlled the solenoid valve for the water reward, the masking light used during photoinhibition and patterns the optogenetic output. The FPGA took ~37 microseconds to process the contingency requirements. At the end of

each millisecond, the FPGA wrote all the input sensor data and the generated outputs to a FIFO register on the FPGA. Using an onboard FIFO prevented sampling errors and discontinuities. (ii) Every second, the code on the RT processor read from the FIFO register using a Direct Memory Access method (DMA) and packaged it into a single array element. The sbRIO had limited onboard memory and could not hold the vast behavioral data being generated, it required a secondary storage solution. Importantly, the data-transfer needed to be fast, in real time and have temporal continuity. We used Network Stream Objects to set up communications between the sbRIO and the server grade acquisition computer. We developed a simple data protocol containing the data, the timestamp and a frame ID. The data from the RT was packaged using this protocol and sent over the Network to the acquisition computer. In addition to packaging and transferring the data, the code on the RT also had the programmatic access to all the parameters of the task, i.e. hold time, reach angle, water dispense time, optogenetic power, optogenetic stimulation time and had the ability to deliver rewards to mouse boxes with a tunable poisson distribution. (iii) The code on acquisition computer (“PC code”) was set up to interface with the appropriate sbRIO and continuously monitored the network stream for any new data packets. If a data packet was detected, the PC code unpacked the data, split it into separate channels, identified the sequence of the data, created filenames for each data file, and then wrote the behavioral data onto the RAID server with generated filenames. Each filename was coded to provide information on the mouse it came from and the settings of the behavioral paradigm. (iv) During training, the behavioral data was automatically analyzed at the end of the day (~11 PM) to determine the new training parameters. The code combined and extracted all valid trials joystick trials from the day, the number of rewards, distributions of hold-times and reach directions. If the animal hadn’t had enough successful trials to meet its daily water requirements, the system communicated with the RT code

to automatically dispense water to make up the difference and the contingency of the task remained unchanged. If the animal met its daily requirement of water intake, the contingency was updated to reward only 15% of the trials based on the current distributions of the hold time and reach direction

Optogenetics light source and control

We used Laser LED light sources (LDFLS_450-450, Doric Life Sciences Ltd), attached to an optical rotary joint (FRJ_1x2i_FC-2FC_0.22) and delivered light to the implanted cannulas using 400um, 0.43NA lightly armored metal jacket patch cords. The light sources were set to analog input mode and driven with a sinusoidal pulse (40 Hz, 15mW peak) generated by the sbRIO.

Behavioral Shaping and Photoinhibition

We used a sequence of reward contingencies to train mice to perform ‘hold-still’ + direction-specific center-out reaches. i) On day 1 water restricted mice (~6hrs) were placed into joystick endowed home cages. Water was automatically dispensed with a poisson distribution (mean 150s). If the mice simultaneously did a nosepoke (np) and contacted both joystick and the fixed post (fp) for more than 50ms they were rewarded with water. ii) On Day2-Day3 after mice started interacting with the joystick, we changed the reward contingency such that the mice only get rewarded if they contact the Joystick after both the NosePoke and FP. (iii) After the mice learned to contact the joystick last in sequence, we changed the reward contingency such that mice had to move the joystick out to at least 4mm from the center in order to get rewarded. (iv) Once the mice started reaching out to 4mm, we gradually shaped the “hold-time” of the trajectories. Hold time was defined as the amount of time the trajectory spent within 2mm radius of the center. We shaped the trajectories by setting the required hold-time for reward each day as greater than

the 75th percentile of hold time distribution of the previous day. This was repeated till the 75th percentile of the hold time was greater than 100ms. At which point, the required hold-time was set to 100ms. (v) We then characterized the reach-angle distributions of the mice. The reach-angle was defined as the angle at which the trajectories crossed the 4mm reward threshold. (vi) After characterizing the reach angle, we performed the first set of CFA and RFA inactivations, we iterated through CFAcl, CFAil, RFAcl, and RFAil by moving the fiber optic cable onto the relevant implanted cannula and turning on the laser in ~15% randomly interleaved trials (vii) The reach-angle was gradually shaped clockwise (CW) or counter clockwise (CCW) by rewarding either the 15th percentile (CW) or the 85th percentile (CCW) of the reward distribution till the mean of the new distribution was different by at least ~60 degrees. (viii) We then stopped the angle shaping and performed the second set of CFA and RFA inactivations.

Quantification and statistical analysis

Trajectory level analysis

Trajectories were acquired at 1kHz and low pass filtered at 50Hz with an 8-pole Butterworth filter in software. Hold-time was defined as the amount of time the trajectory was within the inner radius (2mm) starting from joystick contact. The reach direction was defined as the angle at which the outer radius was transected by the trajectory. Velocity was calculated as a one sample difference of the position vector. To make sure that we were specifically analyzing trajectories that were attributable to right forelimb movement with the animal in a consistent posture, only the trajectories that were contacted after the nose poke and fixed-post contact were considered valid trials eligible for reward. If the mouse exited the nose poke, lost contact with the fixed post or the joystick, the trial was immediately failed. The mouse also failed the trial if it

exited the inner-radius earlier than its hold-still requirement or if it reached in the wrong direction. There were no cues for failed or successful rewards (except the water delivery apparatus). However, a blue LED masking light roughly at eye level to the mouse was turned on at joystick contact. The mouse had to re-contact the joystick in order to start a new trial after both successful and failed trials.

Minimum jerk decomposition and trajectory segmentation

In order to decompose complex trajectories into primitives, we employed two methods: the first was to fit trajectory kinematics to a linear combination of minimum jerk basis functions (called submovements) (Gowda et al., 2015; Rohrer and Hogan, 2003; Viviani and Flash, 1995), and the second was to break up trajectory kinematics into segments, where segment boundaries were defined by temporally coincident minima of velocity and radius of curvature (Milner, 1992; Viviani and Terzuolo, 1982). To implement the former, we followed the method from (Gowda et al., 2015), using the MATLAB package described therein. In short, the code performed a least-squares fit of the six-dimensional description of joystick kinematics (position, velocity, and acceleration for both the x and y coordinates) to a series of minimum-jerk basis, whose velocity profile took the functional form:

$$v(t; t_0, D, A) = (A/D) \times [30\tau^4 - 60\tau^3 + 30\tau^2]$$

Where τ gives the normalized time, defined as $\tau = (t - t_0)/D$, t_0 is the initiation time of the submovement, D is the duration of the submovement, and A is the amplitude. Importantly, the function is defined to be zero outside the bounds $[t_0, t_0 + D]$. The fit procedure did not require

strong assumptions about the number of submovements prior to running the fit, but rather iteratively added submovements to improve the overall fit until a cost function threshold was reached.

The second decomposition algorithm, which used coincident velocity and radius of curvature minima and is the primary decomposition method discussed in the main text, did not rely on any optimization or assumptions regarding the parameterization of primitives. To determine these segment boundaries, we identified the velocity and radius of curvature minima for each trajectory, and assigned a segment boundary whenever these minima were temporally separated by no more than 1 ms. This method acted as a sharp turn detector, and identified temporal boundaries within a trajectory that must have arisen from a new force applied to/via the forelimb.

Segment Analysis.

We performed analyses on primitives, obtained using the methods described in the previous section, in order to gain a finer-scale description of joystick trajectories. Because we are primarily interested in task-related movements, we excluded from our analyses the first primitive produced during each trial. This ensured that our data set did not include motion related to grasping the joystick, but instead only included controlled motion. Furthermore, we excluded from our analyses any primitive with duration < 10 ms. From the primitives we obtained through decomposition/segmentation, we extracted various kinematic parameters to describe said primitive. In the case of minimum jerk basis functions, each submovement was uniquely defined by four parameters: the start time, duration, amplitude (path length), and direction of the submovement. Each of these was calculated directly from the code in (Gowda et al., 2015). Peak speed for submovements was obtained by taking the ratio of amplitude to duration, multiplied by

the constant 1.875 (reflecting the characteristic bell-shape of the submovement basis function). Finally, because multiple, distinct submovements can be occurring at the same time within a trajectory, we measured the fraction of submovements that have temporal overlap (calculated as number of overlapping submovements divided by total number of submovements) as a proxy for motion complexity--when multiple submovements overlap, they give rise to velocity profiles that have richer structure than a train of non-overlapping bell-shaped velocity peaks. In the case of segments defined by coincident minima of velocity and radius of curvature, there was no set number of descriptors that uniquely defines a segment. Segments varied from simple point-to-point reaches to motions with a more complex spatial and velocity profiles. To quantify the degree of complexity for each segment, we used two complementary metrics: the tortuosity of the segment (defined as the path length divided by the distance between start and end points) and the number of acceleration peaks within a trajectory (found using standard peak identification techniques in MATLAB). We also extracted from segments various other kinematic parameters, including the duration, path length, peak speed, and direction. Here we defined segment direction as the angle between the initial position of the segment and the position of the segment at its maximum speed. Finally, because we were interested in the differential effects of cortical inactivations on different types of movement, for many analyses we separately analyzed the primitives involved in the “hold still” and “reach” portions of the task. The “hold” primitives for each trial were defined as the primitives that occur prior to the first inner threshold crossing of the trajectory--this corresponded directly to the definition of the hold period in the task structure. The “reach” primitive for each trajectory was defined as the first primitive to cross the outer threshold, regardless of whether the hold period was completed successfully. Thus each trajectory contained at most one reach

segment, but potentially multiple overlapping reach submovements. We used these categories to analyze the movement-type-dependent effects of cortical inactivations, as in Figure 2.9.

Stabilogram Diffusion Analysis of the ‘Hold-Still’

The stabilogram diffusion function (SDF) gives the mean squared displacement over a specified time window. The SDF was calculated on ‘hold-still’ part of the trajectories by only analyzing the trajectory up to the onset of the segment that exited the inner radius. The mean squared displacement $\langle \Delta r^2 \rangle_{\Delta t}$ for a time interval Δt is given by:

$$\langle \Delta r^2 \rangle_{\Delta t} = \frac{\sum_{i=1}^N \Delta r_i^2}{N}$$

Where N is the total number of points for the time interval across all the trajectories for that condition, and Δr^2 is the squared displacement for each of those of points. The slope and the offset of the log-log plot of the SDF is estimated by linear fit to the first 10ms of the SDF. The transition point is defined as the intersection of the line estimated by the linear fit of the first 10ms with the tangent drawn at the peak of the SDF in the first 100ms.

Statistical Analyses

To determine the effect of cortical inactivation on segment and trajectory kinematic distributions, we fit linear mixed-effects (LME) models to our data set, with random intercept terms to account for variation both i) between mice and ii) across days for a given mouse. We added fixed effects corresponding to i) whether the segment or trajectory was performed during a trial with optogenetic manipulation, ii) in case of segments, whether the mouse was executing the

‘hold’ or ‘reach’ portion of the task (called ‘Condition’), and iii) the interaction between laser and task portion. We fit individual models for each pair of kinematic variable and brain region, where kinematic variable is peak speed, path length, or duration and brain region is CFAcl, CFAil, RFAcl and RFAil. The generic form of this model is thus: $(Kinematic\ Variable) \sim 1 + Laser * Condition + (1 | Mouse) + (1 | Mouse : Day)$. From these models, we determined the effect of inactivation of different motor cortical areas on segment kinematics; a summary of these model fits along with their specific formulation is given in Tables 1-8.

We use a similar model structure to analyze the statistics of segment complexity. In this case, we do not add a fixed effect for hold vs reach segments, so the model is of the form: $(Measure\ of\ Segment\ Complexity) \sim 1 + Laser + (1 | Mouse)$. We use tortuosity and number of acceleration peaks as measures of segment complexity (discussed above), and thus fit individual models for each combination of brain area and the two complexity measures. A summary of these results is given in Tables 10-11.

For the analysis of submovement kinematics, we found that a linear mixed-effects did a poor job of capturing the structure of our data; as an alternative, we performed a Wilcoxon rank sum test on measures of submovement kinematics and complexity, separating data by both brain area and movement type (hold vs reach), and then aggregating data at the day level. The results obtained from these rank sum tests are given in Tables 12-14 (submovement kinematics) and Table 2.16 (fraction of overlapping submovements). Finally, to analyze the statistics of both segment and submovement direction, we applied a Watson U^2 test to cortex intact vs cortex inactivated data. The Watson U^2 test is used to test the null hypothesis that two samples of data with periodic boundary conditions (i.e. angle data) are drawn from the same distribution--in the case of a significant p value, we can reject the null hypothesis and conclude that the two samples are likely

drawn from different distributions. Importantly, this test only assesses the similarity of the sample distributions and does not provide information about the magnitude or type of difference between the two samples. In the case of this direction analysis, we separate primitive data for testing based not only on the basis of 1) hold vs reach and 2) intact vs cortex inactivated, but also by the direction that the animal has learned to reach during that particular day. At a coarse-grained level, we thus separated primitive direction data by whether the animal was being asked to reach to the lower left or lower right. We performed the Watson U^2 test on direction data for both segments and submovements for each of the 16 possible combinations of data types ((4 brain areas) x (2 movement types) x (2 rewarded reach directions)). These results are summarized in Tables 9 (segment) and 15 (submovement).

DATA AND SOFTWARE AVAILABILITY

All the software (trajectory analysis, real time control software, automation analysis) and the hardware design schematics, including part files and building instructions are available at: www.github.com/GoldbergLab/RodentJoystick

Acknowledgements

We thank Joe Fetcho, Melissa Warden, Lena Ting, and Goldberg lab members for helpful discussions and providing comments on the manuscript. JHG was supported by NIH (DP2HD087952), the Pew Charitable Trusts, and the Esther A. & Joseph Klingenstein Fund. T.B. and S.C.W. were supported by the Cornell Mong Neurotech Fellowship

REFERENCES

- Anderson, C.W. (1989). Learning to control an inverted pendulum using neural networks. *IEEE Control Systems Magazine* 9, 31-37.
- Aström, K.J., and Murray, R.M. (2010). *Feedback systems: an introduction for scientists and engineers* (Princeton university press).
- Azim, E., Jiang, J., Alstermark, B., and Jessell, T.M. (2014). Skilled reaching relies on a V2a propriospinal internal copy circuit. *Nature* 508, 357-363.
- Bernstein, N.A. (1967). *The Coordination and Regulation of Movements* (Oxford: Pergamon Press).
- Bhounsule, P.A., Ruina, A., and Stiesberg, G. (2015). Discrete-decision continuous-actuation control: balance of an inverted pendulum and pumping a pendulum swing. *Journal of Dynamic Systems, Measurement, and Control* 137, 051012.
- Brecht, M., Hatsopoulos, N.G., Kaneko, T., and Shepherd, G.M. (2013). Motor cortex microcircuits. *Front Neural Circuits* 7, 196.
- Broderick, M.P., Van Gemmert, A.W., Shill, H.A., and Stelmach, G.E. (2009). Hypometria and bradykinesia during drawing movements in individuals with Parkinson's disease. *Experimental brain research* 197, 223-233.
- Brown, A.R., and Teskey, G.C. (2014). Motor cortex is functionally organized as a set of spatially distinct representations for complex movements. *J Neurosci* 34, 13574-13585.
- Cabrera, J.L., and Milton, J.G. (2002). On-off intermittency in a human balancing task. *Physical Review Letters* 89, 158702.
- Collins, J.J., and De Luca, C.J. (1993). Open-loop and closed-loop control of posture: a random-walk analysis of center-of-pressure trajectories. *Experimental brain research* 95, 308-318.
- Cooper, S.E., Martin, J.H., and Ghez, C. (2000). Effects of inactivation of the anterior interpositus nucleus on the kinematic and dynamic control of multijoint movement. *J Neurophysiol* 84, 1988-2000.
- Darling, W.G., Pizzimenti, M.A., and Morecraft, R.J. (2011). Functional recovery following motor cortex lesions in non-human primates: experimental implications for human stroke patients. *Journal of integrative neuroscience* 10, 353-384.
- Desmurget, M., Gaveau, V., Vindras, P., Turner, R.S., Broussolle, E., and Thobois, S. (2004). On-line motor control in patients with Parkinson's disease. *Brain* 127, 1755-1773.

- Desmurget, M., and Turner, R.S. (2008). Testing basal ganglia motor functions through reversible inactivations in the posterior internal globus pallidus. *J Neurophysiol* 99, 1057-1076.
- Doya, K. (1999). What are the computations of the cerebellum, the basal ganglia and the cerebral cortex? *Neural Netw* 12, 961-974.
- Dum, R.P., and Strick, P.L. (2002). Motor areas in the frontal lobe of the primate. *Physiol Behav* 77, 677-682.
- Dupuis, M.J.M., Evrard, F.L., Jacquerye, P.G., Picard, G.R., and Lermen, O.G. (2010). Disappearance of essential tremor after stroke. *Movement Disorders* 25, 2884-2887.
- Ebbesen, C.L., and Brecht, M. (2017). Motor cortex - to act or not to act? *Nat Rev Neurosci* 18, 694-705.
- Erlich, J.C., Brunton, B.W., Duan, C.A., Hanks, T.D., and Brody, C.D. (2015). Distinct effects of prefrontal and parietal cortex inactivations on an accumulation of evidence task in the rat. *Elife* 4.
- Favilla, M., Hening, W., and Ghez, C. (1989). Trajectory control in targeted force impulses. VI. Independent specification of response amplitude and direction. *Exp Brain Res* 75, 280-294.
- Flament, D., Vilis, T., and Hore, J. (1984). Dependence of cerebellar tremor on proprioceptive but not visual feedback. *Experimental neurology* 84, 314-325.
- Flanders, M., and Soechting, J.F. (1990). Parcellation of sensorimotor transformations for arm movements. *J Neurosci* 10, 2420-2427.
- Flash, T., and Hochner, B. (2005). Motor primitives in vertebrates and invertebrates. *Curr Opin Neurobiol* 15, 660-666.
- Flash, T., and Hogan, N. (1985). The coordination of arm movements: an experimentally confirmed mathematical model. *J Neurosci* 5, 1688-1703.
- Fortier, P.A., Kalaska, J.F., and Smith, A.M. (1989). Cerebellar neuronal activity related to whole-arm reaching movements in the monkey. *J Neurophysiol* 62, 198-211.
- Francis, J.T., and Chapin, J.K. (2004). Force field apparatus for investigating movement control in small animals. *IEEE transactions on biomedical engineering* 51, 963-965.
- Fu, Q.-G., Flament, D., Coltz, J., and Ebner, T. (1997). Relationship of cerebellar Purkinje cell simple spike discharge to movement kinematics in the monkey. *Journal of Neurophysiology* 78, 478-491.
- Galinanes, G.L., Bonardi, C., and Huber, D. (2018). Directional Reaching for Water as a Cortex-Dependent Behavioral Framework for Mice. *Cell Rep* 22, 2767-2783.

- Georgopoulos, A.P., Kettner, R.E., and Schwartz, A.B. (1988). Primate motor cortex and free arm movements to visual targets in three-dimensional space. II. Coding of the direction of movement by a neuronal population. *J Neurosci* 8, 2928-2937.
- Giszter, S.F. (2015). Motor primitives--new data and future questions. *Curr Opin Neurobiol* 33, 156-165.
- Golub, M.D., Yu, B.M., Schwartz, A.B., and Chase, S.M. (2014). Motor cortical control of movement speed with implications for brain-machine interface control. *J Neurophysiol*.
- Gowda, S., Overduin, S.A., Chen, M., Chang, Y.H., Tomlin, C.J., and Carmena, J.M. (2015). Accelerating Submovement Decomposition With Search-Space Reduction Heuristics. *IEEE Trans Biomed Eng* 62, 2508-2515.
- Grill, H.J., and Norgren, R. (1978). Neurological tests and behavioral deficits in chronic thalamic and chronic decerebrate rats. *Brain Res* 143, 299-312.
- Guo, J.Z., Graves, A.R., Guo, W.W., Zheng, J., Lee, A., Rodriguez-Gonzalez, J., Li, N., Macklin, J.J., Phillips, J.W., Mensh, B.D., *et al.* (2015). Cortex commands the performance of skilled movement. *Elife* 4, e10774.
- Guo, Z.V., Li, N., Huber, D., Ophir, E., Gutnisky, D., Ting, J.T., Feng, G., and Svoboda, K. (2014). Flow of cortical activity underlying a tactile decision in mice. *Neuron* 81, 179-194.
- Harrison, T.C., Ayling, O.G., and Murphy, T.H. (2012). Distinct cortical circuit mechanisms for complex forelimb movement and motor map topography. *Neuron* 74, 397-409.
- Hoffman, D.S., and Strick, P.L. (1995). Effects of a primary motor cortex lesion on step-tracking movements of the wrist. *J Neurophysiol* 73, 891-895.
- Inzelberg, R., Flash, T., Schechtman, E., and Korczyn, A.D. (1995). Kinematic properties of upper limb trajectories in idiopathic torsion dystonia. *Journal of Neurology, Neurosurgery & Psychiatry* 58, 312-319.
- Inzelberg, R., Plotnik, M., Harpaz, N.K., and Flash, T. (2016). Micrographia, much beyond the writer's hand. *Parkinsonism Relat Disord* 26, 1-9.
- Kaufman, M.T., Churchland, M.M., Ryu, S.I., and Shenoy, K.V. (2014). Cortical activity in the null space: permitting preparation without movement. *Nat Neurosci* 17, 440-448.
- Kawai, R., Markman, T., Poddar, R., Ko, R., Fantana, A.L., Dhawale, A.K., Kampff, A.R., and Olveczky, B.P. (2015). Motor cortex is required for learning but not for executing a motor skill. *Neuron* 86, 800-812.
- Kim, J.S., Park, J.W., Kim, W.J., Kim, H.T., Kim, Y.I., and Lee, K.S. (2006). Disappearance of essential tremor after frontal cortical infarct. *Movement disorders* 21, 1284-1285.

- Kimura, R., Saiki, A., Fujiwara-Tsukamoto, Y., Ohkubo, F., Kitamura, K., Matsuzaki, M., Sakai, Y., and Isomura, Y. (2012). Reinforcing operandum: rapid and reliable learning of skilled forelimb movements by head-fixed rodents. *J Neurophysiol*.
- Larson, C.R., Byrd, K.E., Garthwaite, C.R., and Luschei, E.S. (1980). Alterations in the pattern of mastication after ablations of the lateral precentral cortex in rhesus macaques. *Experimental neurology* 70, 638-651.
- Lawrence, D.G., and Kuypers, H.G. (1968). The functional organization of the motor system in the monkey. I. The effects of bilateral pyramidal lesions. *Brain* 91, 1-14.
- Lemon, R.N. (2008). Descending pathways in motor control. *Annu Rev Neurosci* 31, 195-218.
- Majsak, M.J., Kaminski, T., Gentile, A.M., and Flanagan, J.R. (1998). The reaching movements of patients with Parkinson's disease under self-determined maximal speed and visually cued conditions. *Brain: a journal of neurology* 121, 755-766.
- Manto, M.-U., Setta, F., Jacquy, J., Godaux, E., Hildebrand, J., Roland, H., Blum, S., and Brohee, P. (1998). Different types of cerebellar hypometria associated with a distinct topography of the lesion in cerebellum. *Journal of the neurological sciences* 158, 88-95.
- Martin, J.H., Cooper, S.E., Hacking, A., and Ghez, C. (2000). Differential effects of deep cerebellar nuclei inactivation on reaching and adaptive control. *J Neurophysiol* 83, 1886-1899.
- Mason, C.R., Miller, L.E., Baker, J.F., and Houk, J.C. (1998). Organization of reaching and grasping movements in the primate cerebellar nuclei as revealed by focal muscimol inactivations. *Journal of neurophysiology* 79, 537-554.
- Mathis, M.W., Mathis, A., and Uchida, N. (2017). Somatosensory Cortex Plays an Essential Role in Forelimb Motor Adaptation in Mice. *Neuron* 93, 1493-1503 e1496.
- Milner, T.E. (1992). A model for the generation of movements requiring endpoint precision. *Neuroscience* 49, 487-496.
- Miri, A., Warriner, C.L., Seely, J.S., Elsayed, G.F., Cunningham, J.P., Churchland, M.M., and Jessell, T.M. (2017). Behaviorally Selective Engagement of Short-Latency Effector Pathways by Motor Cortex. *Neuron* 95, 683-696 e611.
- Morandell, K., and Huber, D. (2017). The role of forelimb motor cortex areas in goal directed action in mice. *Sci Rep* 7, 15759.
- Murphy, T.H., Boyd, J.D., Bolanos, F., Vanni, M.P., Silasi, G., Haupt, D., and LeDue, J.M. (2016). High-throughput automated home-cage mesoscopic functional imaging of mouse cortex. *Nat Commun* 7, 11611.

Murray, A.J., Croce, K., Belton, T., Akay, T., and Jessell, T.M. (2018). Balance Control Mediated by Vestibular Circuits Directing Limb Extension or Antagonist Muscle Co-activation. *Cell reports* 22, 1325-1338.

Mussa-Ivaldi, F.A., Giszter, S.F., and Bizzi, E. (1994). Linear combinations of primitives in vertebrate motor control. *Proc Natl Acad Sci U S A* 91, 7534-7538.

Novak, K.E., Miller, L.E., and Houk, J.C. (2002). The use of overlapping submovements in the control of rapid hand movements. *Exp Brain Res* 144, 351-364.

Nudo, R.J. (2013). Recovery after brain injury: mechanisms and principles. *Front Hum Neurosci* 7, 887.

Omrani, M., Kaufman, M.T., Hatsopoulos, N.G., and Cheney, P.D. (2017). Perspectives on classical controversies about the motor cortex. *Journal of neurophysiology* 118, 1828-1848.

Otchy, T.M., Wolff, S.B., Rhee, J.Y., Pehlevan, C., Kawai, R., Kempf, A., Gobes, S.M., and Olveczky, B.P. (2015). Acute off-target effects of neural circuit manipulations. *Nature* 528, 358-363.

Panigrahi, B., Martin, K.A., Li, Y., Graves, A.R., Vollmer, A., Olson, L., Mensh, B.D., Karpova, A.Y., and Dudman, J.T. (2015). Dopamine Is Required for the Neural Representation and Control of Movement Vigor. *Cell* 162, 1418-1430.

Passingham, R., Perry, V., and Wilkinson, F. (1983). The long-term effects of removal of sensorimotor cortex in infant and adult rhesus monkeys. *Brain* 106, 675-705.

Peterka, R. (2002). Sensorimotor integration in human postural control. *Journal of neurophysiology* 88, 1097-1118.

Peterka, R.J. (2000). Postural control model interpretation of stabilogram diffusion analysis. *Biological cybernetics* 82, 335-343.

Peters, A.J., Chen, S.X., and Komiyama, T. (2014). Emergence of reproducible spatiotemporal activity during motor learning. *Nature* 510, 263-267.

Peters, A.J., Liu, H., and Komiyama, T. (2017). Learning in the Rodent Motor Cortex. *Annu Rev Neurosci*.

Poddar, R., Kawai, R., and Olveczky, B.P. (2013). A Fully Automated High-Throughput Training System for Rodents. *PLoS One* 8, e83171.

Pruszynski, J.A., Kurtzer, I., Nashed, J.Y., Omrani, M., Brouwer, B., and Scott, S.H. (2011). Primary motor cortex underlies multi-joint integration for fast feedback control. *Nature* 478, 387-390.

- Rohrer, B., Fasoli, S., Krebs, H.I., Volpe, B., Frontera, W.R., Stein, J., and Hogan, N. (2004). Submovements grow larger, fewer, and more blended during stroke recovery. *Motor Control* 8, 472-483.
- Rohrer, B., and Hogan, N. (2003). Avoiding spurious submovement decompositions: a globally optimal algorithm. *Biol Cybern* 89, 190-199.
- Rouiller, E.M., Moret, V., and Liang, F. (1993). Comparison of the connectional properties of the two forelimb areas of the rat sensorimotor cortex: support for the presence of a premotor or supplementary motor cortical area. *Somatosensory & motor research* 10, 269-289.
- Sanders, J.I., and Kepecs, A. (2012). Choice ball: a response interface for two-choice psychometric discrimination in head-fixed mice. *Journal of neurophysiology* 108, 3416-3423.
- Schwartz, A.B. (2007). Useful signals from motor cortex. *J Physiol* 579, 581-601.
- Scott, S.H. (2003). The role of primary motor cortex in goal-directed movements: insights from neurophysiological studies on non-human primates. *Curr Opin Neurobiol* 13, 671-677.
- Scott, S.H. (2004). Optimal feedback control and the neural basis of volitional motor control. *Nat Rev Neurosci* 5, 532-546.
- Shadmehr, R. (2017). Distinct neural circuits for control of movement vs. holding still. *J Neurophysiol* 117, 1431-1460.
- Shadmehr, R., and Krakauer, J.W. (2008). A computational neuroanatomy for motor control. *Experimental brain research* 185, 359-381.
- Shadmehr, R., and Wise, S.P. (2005). *The Computational Neurobiology of Reaching and Pointing: A Foundation for Motor Learning* (Cambridge, MA: MIT Press).
- Shenoy, K.V., Sahani, M., and Churchland, M.M. (2013). Cortical control of arm movements: a dynamical systems perspective. *Annu Rev Neurosci* 36, 337-359.
- Slutzky, M.W., Jordan, L.R., Bauman, M.J., and Miller, L.E. (2010). A new rodent behavioral paradigm for studying forelimb movement. *J Neurosci Methods* 192, 228-232.
- Sorenson, C.A., and Ellison, G.D. (1970). Striatal organization of feeding behavior in the decorticate rat. *Exp Neurol* 29, 162-174.
- Todorov, E., and Jordan, M.I. (2002). Optimal feedback control as a theory of motor coordination. *Nat Neurosci* 5, 1226-1235.
- Turner, R.S., and Anderson, M.E. (1997). Pallidal discharge related to the kinematics of reaching movements in two dimensions. *J Neurophysiol* 77, 1051-1074.
- Van Gemmert, A., Adler, C.H., and Stelmach, G. (2003). Parkinson's disease patients undershoot target size in handwriting and similar tasks. *Journal of Neurology, Neurosurgery & Psychiatry* 74, 1502-1508.

- Velliste, M., Kennedy, S.D., Schwartz, A.B., Whitford, A.S., Sohn, J.-W., and McMorland, A.J. (2014). Motor cortical correlates of arm resting in the context of a reaching task and implications for prosthetic control. *Journal of Neuroscience* 34, 6011-6022.
- Viviani, P., and Flash, T. (1995). Minimum-jerk, two-thirds power law, and isochrony: converging approaches to movement planning. *Journal of Experimental Psychology: Human Perception and Performance* 21, 32.
- Viviani, P., and McCollum, G. (1983). The relation between linear extent and velocity in drawing movements. *Neuroscience* 10, 211-218.
- Viviani, P., and Terzuolo, C. (1982). Trajectory determines movement dynamics. *Neuroscience* 7, 431-437.
- Wagner, M.J., Kim, T.H., Savall, J., Schnitzer, M.J., and Luo, L. (2017). Cerebellar granule cells encode the expectation of reward. *Nature* 544, 96.
- Walter, J.T., Alvina, K., Womack, M.D., Chevez, C., and Khodakhah, K. (2006). Decreases in the precision of Purkinje cell pacemaking cause cerebellar dysfunction and ataxia. *Nature neuroscience* 9, 389.
- Wang, X., Liu, Y., Li, X., Zhang, Z., Yang, H., Zhang, Y., Williams, P.R., Alwahab, N.S., Kapur, K., and Yu, B. (2017). Deconstruction of Corticospinal Circuits for Goal-Directed Motor Skills. *Cell* 171, 440-455. e414.
- Whishaw, I.Q., and Kolb, B. (1983). Can male decorticate rats copulate? *Behav Neurosci* 97, 270-279.
- Whishaw, I.Q., Schallert, T., and Kolb, B. (1981). An analysis of feeding and sensorimotor abilities of rats after decortication. *Journal of Comparative and Physiological Psychology* 95, 85.
- Wolff, S., and Ölveczky, B. (2018). The promise and perils of causal circuit manipulations. *Current opinion in neurobiology* 49, 84-94.
- Wolpert, D.M., and Kawato, M. (1998). Multiple paired forward and inverse models for motor control. *Neural Netw* 11, 1317-1329.
- Wong, A.L., Haith, A.M., and Krakauer, J.W. (2014). Motor Planning. *Neuroscientist*.
- Woodard, C.L., Bolanos, F., Boyd, J.D., Silasi, G., Murphy, T.H., and Raymond, L.A. (2017). An Automated Home-Cage System to Assess Learning and Performance of a Skilled Motor Task in a Mouse Model of Huntington's Disease. *eNeuro* 4.
- Woodworth, R.S. (1899). The accuracy of voluntary movement (Columbia University.).

Zeiler, S.R., and Krakauer, J.W. (2013). The interaction between training and plasticity in the poststroke brain. *Curr Opin Neurol* 26, 609-616.

APPENDIX

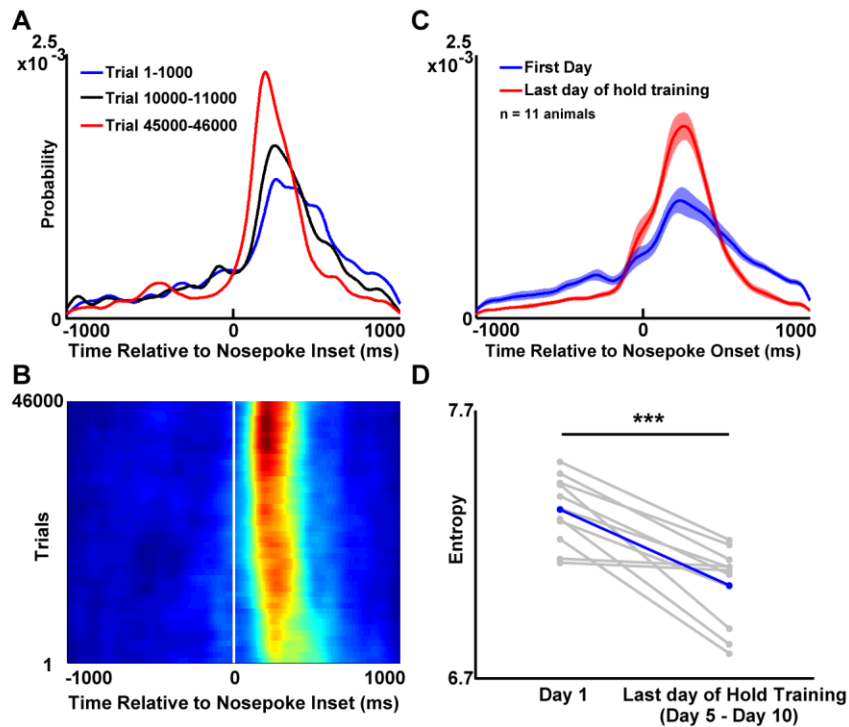


Figure 2.S1. Mice learn to contact the joystick after the nosepoke. Related to Figure 2.2. (A) Probability distribution of time of joystick contact relative to nosepoke onset in an example mouse at early (trials 1-1000, red), intermediate (trials 10000-11000, black) and late stages of training (trials 45000-46000, blue). (B) Evolution of stereotypy in joystick contact time. Distribution of joystick contact times relative to nosepoke onset as a function of trial number. (C) Time of joystick contact relative nosepoke across animals ($n=11$ animals, mean \pm SEM). (D) Entropy of time of the joystick contact relative to nosepoke on Day 1 in the homecage and the last day of hold training (range: 5-10 days later across mice).

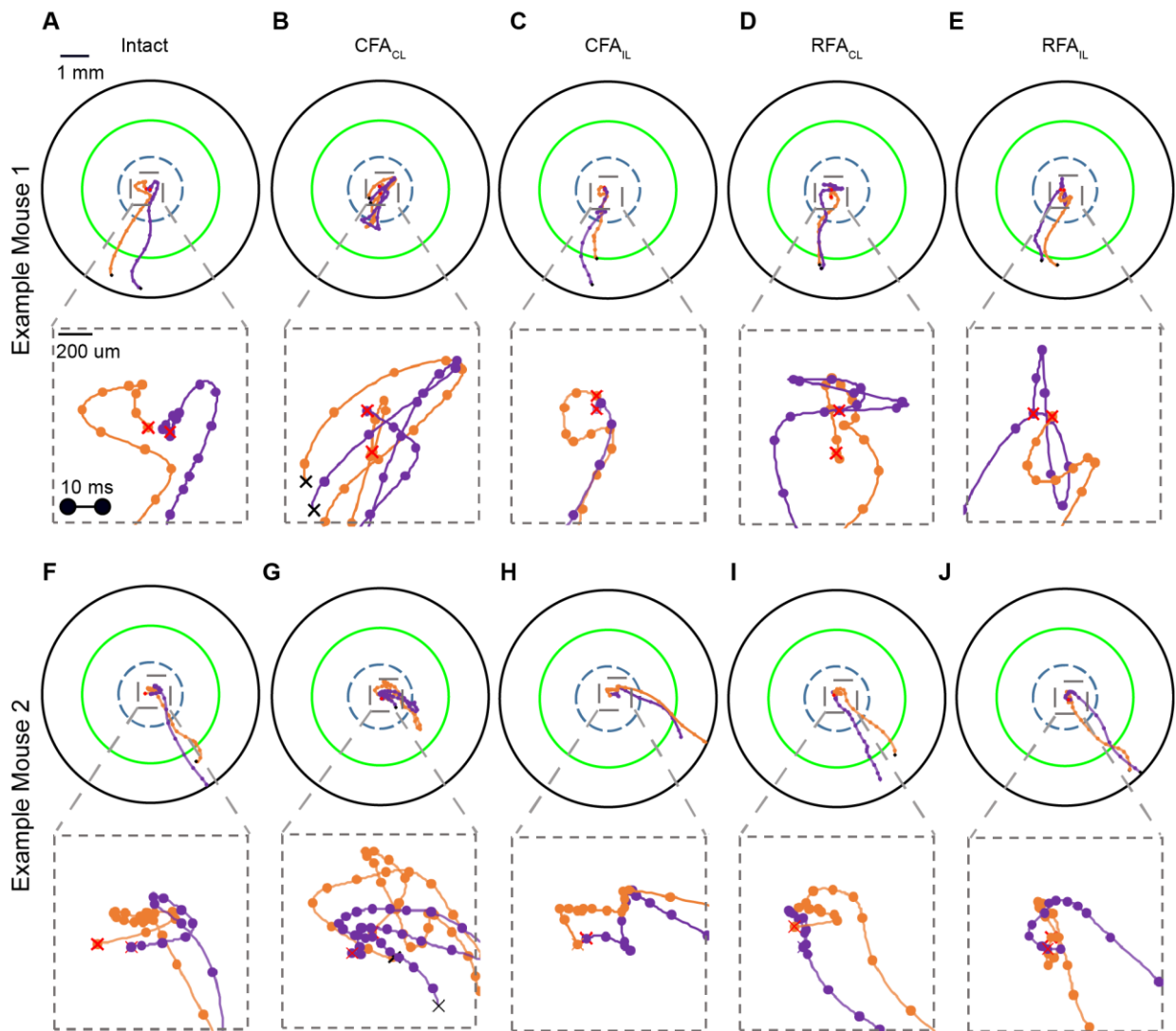


Figure 2.S2. Example trajectories forelimb trajectories. Related to Figure 2.3. (A) Top: Two trajectories (orange and purple) from an example mouse from control trials. Bottom inset: expanded view of micromovements executed during the hold period. (B-E) Data plotted as in A showing example trajectories from the same mouse with CFAcl (B), CFAil (C), RFAcl (D) and RFAil (E). (F-J). Data plotted as in A-E for a different mouse.

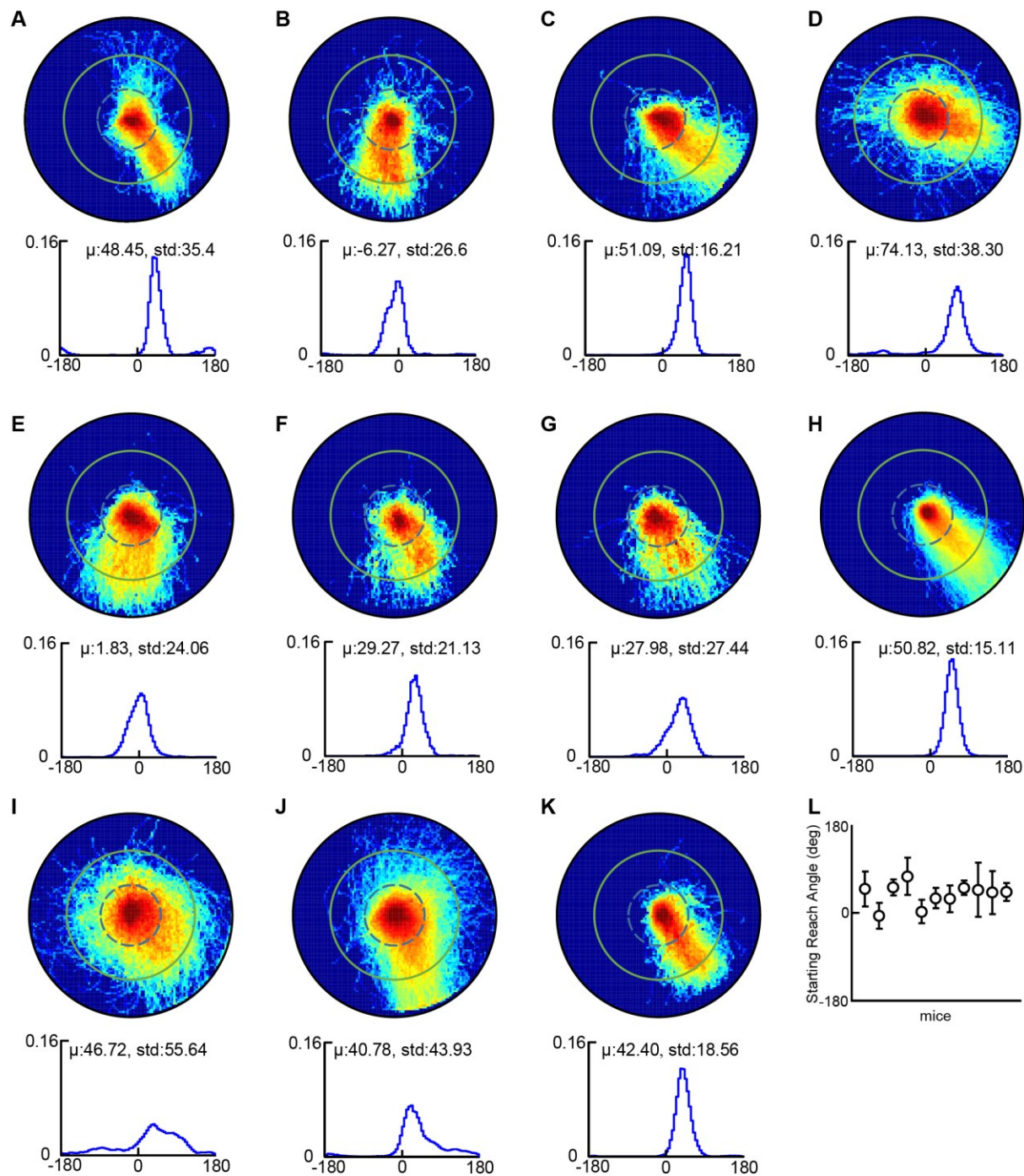


Figure 2.S3. Trajectory patterns exhibited by mice during all-directions-rewarded stage of training. Related to Figure 2.4. (A) Top: Probability density function of all trajectories produced by a single mouse during a single day, immediately after hold training, when all directions were rewarded (green circle indicates reward zone). Bottom: corresponding reach direction distribution (down corresponds to 0 degrees) (bottom). (B-K) Data plotted as in A for all mice in the study. (L)

Reach angles (mean \pm S.D.) produced by each mouse in the study at all-directions-rewarded stage shown in A-K.

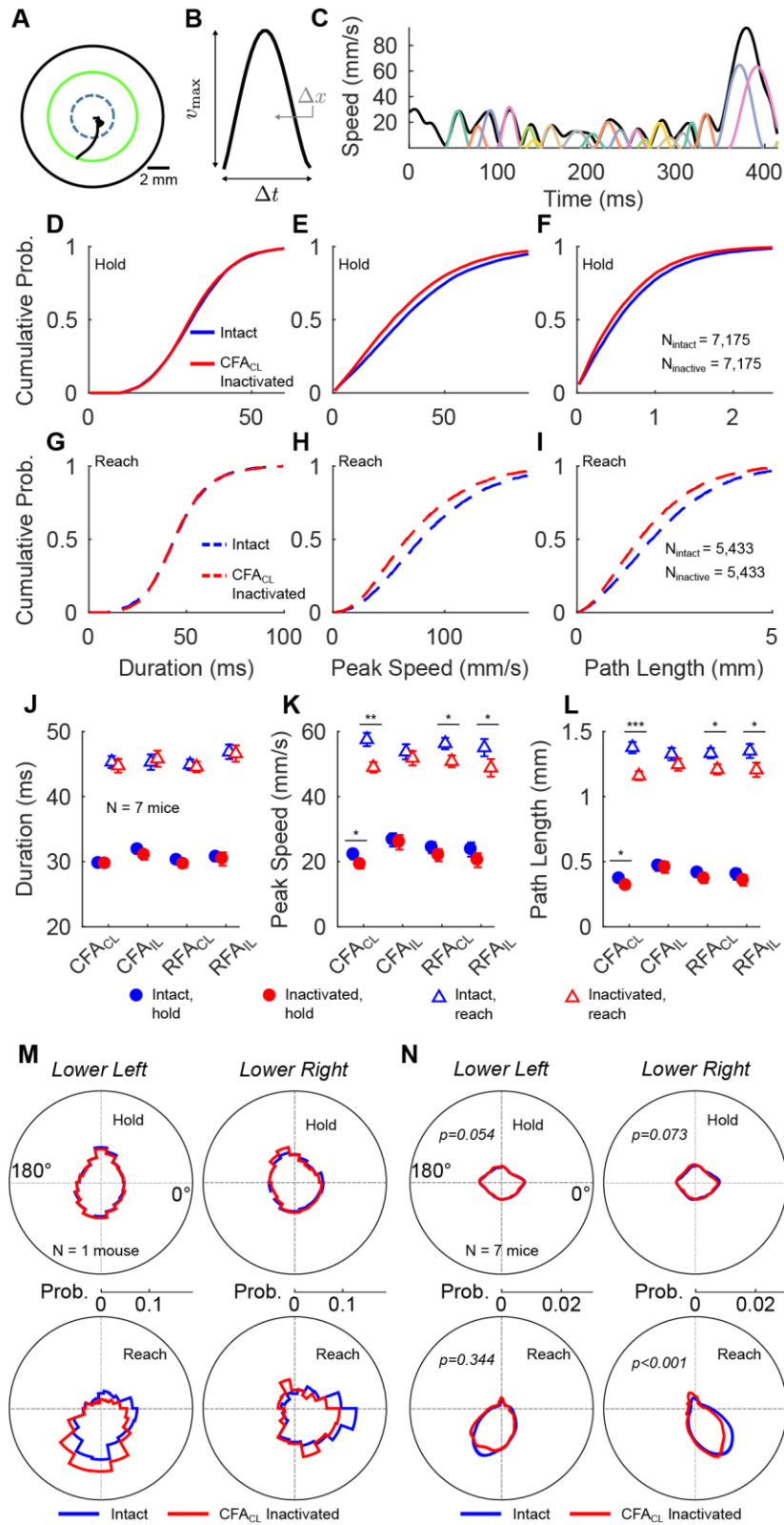


Figure 2.S4. Effect of motor cortical inactivations on the ‘submovement’ class of kinematic primitives. Related to Figure 2.8. (A) Example mouse forelimb trajectory. (B) Example of a

minimum-jerk basis function. (C) Example decomposition of the trajectory in A into minimum jerk basis functions, or submovements, using algorithms previously used in primate studies (Rohrer and Hogan, 2003; Gowda et al, 2016) (see methods). (D-F) Cumulative probability distributions of durations (D), peak speeds (E) and pathlengths (F) of submovements produced within the hold zone. Blue and red traces indicate data intact CFAc1 inactivated trials, respectively. (G-I) Distributions plotted as in D-F for submovements that transected the outer radius. (J-L) Mean \pm SEM of duration (J), peak speed (K) and pathlength (L) with (red) and without (blue) inactivation of various motor cortical areas for hold (circle) and reach (triangle) segments. (M) Direction distributions of hold (top) and reach (bottom) submovements for an example mouse in intact (blue) and CFAc1 inactivated (red) trials. (N) Data plotted as in M with average direction distributions across animals (n=7).

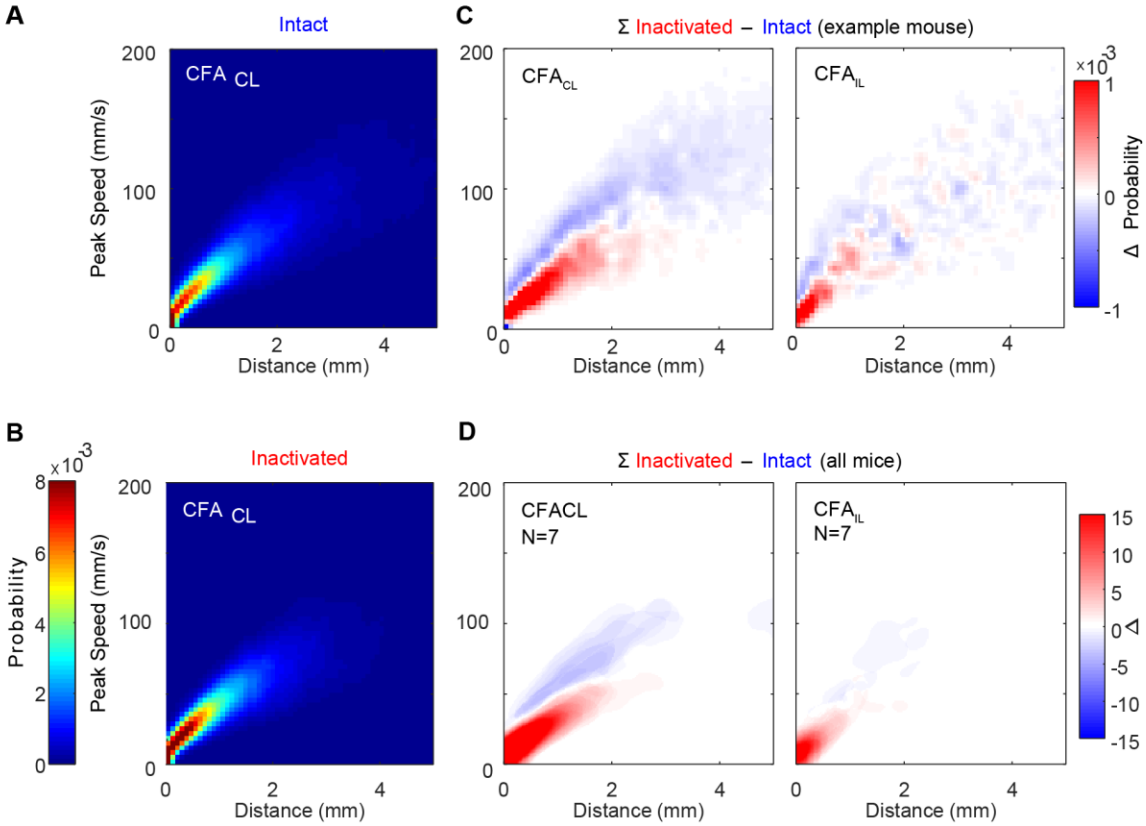


Figure 2.S5. Segment pathlength is predicted by its peak speed. Related to Figure 2.8. (A-B) Joint probability distributions of segment pathlength and peak speed in intact (A) and CFAcl inactivated (B) trials for an example mouse. (C) Difference between joint distributions of intact and inactivated trials for an example mouse (CFAcl left, CFAil right). (D) Data plotted as in C, overlaying difference histograms across all mice (n=7).

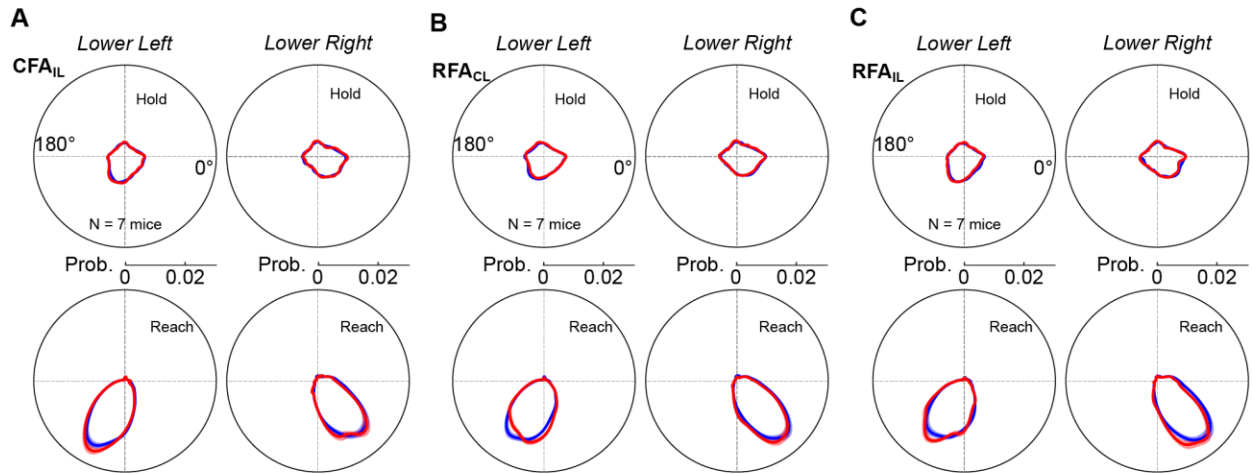


Figure 2.S6. Impact of cortical inactivations on segment directions. Related to Figure 2.8. (A) Direction distributions of hold (top) and reach (bottom) segments for all mice in intact (blue) and CFAil inactivated (red) trials. (B-C) Data plotted as in A for RFAcl (B) and RFAil (C) dataset.

Table 2.1: Probability of a successful hold (LME)

Probability of successful hold ~ $1 + Laser + (1 | Mouse) + (1 | Mouse:Day)$

	Term	Estimate	Standard Error	pValue of ttest
CFAc 1	Intercept	0.3815	0.0723	1.62E-05
	Laser	0.1099	0.0457	0.0237
CFAil	Intercept	0.3826	0.0925	3.26E-04
	Laser	0.0657	0.041	0.1213
RFAc 1	Intercept	0.3742	0.0894	2.89E-04
	Laser	0.0097	0.0466	0.8369
RFAil	Intercept	0.3764	0.0887	2.48E-04
	Laser	0.0472	0.0475	0.3292

Table 2.2: Slope of SDF function				
Implant	Condition	Mean	SEM	Pval of paired t-test
CFAcl	Intact	1.957	0.0028	0.0022
	Laser	1.966	0.0027	
CFAil	Intact	1.953	0.00289	0.699
	Laser	1.955	0.00540	
RFAcl	Intact	1.955	0.00542	0.978
	Laser	1.955	0.00433	
RFAil	Intact	1.955	0.00544	0.611
	Laser	1.953	0.00255	

Table 2.3: Transition point of SDF function				
Implant	Condition	Mean	SEM	Pval of paired t-test
CFAcl	Intact	27.59786	1.56805 6	9.92E-05
	Laser	32.4554	1.77308 5	
CFAil	Intact	26.38059	2.21787 2	0.098023
	Laser	28.12336	2.35663 6	
RFAcl	Intact	26.92599	2.13988 8	0.146999
	Laser	28.41068	2.53878 6	
RFAil	Intact	27.26027	2.19139 4	0.322409
	Laser	28.21111	2.17547 6	

Table 2.4: Offsets of SDF function (log)				
Implant	Condition	Mean	SEM	Pval of paired t-test
CFAcl	Intact	8.12e-04	1.47e-04	0.0012
	Laser	5.98e-04	1.09e-04	
CFAil	Intact	8.96e-04	2.01e-04	0.340
	Laser	8.63e-04	2.07e-04	
RFAcl	Intact	8.4e-04	1.64e-04	0.021
	Laser	6.7e-04	1.98e-04	
RFAil	Intact	8.26e-04	1.69e-04	0.023
	Laser	6.48e-04	1.85e-04	

Table 2.5: Probability of transecting outer radius (4mm), LME model				
<i>Probability of transecting outer radius ~ 1 + Laser* + (1 Mouse) + (1 Mouse:Day)</i>				
	Term	Estimate	Standard Error	pValue of ttest
CFAcl	Intercept	0.6706	0.0255	6.16E-40
	Laser	-0.1908	0.0239	1.17E-11
CFAil	Intercept	0.7409	0.033	1.91E-26
	Laser	0.018	0.0104	0.0914
RFAcl	Intercept	0.7179	0.0311	1.99E-34
	Laser	-0.0053	0.0073	0.4683
RFAil	Intercept	0.71831499	0.022468451	4.60E-33
	Laser	-0.0039307	0.013062648	0.765

Table 2.6: Peak Speed of trajectories (mm/s), LME model				
<i>Peak Speed ~ I + Laser + (I Mouse) + (I Mouse:Day)</i>				
	Term	Estimate	Standard Error	pValue of ttest
CFAcl	Intercept	115.9873	7.82	3.85E-24
	Laser	-21.0618	1.8242	2.17E-18
CFAil	Intercept	121.8371	8.798	5.06E-18
	Laser	-4.5188	1.5344	0.0051
RFAcl	Intercept	119.198	9.956	1.32E-18
	Laser	-8.4271	1.423	1.21E-07
RFAil	Intercept	117.8757	9.8914	1.16E-15
	Laser	-9.9938	1.574	8.66E-08

Table 2.7: Angle of trajectory (degrees), LME model

$$Angle \sim 1 + Laser + Direction + (1 | Mouse) + (1 | Mouse:Day)$$

	Term	Estimate	SE	pValue of ttest
CFAcl	Intercept	-92.8197	12.0587	1.52E-07
	Direction	77.2378	5.1366	1.03E-12
	Laser	-4.5339	5.1366	0.3874
CFAil	Intercept	- 101.2771	10.8302	6.19E-09
	Direction	78.7517	5.6466	4.34E-12
	Laser	0.3694	5.6466	0.9485
RFAcl	Intercept	-97.2651	10.4994	7.26E-09
	Direction	77.5466	5.0024	5.69E-13
	Laser	-0.5092	5.0024	0.9199
RFAil	Intercept	-94.7543	10.7913	1.79E-08
	Direction	76.6175	4.8685	4.25E-13
	Laser	-3.1483	4.8685	0.5249

Table 2.8: StdDev of Reach Angle for trajectory (degree)				
	Laser	Mean Std Dev of Angle	SEM	pValue of paired ttest
CFAcl	off	33.97343034	4.37539	p = 0.9945
	on	33.96230309	4.35355	
CFAil	off	29.93535776	3.52972	p = 0.5823
	on	27.98774658	2.91409	
RFAcl	off	29.19536116	3.68252	p = 0.8809
	on	29.25396581	3.66252	
RFAil	off	29.0139461	4.27275	p = 0.4444
	on	28.48927885	4.50755	

Table 2.9: Duration of segments (milliseconds), LME model				
<i>Duration ~ 1 + Laser*Condition + (1 Mouse) + (1 Mouse:Day)</i>				
	Model Term	Estimate	SE	pValue of ttest
CFAcl	Intercept	34.057	2.8549	1.43E-23
	Laser (hold)	-1.5385	1.7015	0.36733
	Laser (reach)	-0.16667	1.7015	0.9221
	Condition (reach vs hold)	28.41	1.7015	3.30E-36
	Laser:Condition (interaction)	1.3718	2.4063	0.56946
CFAil	Intercept	35.563	3.6848	8.35E-16
	Laser (hold)	0.14	2.622	0.95753
	Laser (reach)	0.96	2.622	0.71507
	Condition (reach vs hold)	29.56	2.622	2.82E-19
	Laser:Condition (interaction)	0.82	3.7081	0.82545
RFAcl	Intercept	33.834	3.0082	1.86E-21
	Laser (hold)	-1.4595	1.7568	0.4075
	Laser (reach)	-0.25676	1.7568	0.88401
	Condition (reach vs hold)	29.77	1.7568	4.15E-36
	Laser:Condition (interaction)	1.2027	2.4846	0.62907
RFAil	Intercept	34.061	3.4471	6.31E-16
	Laser (hold)	0.34783	2.7918	0.90113
	Laser (reach)	2.5	2.7918	0.37297

	Condition (reach vs hold)	31.065	2.7918	1.81E-18
	Laser:Condition (interaction)	2.1522	3.9482	0.58706

Table 2.10: Peak speed of segments (mm/s), LME model

$$Peak\ Speed \sim I + Laser * Condition + (I | Mouse) + (I | Mouse : Day)$$

	Model Term	Estimate	SE	pValue of ttest
CFAcl	Intercept	34.495	3.7575	2.94E-16
	Laser (hold)	-8.6013	1.7962	3.95E-06
	Laser (reach)	-10.428	1.7962	3.62E-08
	Condition (reach vs hold)	59.541	1.7962	1.87E-71
	Laser:Condition (interaction)	-1.8268	2.5402	0.47316
CFAil	Intercept	39.371	4.5833	1.58E-13
	Laser (hold)	0.87282	2.6842	0.74576
	Laser (reach)	-4.9183	2.6842	0.070007
	Condition (reach vs hold)	52.219	2.6842	4.45E-35
	Laser:Condition (interaction)	-5.7911	3.796	0.13041
RFAcl	Intercept	34.993	5.3427	9.52E-10
	Laser (hold)	-4.7965	2.479	0.054967
	Laser (reach)	-7.384	2.479	0.0033985
	Condition (reach vs hold)	58.03	2.479	6.13E-51
	Laser:Condition (interaction)	-2.5875	3.5058	0.46167

RFAil	Intercept	38.001	4.9875	2.76E-11
	Laser (hold)	-4.1481	2.7809	0.13937
	Laser (reach)	-8.4982	2.7809	0.00297
	Condition (reach vs hold)	55.046	2.7809	3.64E-34
	Laser:Condition (interaction)	-4.3501	3.9328	0.27169

Table 2.11: Path length of segments (mm), LME model				
<i>Path Length ~ I + Laser*Condition + (I Mouse) + (I Mouse:Day)</i>				
	Model Term	Estimate	SE	pValue of ttest
CFAcl	Intercept	0.8393	0.15934	4.65E-07
	Laser (hold)	-0.22265	0.10844	0.041768
	Laser (reach)	-0.49128	0.10844	0.000011833
	Condition (reach vs hold)	2.9877	0.10844	5.52E-61
	Laser:Condition (interaction)	-0.26863	0.15336	0.081844
CFAil	Intercept	1.0139	0.16868	3.32E-08
	Laser (hold)	0.0081177	0.14906	0.95668
	Laser (reach)	-0.076229	0.14906	0.61026
	Condition (reach vs hold)	2.7779	0.14906	1.17E-33
	Laser:Condition (interaction)	-0.084347	0.21081	0.68996
RFAcl	Intercept	0.8777	0.19372	0.000012245
	Laser (hold)	-0.1234	0.11648	0.2912

	Laser (reach)	-0.32152	0.11648	0.0065281
	Condition (reach vs hold)	2.9168	0.11648	2.51E-54
	Laser:Condition (interaction)	-0.19812	0.16473	0.23108
RFAil	Intercept	0.92915	0.16365	1.73E-07
	Laser (hold)	-0.071143	0.12195	0.56112
	Laser (reach)	-0.29834	0.12195	0.016415
	Condition (reach vs hold)	2.9244	0.12195	2.32E-40
	Laser:Condition (interaction)	-0.22719	0.17246	0.19113

Table 2.12: Segment direction, Watson U^2 statistic			
	Reward Direction	Condition (reach v hold)	p value
CFAcl	Lower Right	hold	1.15E-04
	Lower Left	hold	0.0057
	Lower Right	reach	0.0608
	Lower Left	reach	0.515
CFAil	Lower Right	hold	0.4872
	Lower Left	hold	0.8818
	Lower Right	reach	0.4761
	Lower Left	reach	0.3515
RFAcl	Lower Right	hold	0.1768
	Lower Left	hold	0.3543

	Lower Right	reach	0.0908
	Lower Left	reach	0.2921
RFail	Lower Right	hold	0.2266
	Lower Left	hold	0.2252
	Lower Right	reach	0.7528
	Lower Left	reach	0.6787

Table 2.13: Segment tortuosity, LME model				
<i>Tortuosity ~ I + Laser + (I Mouse)</i>				
	Model Term	Estimate	SE	p value of ttest
CFAcl	Intercept	1.1766	0.0061316	1.04E-102
	Laser	0.0081169	0.005917	0.17422
CFAil	Intercept	1.1753	0.007764	5.54E-66
	Laser	-0.0060958	0.0061618	0.32748
RFAcl	Intercept	1.1724	0.0050784	4.51E-105
	Laser	-0.0062216	0.0041455	0.13777
RFAil	Intercept	1.1856	0.0082281	1.71E-60
	Laser	-0.0085329	0.0082743	0.30806

Table 2.14: Segment number of acceleration peaks, LME model				
<i>Number of Acceleration Peaks ~ 1 + Laser + (1 Mouse)</i>				
	Model Term	Estimate	SE	p value of ttest
CFAcl	Intercept	1.7569	0.048372	8.84E-50
	Laser	-0.023322	0.019195	0.22812
CFAil	Intercept	1.7952	0.055241	2.43E-34
	Laser	0.032804	0.020123	0.10961
RFAcl	Intercept	1.7645	0.050505	6.85E-47
	Laser	0.0020228	0.017516	0.90838
RFAil	Intercept	1.7933	0.055104	2.02E-32
	Laser	0.013118	0.030703	0.67128

Table 2.15: Fraction of overlapping submovements (OSMs), Wilcoxon rank sum test	
	p value
CFAcl	0.19524
CFAil	0.06185
RFAcl	0.08186
RFAil	0.88003

Table 2.16: Submovement duration, Wilcoxon rank sum test		
	Condition (reach v hold)	p value
CFAcl	hold	0.49137
	reach	0.31859
CFAil	hold	0.28021
	reach	0.57837
RFAcl	hold	0.20225
	reach	0.41309
RFAil	hold	0.29862
	reach	0.42025

Table 2.17: Submovement velocity, Wilcoxon rank sum test

	Condition (reach v hold)	p value
CFAcl	hold	0.039819
	reach	0.0016283
CFAil	hold	0.43024
	reach	0.29142
RFAcl	hold	0.12417
	reach	0.011623
RFAil	hold	0.15715
	reach	0.045952

Table 2.18: Submovement path length, Wilcoxon rank sum test		
	Condition (reach v hold)	p value
CFAcl	hold	0.039819
	reach	0.00036394
CFAil	hold	0.43889
	reach	0.18386
RFAcl	hold	0.098607
	reach	0.019922
RFAil	hold	0.21775
	reach	0.022086

Table 2.19: Submovement direction, Watson U2 statistic			
	Reward Direction	Condition (reach v hold)	p value
CFAcl	Lower Right	hold	0.0536
	Lower Left	hold	0.0728
	Lower Right	reach	0.000987
	Lower Left	reach	0.344
CFAil	Lower Right	hold	0.6753
	Lower Left	hold	0.7345
	Lower Right	reach	0.7981
	Lower Left	reach	0.2914
RFAcl	Lower Right	hold	0.5678
	Lower Left	hold	0.482
	Lower Right	reach	0.1347
	Lower Left	reach	0.453
RFAil	Lower Right	hold	0.4111
	Lower Left	hold	0.1132
	Lower Right	reach	0.6452
	Lower Left	reach	0.4869

CHAPTER 3

TONGUE KINEMATICS REVEAL CORTEX-DEPENDENT CORRECTIONS AS THE MOUSE TONGUE REACHES FOR, AND MISSES, TARGETS

Abstract

Precise control of the tongue is necessary for drinking, eating, and vocalizing (Guenther, 1995; Kier and Smith, 1985). Yet because tongue movements are fast and difficult to resolve, neural control of lingual kinematics remains poorly understood. We combine kilohertz frame-rate control of lingual kinematics remains poorly understood. We combine kilohertz frame-rate imaging and a deep learning based artificial neural network to resolve 3D tongue kinematics in mice performing a cued lick task. Cue-evoked licks exhibit previously unobserved fine-scale movements which, like a hand searching for an unseen object (Ghez et al., 1995b; Khan and Franks, 2003; Meyer et al., 1988; Spijkers and Lochner, 1994), were produced after tongue protrusions and were directionally biased towards remembered locations. Photoinhibition of anterolateral motor cortex (ALM) abolished these fine-scale adjustments, resulting in well-aimed but hypometric licks that missed the spout. Our results show that cortical activity is required for online corrections during licking and reveal novel, limb-like dynamics of the mouse tongue as it reaches for, and misses, targets.

Introduction

When you reach for an unseen object on a table in front of you, how do you move your hand to make contact? Reaches towards unseen targets exhibit variable trajectories that include initial guesses followed by ‘corrective submovements’ after misses (Ghez et al., 1995b; Khan and Franks, 2003; Meyer et al., 1988; Spijkers and Lochner, 1994). Sensorimotor noise reduces movement accuracy (Faisal et al., 2008), and successfully directing submovements to a small or unseen target requires motor commands to be derived from online estimates of both current hand

position and target location(Ghez et al., 1995b; Khan and Franks, 2003; Meyer et al., 1988; Spijkers and Lochner, 1994).

Many animals, including humans and rodents, have prehensile tongues that act external to the oral cavity to contact objects such as food, water and conspecifics(Kier and Smith, 1985). During natural behaviors such as licking, eating and grooming, tongues must precisely contact unseen targets. Coherent speech relies on online feedback control(Guenther, 1995), but it remains unknown if non-vocal learners such as rodents use online control mechanisms to aim their tongues. For example, when a mouse licks at an unseen water spout, does its tongue, like a hand, produce corrective submovements online after misses to zero in on the spout?

Identifying motor control principles requires precise quantification of moment-to-moment movement kinematics, but lingual kinematics are difficult to resolve because tongues are complicated, deformable effectors that move extremely fast(Kier and Smith, 1985). Even in tractable model systems such as rodents, where licking is used to study principles of motor initiation, learning, planning, and decision making(Coddington and Dudman, 2018; Crochet et al., 2019; Gaffield and Christie, 2017; Goard et al., 2016; Komiyama et al., 2010; Svoboda and Li, 2018; Welsh et al., 1995), licks are usually measured as a binary register of whether or not a tongue contacts a spout or transects an IR beam(Goard et al., 2016; Komiyama et al., 2010) or with single plane imaging(Gaffield and Christie, 2017; Welsh et al., 1995). Remarkably, it remains unclear how exactly the tongue moves during rodent licking.

Results

To precisely resolve 3D tongue kinematics, we imaged the tongue at 1 kHz in two planes and trained a deep learning based artificial neural network(Ronneberger et al., 2015) to identify and segment the tongue from side and bottom views at all phases of a lick cycle (Figure 3.1A-

E)(Methods). Using hull reconstruction to build a 3D model of the tongue(Beatus et al., 2015), we estimated the tongue tip for each frame of the lick to achieve millisecond timescale resolution of the tongue tip trajectory (Figure 3.1F, Figure 3.S1)(Methods). Mice were trained to withhold licking for at least 1 second to earn an auditory cue, and then to produce a cue-evoked lick within 1.3 seconds to earn a water reward (Figure 3.1A)(Methods). Cues evoked bouts of licking, as previously observed in head-fixed mouse setups where the spout could not be directly seen (Figure 3.1B, Inter spout contact interval: $150\text{ms}\pm 11\text{ms}$, Inter lick interval: $142\pm 5\text{ms}$, $n = 9$ animals) (Gaffield and Christie, 2017; Komiyama et al., 2010). We defined ‘cue-evoked licks’ as licks initiated before first spout contact and ‘water-retrieval licks’ as licks initiated after the first tongue-spout contact in a bout(Coddington and Dudman, 2018)(Figure 3.1A, G-H).

Consistent with the idea that water-tongue contact can trigger brainstem central pattern generators (CPGs) to produce alternating phases of tongue protrusion and retraction(McElvain et al., 2018), water-retrieval licks exhibited highly stereotyped kinematics, consisting of a single protrusion phase and a single retraction phase with no fine-scale movements in between (Figure 3.1G,H, Figure 3.S2, Table 3.1)(Methods) (Protrusion duration, peak speed, pathlength: 32ms [30 33], 308.12 mm/s [301.60 310.95], 4.7 mm [4.59 5.29]; Retraction: 32ms [32 34], 349.86 mm/s [345.63 354.66], 6.43 mm [6.43 6.49]; Latency from protrusion offset to retrieval onset: 0ms [0 0]; medians [IQRs] $n = 9$ animals).

In contrast to these ‘water-retrieval licks’, the first cue-evoked licks of each bout, initiated before spout contact, exhibited highly complex trajectories with longer durations and more acceleration peaks (Figure 3.1G,H, Figure 3.S2, Table 3.1)(Methods)(Durations, cued: 113ms [112 115] vs. retrieval: 70ms [69 76]; acceleration peaks, cued: 6 [5 6] vs retrieval: 4 [4 4], medians [IQR], $p < 0.05$ for all comparisons, $n = 9$ animals, Wilcoxon signed rank test). Cued

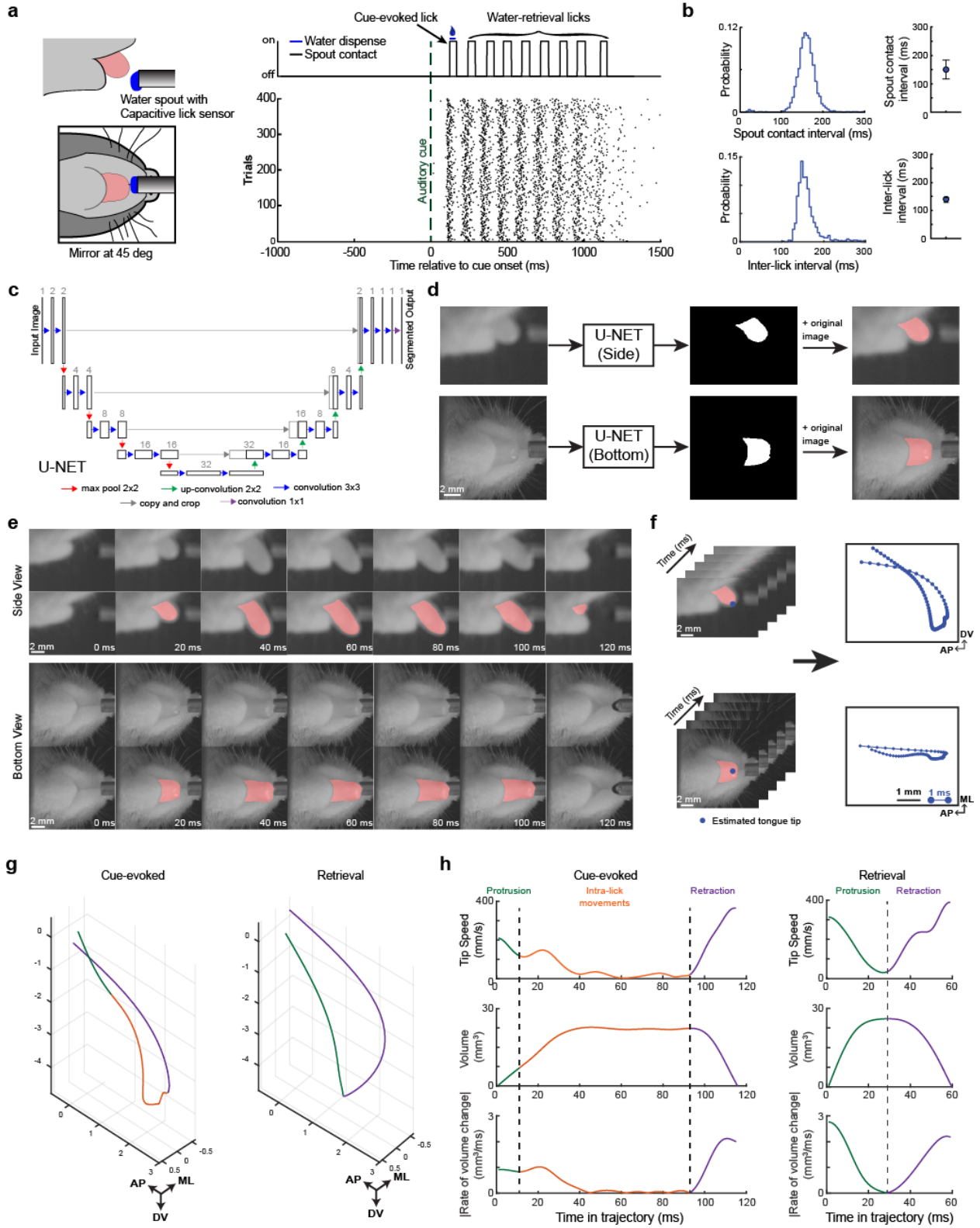


Figure. 3.1 Machine vision based tracking of lingual kinematics identifies intra-lick movements important for spout contact.

a) Left, the tongue was filmed at kilohertz framerate in two planes (from the side and, via a mirror, from the bottom) during a cued lick task. Right, spout contacts as a function of time for a single trial (top) and lick raster showing spout contact onset times across 400 trials (bottom). Water was dispensed at the moment of first spout contact. We defined cue-evoked licks as those initiated before first spout contact in a trial and water-retrieval licks as ones initiated after.

b) Left: Distributions of inter-spout contact intervals (top) and inter-lick protrusion intervals (bottom) for a single mouse. Right: median±interquartile range (IQR) values across 9 mice.

c) Architecture of the artificial neural network (U-NET) used to segment the tongue from the background image. U-NET has characteristic symmetrical contraction and expansion paths that simultaneously capture localization and image context. Each box corresponds to a multi-channel feature map and numbers above each layer indicate the number of channels; color-coded arrows indicate sequential processing steps.

d) Pipeline for tongue segmentation. Left to right, top: side view of the tongue as the input image to U-NET, the identified tongue mask, and the mask plus the input image. Bottom: process is repeated separately for the bottom view of the tongue.

e) Example frames from side and bottom views across a single lick cycle. Each row shows the raw image above the image overlaid with the U-NET labeled tongue mask.

f) Tongue tip positions, computed from a 3D tongue model (Extended data fig. 1), were estimated in each frame (left), resulting in millisecond timescale tracking of tongue tip in two planes

g) Trajectories from two planes were converted into a 3D trajectory of a single cue-evoked lick (left) and water-retrieval lick (right). Protrusion, retraction, and intra-lick movement phases of the lick are labeled in green, purple and orange, respectively.

h) Top to bottom: Tip speed, tongue volume, and absolute value of rate of tongue volume change for the cue-evoked and retrieval licks shown in G. Protrusion offsets and retraction onsets were defined as the first and last minima in the rate of volume change (vertical dotted lines). Note that the cue-evoked lick contained ILMs (orange) between protrusion offset and retraction onset, whereas retrieval licks exhibited a single minimum in rate of volume change, marking the transition from protrusion to retraction.

licks also exhibited significantly more trial-by-trial variability (Table 3.1, Figure 3.S2l). Examination of cued lick trajectories revealed that the initial tongue protrusion almost never reached the spout (Probability of contact on protrusion: 0.1 ± 0.06 , $n = 9$ animals, Figure 3.S3g). After the protrusion, the animal initiated additional fine-scale tongue movements prior to retracting. These ‘intra-lick movements’ (ILMs) were too fast to be visually identifiable in real-time videos but were clearly visible in slow-motion (Movie S1).

When primates reach to unseen targets, corrective submovements initiated after an initial miss ensure endpoint accuracy, and their number is correlated with latency to target contact (Ghez et al., 1995b; Meyer et al., 1988). Similarly, ILMs terminated at precisely clustered tongue tip positions beneath the spout (endpoint accuracy, defined as standard deviation of the tongue tip position at moment of retraction onset across trials: 0.195 ± 0.03 mm M/L, 0.31 ± 0.03 mm A/P, and 0.76 ± 0.07 mm D/V, Figure 3.S3 and Supplemental Text)(Methods). Further, the number of acceleration peaks per ILM strongly predicted cue-to-spout contact latencies (Figure 3.S4, r -square: $0.83 [0.68 \ 0.85]$, $p < 0.001$, F-test, (9/9) animals)(Methods). These data show that previously unresolved tongue movements within a lick are important for making spout contact. These within-lick adjustments also exhibit some phenomenological similarities to corrective submovements observed in primate reach studies (Ghez et al., 1995b; Khan and Franks, 2003; Meyer et al., 1988; Spijkers and Lochner, 1994).

Why did cue-evoked licks contain ILMs while subsequent water-retrieval ones did not? One possibility is that reduction in lick complexity is pre-programmed into the bout motor plan. Alternatively, the moment of first tongue-spout contact in a bout could clarify the spout’s position in space and rapidly update the next lick’s motor plan, in the same way that, for example, even brief visual feedback at the end of a non-visually guided reach can clarify target position and

increase the accuracy of a subsequent reach, obviating the need for corrective submovements (Khan and Franks, 2003; Spijkers and Lochner, 1994). Occasionally, the first one or two cue evoked licks failed to make spout contact, providing an opportunity to test how the first contact affects the next lick (Probability of spout contact on first cue evoked lick: 0.63 ± 0.08 , $n=9$ animals). Licks preceding first contact always exhibited ILMs, whereas licks following first contact always lacked them, independent of when in the lick bout the first contact was made (Figure 3.S5). Thus, the first spout contact facilitated the transition to stereotyped and well-aimed retrieval licks, suggesting that spout contact updates the motor plan for the ensuing retrieval lick. Note that any update to an ensuing lick's motor plan must occur in the brief interval between the first spout contact and the ensuing protrusion onset (Latency between spout contact and subsequent protrusion: 94.5ms [87.5 109.5], $n = 9$ animals). The return to variable cue-evoked licks by the next trial >1 second later also suggests that the precision of the 'memory' of spout location degrades on second timescales, as in memory-guided reach tasks (Heath and Westwood, 2003; McIntyre et al., 1997).

To test cortical roles in the new kinematics we describe, we used VGAT-hChR2-EYFP mice to photoinactivate anterolateral (ALM) or posterior medial (PMM) motor cortical areas (Methods), two non-overlapping regions with functional projections to brainstem lingual circuits (Komiyama et al., 2010; McElvain et al., 2018) (Figure 3.2a). Photoinhibition of ALM, but not PMM, impaired spout contact (Figure 3.2b, Figure 3.S6, Probability of contact: intact: 1 [1 1] vs ALM inactivated: 0.03 [0.03 0.13] $p < 0.05$, $n = 9$ animals, Wilcoxon signed rank test; probability of contact, intact: 1 [1 1] vs PMM inactivated: 1 [1 1] $p > 0.05$, $n = 9$ animals, Wilcoxon signed rank test), consistent with previous studies (Goard et al., 2016; Svoboda and Li, 2018).

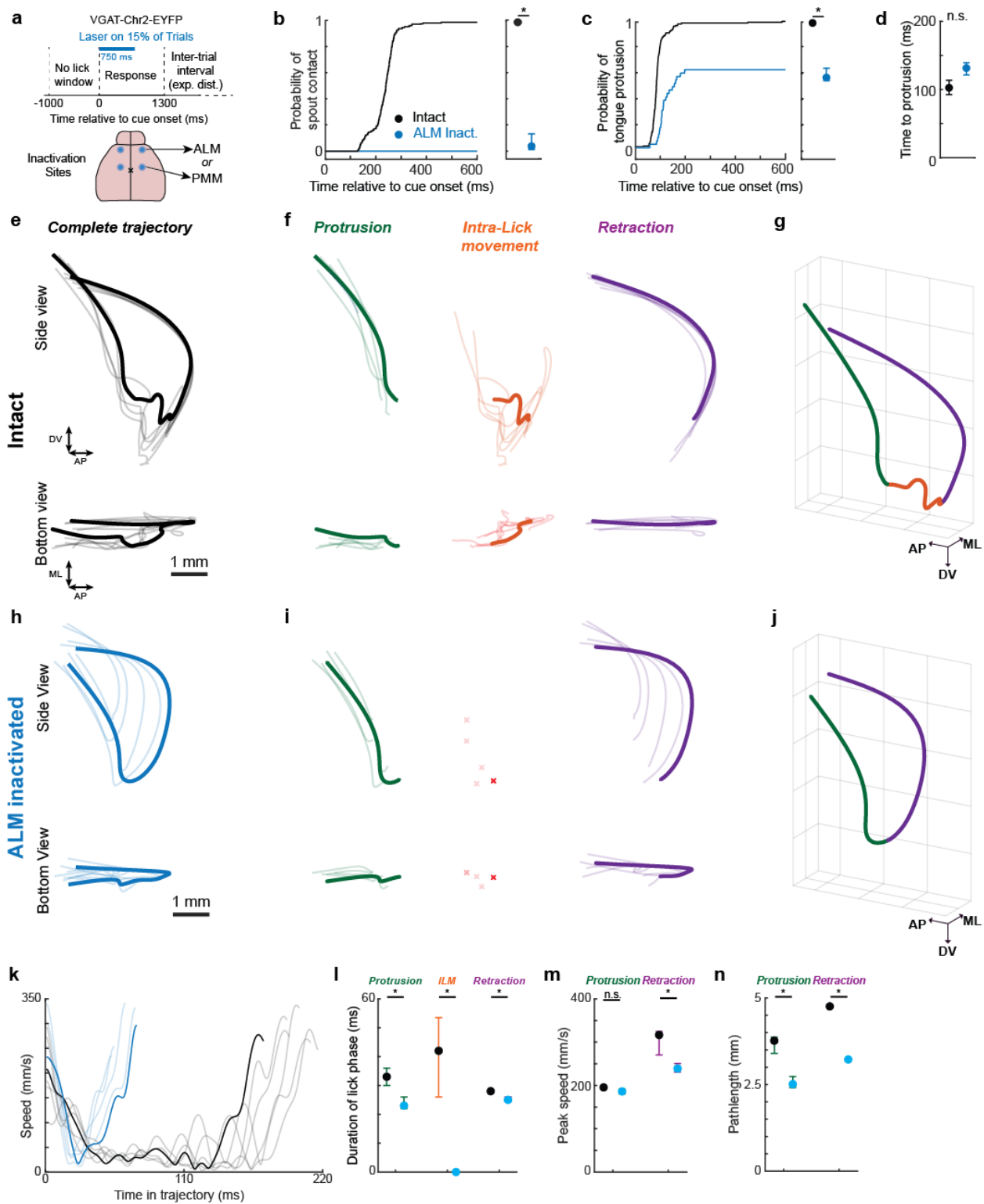


Figure 3.2. Photoinactivation of ALM impairs spout contact by abolishing intra-lick movements.

- a) ALM or PMM were bilaterally photoinactivated on 15% of randomly interleaved trials.
- b) Cumulative probability of tongue-spout contact relative to cue onset during laser-off and ALM-photoinactivated trials. Right, median \pm IQR probability of spout contact within a trial across mice (n=9 mice).
- c) Data plotted as in (b) for onsets of tongue protrusions.
- d) Median latency from cue onset to tongue protrusion onset across animal (errorbars, IQRs, n=9 mice)
- e-g Laser-off trials ('intact'). e) Six overlaid tongue tip trajectories during cue-evoked licks. A single lick is bold for clarity. f) Protrusion, intra-lick, and retraction phases of the trajectories from E are separately plotted. g) 3D trajectory of the highlighted lick shown in E-F.
- h-j) data plotted as in (e-g) for six tongue trajectories from ALM photoinactivated trials. Red X symbols denote the absence of ILMs.
- k) Speed versus time for the tongue trajectories shown in E, H. Blue, ALM inactivated.
- l-n) Median durations (l), Peak speeds (m) and Pathlengths (n) of lick phases with ALM intact (black) and ALM Inactivated (blue). (median \pm IQRs).

To test why ALM inactivations impaired tongue-spout contact we analyzed tongue kinematics during ALM-inactivated trials, first focusing on the ability of the cue to cause tongue protrusion. ALM inactivation reduced the probability of tongue protrusion, consistent with the idea that ALM sends movement initiation signals to brainstem circuits to initiate a cued lick bout (Goard et al., 2016; Komiyama et al., 2010; McElvain et al., 2018; Svoboda and Li, 2018). However, cue-evoked protrusions were mostly intact following ALM inactivation, even in cases where spout contact was not (Figure 3.2b, Movie S3)(Probability of protrusion, intact:1 [0.9968 1] vs inactivated: 0.58 [0.58 0.61], $p < 0.05$, $n = 9$ animals, Wilcoxon signed rank test). Tongue protrusions initiated during ALM inactivation exhibited similar latencies and peak speeds as control trials (Figure 3.2d,l-n, Table 3.2; Latency to protrusion, intact:103 [93 114] vs ALM inactivated:132 [122 140]; Protrusion peak speed, intact:195.45 mm/s [191.22 199.37] vs ALM inactivated:186.15 mm/s [181 191.54], $p > 0.05$, $n = 9$ animals, Wilcoxon signed rank test). Thus deficient lick initiation did not fully explain ALM inactivation-associated deficits in spout contact.

Why did cue-evoked licks during ALM inactivation fail to make spout contact even on trials when protrusion was normal? Cued licks initiated with ALM inactivated exhibited significantly shorter durations, reduced speeds, reduced pathlengths and fewer acceleration peaks (Figure 3.2, Table 3.2; Intact Duration, Acceleration peaks: 113ms [112 115], 6 [5 6]; ALM Inactivated: 53ms [51 58], 2 [2 3], $p < 0.05$ all comparisons, $n=9$ animals, Wilcoxon signed rank test). ALM photoinhibition also reduced trial-by-trial variability of lick kinematics (Methods)(Table 3.2). Critically, on ALM inactivated trials, mice failed to produce ILMs after protrusions and immediately retracted the tongue (Duration of ILM on missed spout contact, Intact: 50 ms [40 57] vs ALM Inactivated: 0ms [0 0], $p < 0.05$, $n = 9$ animals, Wilcoxon signed rank test). On rare cases where spout contact occurred during ALM photoinhibition, subsequent water

retrieval licks were not strongly affected by ongoing ALM inactivation (Supplemental Text, Table 3.4, and Figure 3.S7). Thus, with ALM inactivated, animals could usually generate cued licks but could not make within-lick adjustments that facilitate spout contact. Within-reach adjustments in primates also rely on cortical activity (Dickey et al., 2013; Georgopoulos et al., 1983; Rohrer et al., 2002).

We next trained mice to lick to left or right by differential placement of a single spout across distinct daily sessions. High success rates showed that cue-evoked licks could be directed towards remembered spout locations (Spout-Left, Probability of Success: 1 [1 1], Latency to Spout Contact: 213 ± 19 ms, $n=9$ animals; Spout-Right, Probability of Success: 1 [1 1], Latency to Spout Contact: 232 ± 22 ms, $n=7$ animals). Kinematic analyses of cue-evoked licks revealed that the tongue protrusions were significantly biased towards whichever spout location was rewarded in the session (Figure 3.3, Movie S4, Median Lateral Displacement: 0.55mm [0.50 0.60] (left), and -0.27[-0.15 -0.33] mm (right), $p < 0.05$ one sided t-test for all measures, $n = 9$ and 7 animals respectively).

To test if directionally biased tongue protrusion required cortex, we inactivated ALM or PMM after mice learned to lick at left or right spouts. Consistent with past work and with lick-straight conditions (Goard et al., 2016), inactivation of ALM, but not PMM, reduced cue-evoked spout contact (Probability of spout contact, spout left, intact: 1 [1 1] vs ALM inactivated: 0.57 [0.54 0.67]; Spout right, intact: 1 [1 1] vs ALM inactivated: 0.47 [0.3 0.66], $p < 0.05$, $n=9$ and 7 animals, Wilcoxon signed rank test). Kinematic analysis revealed, however, that tongue protrusions were still usually present during ALM photoinhibition (Probability of protrusion with ALM inactivation, left: 0.85 [0.53 0.86], right: 0.67 [0.54 0.81], $n=7$ and 9 animals, respectively, medians [IQRs]) and that protrusions remained significantly biased toward the remembered spout

location (Figure 3.3, Movie S5, Median Lateral Displacement (ALM inactivated): 0.49 ± 0.14 mm(left) $p < 0.05$, -0.21 ± 0.07 mm (right) $p < 0.05$, and 0.004 ± 0.07 mm (center) $p > 0.05$, $n = 9, 7$ and 9 animals respectively, one sided t-test for all measures). As with spout straight-conditions, ALM inactivated trials lacked the ILM component of the lick (Spout left, Duration of ILM, intact: 9ms [4 15] vs ALM inactivated: 0 [0 0]; Spout right, intact: 14ms [8 19] vs ALM inactivated: 3ms [0 7], $p < 0.05$, $n = 9$ and 7 animals respectively, Wilcoxon signed rank test), resulting in a failure to make online adjustments important for spout contact.

During reaching, primates use online proprioceptive feedback and estimates of target position to aim corrective submovements towards unseen targets (Ghez et al., 1995a; Meyer et al., 1988). To test if ILMs were random walk-like movements or if they were aimed in preferred directions, we examined the distribution of each ILM's initial velocity vector (Methods). In all mice and in all sessions, ILMs were strongly biased in specific directions (Figure 3.4a,d,g Insets, $p < 0.001$ chi-squared test for a uniform distribution. 12/12 animals)(Methods). This ILM directional bias could, in principle, be due to a further extension of the preceding protrusion or could be an aimed re-direction towards a target. Surprisingly, within sessions, the direction of each ILM's initial velocity vector was not correlated with the direction of the immediately preceding protrusion (linear regression of protrusion direction vs ILM direction, $p > 0.05$ for 12/12 animals, F-test)(Methods), suggesting that a new direction command was generated at the moment of protrusion offset. To test if this direction was biased towards remembered spout locations, we computed a direction bias, defined as the dot product between each ILM's initial velocity vector and the three vectors from ILM starting position to the three possible target locations (left, center, or right) (targets defined as the median tongue tip position at spout

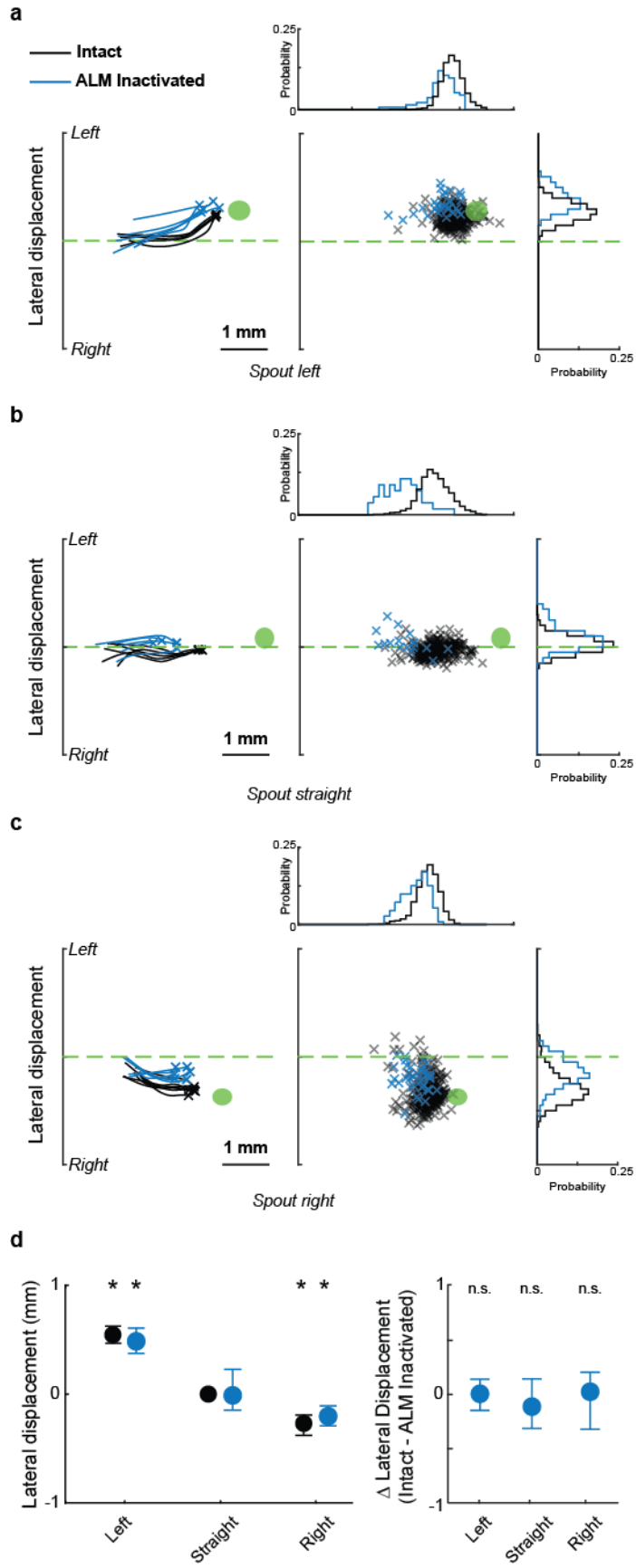


Figure. 3.3. Directionally biased tongue protrusions persist during ALM inactivation.

a) Left: Five example tongue protrusions (from bottom view) from a single session with the spout placed to the left (blue, ALM inactivated; black: ALM intact). Green ellipse denotes 95% CI of the tongue tip location at the moment of retraction onset. Center: Scatter plot of tongue tip positions at the end tongue protrusions. Probability distributions of the ALM intact (black) and inactivated (blue) dots are projected along the axes at top and right (bin size, 120um). Green line, midline.

b-c) Data plotted in A for sessions with centered (b) and right (c) spout placements.

d) Left: The lateral placement of the tongue tip at the moment of protrusion offset is plotted across left, straight, and right sessions (black: laser off; Blue: ALM Inactivated; data are median±IQR across n=9 animals). Right: The average difference in lateral displacement between ALM intact and ALM inactivated trials (median±IQR displacements across animals (n=7 mice)

contact)(Methods) (Supplemental Text, Figure 3.4b and Figure 3.S3D-F). Across mice and sessions, the ILMs' initial velocity vectors were significantly more biased towards the rewarded target location (Figure 3.4, Table 3.5), consistent with online aiming that may account for both current and target tongue position. Yet, importantly, ILMs were highly tortuous (ILM tortuosity: 1460 mm⁻³ [740 2378]; straight line tortuosity: 0)(Methods), suggesting that the consequence of ILM aiming was to bias a noisy and/or exploratory process.

ALM is implicated in both lick planning and execution(Goard et al., 2016; Komiyama et al., 2010; Svoboda and Li, 2018). In our task, which by design only focused on execution, we found that deficits during ALM inactivation were primarily attributable to an inability to produce within-lick adjustments, and, to a lesser extent, the inability to initiate a lick. These results predict that placing the spout very close to the mouth could rescue ALM inactivation-associated execution deficits. Experiments confirmed this prediction (Figure 3.S8, Probability of contact, spout Close: Intact: 1 [1 1] vs ALM inactivated: 0.93 [0.72 0.96] $p < 0.05$, $n = 9$ animals, Wilcoxon signed rank test), supporting the more general idea that motor cortical activity in mice is critical for online adjustments but not for cue-evoked movement initiation(Heindorf et al., 2018)

Discussion

High speed videography has repeatedly overturned assumptions of lingual control in bats, hummingbirds, chameleons and cats(de Groot and van Leeuwen, 2004; Harper et al., 2013; Reis et al., 2010; Rico-Guevara and Rubega, 2011). By combining kilohertz frame-rate imaging and deep learning based machine vision methods, we tracked the rodent tongue in 3D for the first time and discovered that licks cannot be explained by open loop central pattern generators that drive simple binary ballistic events. Instead, individual licks exhibit complex, variable

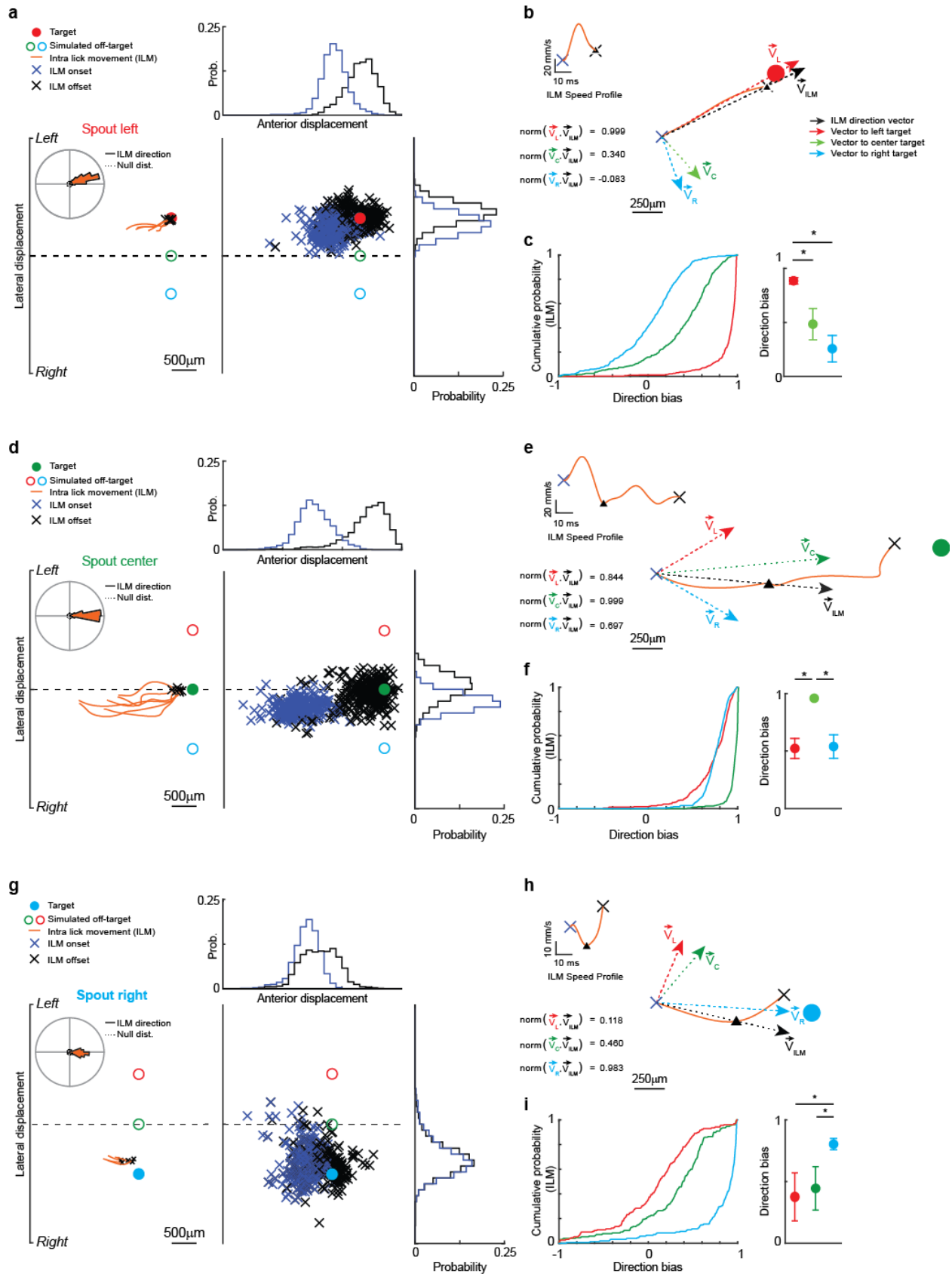


Figure. 3.4. Intra-lick movements are directionally biased towards remembered spout locations.

(a-c) ILM kinematics for spout-left sessions.

a) Left: Six representative ILMs. Inset: polar plot with direction distribution of all ILMs produced in a single spout-left session (center) and the null distribution of ILM directions. Middle: Scatter plot of tongue tip positions at protrusion offset (blue) and retraction onset (black), indicating ILM start and end points. Probability distributions of the ILM start- and end-points are projected along the axes at top and right (bin size, 120um).

b) Example of a single ILM path and its speed profile (orange). The ILM's initial direction (V_{ilm} , black dotted line) was computed from the vector connecting ILM starting point to its position at the first speed minimum (upward black triangle in speed and path plots). The dot products between this ILM direction vector and three additional vectors from ILM starting point to left, center, and right targets (dotted red, green, and blue lines, respectively) were computed to quantify the 'direction bias', the extent to which a given ILM was aimed at each of the three candidate targets.

c) Left: Cumulative distributions of directional biases for all ILMs produced in a single session to the three candidate targets (colored as in (b)). ILMs were reliably aimed to the left target.

Right: Directional biases of ILMs to left, center, and right targets spout-left sessions (median±IQRs across n=9, 9 and 7 animals respectively)

(d-f) ILM kinematics for spout-center sessions, plotted as in (a-c).

(g-i) ILM kinematics for spout-right sessions, plotted as in (a-c).

trajectories with limb-like dynamics, including the production of motor cortex-dependent online adjustments that facilitate target contact.

Precise aiming of the human tongue is necessary for coherent speech and can be leveraged for prosthetic control (Guenther, 1995; Kim et al., 2013). Our discovery of cortex-dependent corrections during licking establishes an experimentally tractable system for dissecting mechanisms of online motor control and reveals common principles underlying limb and lingual control.

Methods

Animals and Surgery

All experiments were carried out in accordance with NIH guidelines and were approved by the Cornell Institutional Animal Care and Use Committee. 12 VGAT-ChR2-EYFP (Jackson laboratory, JAX Stock #014548) animals of ages 32-52 weeks were individually housed under a 12hr light/dark cycle for the duration of the study, and were tested during the dark phase. On days when mice weren't being trained or tested, mice received 1 ml of water. Mice were trained and tested in experimental sessions that lasted 0.5h to 1h. If the mice did not receive at least 1ml of water during the behavioral session, their water was supplemented to meet the 1ml/day requirement.

Mice were deeply anesthetized with isoflurane (5%). Fur was trimmed, and mice were placed in a stereotaxic frame (Kopf Instruments, Tujunga, CA). A heating pad was used to prevent hypothermia. Isoflurane was delivered at 1-3% throughout surgery; this level was adjusted to maintain a constant surgical plane. Ophthalmic ointment was used to protect the eyes. Buprenorphine (0.05 mg/kg, subcutaneous) was given before the start of surgery. A mixture of

0.5% lidocaine and 0.25% bupivacaine (100 μ L) was injected subdermally along the incision line. The scalp was disinfected with betadine and alcohol. The scalp was then removed with surgical scissors to expose the skull, which was thoroughly cleaned, and four craniotomies were made over ALM (2.5 A/P \pm 1.5 M/L) and PMM (0.5 A/P \pm 1.5 M/L). 400 μ m optical fiber embedded in a 1.25 mm metal ferrule (Thor Labs) was then implanted bilaterally above these areas and held in place with a layer of Metabond (Parkell, Inc., Edgewood, NY). Mice were also implanted with a custom modified RIVETS (Osborne and Dudman, 2014) headplate for head restraint during the behavioral sessions. Another layer of Metabond was applied to firmly hold the implants in place, and the surrounding skin was sutured closed. Post-operative buprenorphine (0.05 mg/kg), carprofen (5 mg/kg), and lactated ringers (500 μ L) were administered subcutaneously.

Behavioral Setup

To simultaneously image two orthogonal planes of the mouse's orofacial movements, we placed a mirror (Thorlabs ME1S-P01 1") angled at 45 degrees below the mouse's mouth. We used a Phantom VEO 410L camera with a Nikon 105mm f/2.8D AF Micro-Nikkor lens to acquire videos with a resolution of 192x400 pixels at 1000 fps. Custom LabVIEW code for behavioral training was run on a training system built using a National Instruments sbRIO-9636 FPGA.

Behavioral Training

Five days after surgery and postoperative recovery, mice were started on water restriction. Mice were restricted to 1mL of water per day and their body weight was recorded daily. The behavioral training began after mice reached a steady state of body mass of 80% their original body weight with water restriction. Mice typically reached the steady state body weight in 5-6

days. In the first behavioral sessions, mice were head restrained and water (3 μ l) was delivered paired with an auditory cue (3.5 kHz). The spout was placed directly ahead of the mouse, approximately 1.6mm from the mouse's incisors. The auditory cues had an inter-trial interval with an exponential distribution, which provided a flat hazard rate such that the probability of a cue was not altered over the duration of the trial. After the mice learned to reliably lick the spout following the auditory cue, water delivery in subsequent sessions was made contingent on spout contact happening within 1.3 seconds of the auditory cue. Once the mice learned to initiate spout contact following an auditory cue to dispense water, we imposed a 1 second no spout contact window prior to the onset of the auditory cue. If the animal made spout contact within this window, the inter-trial interval was extended by an interval randomly drawn from the exponential distribution. This discouraged mice from spontaneously licking the spout and ensured that the licking we observed was in response to the auditory cue. Once the animals were trained, in separate sessions, ALM or PMM were bilaterally photoinhibited on 15% of the trials. After photoinhibition experiments were completed with the spout straight at 1.6mm, the spout location was moved to 3.2mm from the mouse's incisors. Once the mouse learned to lick the spout at 3.2mm, pseudorandom bilateral ALM or PMM inactivations were again performed. Once the animal learned to lick left or right, pseudorandom bilateral ALM or PMM inactivations were again performed.

Photoinhibition

We used laser LED light sources (LDFLS_450-450, Doric Life Sciences Ltd), attached to an optical rotary joint (FRJ_1 \times 2i_FC-2FC_0.22) and delivered light to the implanted cannulas

using 400 μ m, 0.43NA lightly armored metal jacket patch cords. The light sources were set to analog input mode and driven with a sinusoidal pulse (40 Hz, 10mW peak, 0.75s duration).

Artificial Deep Neural Network for Segmentation

We used an implementation of a semantic segmentation neural network (U-NET) to identify and segment the tongues from high speed videography. U-NET uses a contracting path that is thought to identify context, i.e. “is the tongue present in this image?”, and a symmetric expanding path that precisely localizes the relevant object, i.e. “where is the tongue present in the image?”

U-NET Architecture. The contracting path of the network was constructed as a series of 5 repeating modules. Each module was an application of two 3x3 convolutions, with each convolution followed by a ReLU and 2x2 max pooling operation with stride 2 for downsampling. At each downsampling, the number of feature channels was doubled. The number of channels for the first module was 2, and thus for the remaining modules they were 4, 8, 16 and 32 respectively. Dropout of 0.7 was added at the output of module 4 and 5. The expanding path of the network was symmetric to the contracting path, with 4 repeating modules. Each module had: First, a 3x3 convolution with half the number of channels from the previous module. Second, an upsampling step that doubled the frame size. Third, a concatenation step that merged the output of the current module with that of the symmetric module from the contracting path. And finally, two 3x3 convolutions, with each convolution followed by a ReLU. The last layer of the network was a 1x1 convolution layer that followed the last layer of the expanding path. This network had a sigmoid activation function and gave the probability of an individual pixel being a part of the tongue.

Network training. The network was trained on 3668 frames pseudo randomly selected from the dataset of 25,258,017 frames from all 12 animals across all sessions. The training set was balanced such that half of the 3668 frames contained visible portions of the tongue. The frames were then manually annotated with both the side view and the bottom view using a custom GUI. Separate networks were trained for the side and bottom views. The networks were trained with a batch size of 256 images, using the ‘adam’ optimizer and a binary cross entropy loss function. The networks were trained till the loss function reached an asymptotic value, of 0.0047 for the side view network and 0.0023 for the bottom view network, with a validation accuracy of 0.9979 and 0.9991 respectively. Both networks reached asymptotic performance within 4000 epochs.

Extracting 3D tongue kinematics

To obtain the full 3D kinematics of the tongue tip during a lick bout, we performed a visual hull reconstruction using two orthogonal views (bottom and right side) of the tongue filmed via high-speed videography. This hull reconstruction procedure is contingent upon crisp 2D silhouettes of the tongue from both the bottom and side views, which were obtained by U-NET segmentation. We next constructed a 3D voxel representation of the tongue by identifying voxels that map onto the tongue silhouette when projected back into the 2D image space. Intuitively, this can be thought of as placing the bottom and side view images on adjacent faces of a cube, projecting the silhouettes in towards the center of the cube, and identifying the 3D intersection of these projections (Figure 3.S1A). For trials in which the side view of the tongue tip is occluded by the lick spout, we estimate the shape of the occluded tongue region by fitting a cubic spline to the boundary of the side silhouette and extrapolating the boundary spline into the occluded region.

We obtained 3D coordinates of the tongue centroid by averaging, and then defined the tongue tip as the position on the tongue that is furthest from the centroid in the direction of the lick, which we located using a two-step search process (Figure 3.S1b). In the first step, we defined an initial search vector, which points forward (anterior) and down (ventral) from the tongue centroid. This initial search vector was used across all videos. Using this initial search vector, we identified voxels in the tongue hull that satisfied the search criteria of i) the vector connecting the voxel to the centroid made an angle of less than 45 degrees with the initial search vector and ii) the distance from the centroid to the voxel was $\geq 75\%$ of all voxel-to-centroid distances. We took the collection of voxels that satisfy these criteria, which we called candidate voxels, and calculated their mean location. The unit vector between the tongue centroid and the mean location of the candidate voxels was then used as the search vector for the second step of the search process, as it pointed in the rough direction of tongue tip. The second step of the search process followed a similar pattern to refine the search described above. Using the refined search vector from step one, we performed a search for voxels that were i) within a given angular range (15 degrees) of the search vector and ii) were located on the boundary of the tongue hull. The average location of this second set of candidate voxels was defined to be the tongue tip (Figure 3.S1C). The resultant 3D kinematics for the tongue tip were filtered using an 8 pole, 50 Hz low-pass filter.

Trajectory Analysis

Tongue volume was determined from the convex hull reconstruction from the segmented images (see “Extracting 3D tongue kinematics”). Tongue tip trajectories were segmented into three distinct phases on the basis of the rate of volume change of the tongue. The protrusion phase was defined as the time from when the tongue is detected up to the first minimum in the rate of volume

expansion of the tongue. The retraction phase was defined as the time from the last minima of the rate of volume expansion of the tongue until the tongue was back in the mouse's mouth. Movements between the end of protrusion and the onset of retraction were defined as intra-lick movements (ILM).

Instantaneous speed was calculated as a one-sample difference of the position vector and pathlength was calculated as the cumulative sum of the one-sample difference of the position vector over the entire trajectory. Acceleration was calculated as the one sample-difference of the instantaneous speed. Peaks were identified using the `findpeaks` function in MATLAB. Lateral displacement was defined as the distance of the tip position from the midline of the mouse. The midline of the mouse was defined as the line that passes through the point equidistant between the mice's nostrils and the midpoint of the mouse's incisors. Tortuosity was calculated as the integral of square of derivative of curvature, divided by the length of a curve. Intuitively, this formulation describes the degree to which the curvature of a trajectory changes relatively to its length. This formulation establishes that the tortuosity of a circle or a straight line is zero.

Direction bias was estimated as the dot product of the initial ILM direction vector and either the target direction vector or the simulated off-target direction vector. The ILM direction vector was defined as the direction vector from the location of the tongue tip at the onset of the ILM to the location of the tongue tip at the first speed minimum. The target direction vector was defined as the direction vector from the location of the tongue tip at the onset of the ILM to the median location of the tongue tip at retraction onset in that session. Similarly, the simulated off-target direction vector was defined as the direction vector from the location of the tongue tip at the onset of the ILM to the simulated target locations in that session.

Since targets were changed across sessions and not within sessions, and not all mice were trained in all directions, the simulated off-target direction vectors were defined as follows. For the left sessions: the center/straight simulated target had the same the A/P location and was on the midline. The right simulated target had the same A/P location as the target, and symmetrical M/L location from the midline. For example, if the left target was at +4mm A/P and +1.2mm M/L, the right simulated target would be at +4mm A/P -1.2mm M/L and the center straight target would be at +4mm A/P 0 M/L. For the right sessions: symmetrical to the left sessions. For the center sessions: Both the right and left simulated targets had the same A/P location, and M/L was $\pm 1.2\text{mm}$.

Statistical Analyses

For measures of central tendency, we used medians and interquartile ranges (IQR) since these measures do not assume normality of distributions. They are represented as medians [IQR]. For e.g. a duration measure of 18ms [16 22], represents a median of 18ms with interquartile range from 16ms to 22ms.

Statistical analyses were performed using standard tests in MATLAB, including one sided t-tests, two-sample t-tests and Wilcoxon signed-rank tests. Correlation was tested by applying the F-test statistic to a linear fit. A chi-squared goodness-of-fit test was performed to determine if a distribution was uniform.

Acknowledgements

We thank Joe Fetcho, Melissa Warden, Neville Hogan and members of the Goldberg lab for comments on the manuscript. We thank Bilal Bari for valuable advice on behavioral training, and Nikil Prasad and Jackson Walker for technical advice and support.

REFERENCES

- Beatus, T., Guckenheimer, J.M., and Cohen, I. (2015). Controlling roll perturbations in fruit flies. *J R Soc Interface* 12.
- Coddington, L.T., and Dudman, J.T. (2018). The timing of action determines reward prediction signals in identified midbrain dopamine neurons. *Nat Neurosci* 21, 1563-1573.
- Crochet, S., Lee, S.H., and Petersen, C.C.H. (2019). Neural Circuits for Goal-Directed Sensorimotor Transformations. *Trends Neurosci* 42, 66-77.
- de Groot, J.H., and van Leeuwen, J.L. (2004). Evidence for an elastic projection mechanism in the chameleon tongue. *Proceedings of the Royal Society of London Series B: Biological Sciences* 271, 761-770.
- Dickey, A.S., Amit, Y., and Hatsopoulos, N.G. (2013). Heterogeneous neural coding of corrective movements in motor cortex. *Front Neural Circuits* 7, 51.
- Faisal, A.A., Selen, L.P., and Wolpert, D.M. (2008). Noise in the nervous system. *Nat Rev Neurosci* 9, 292-303.
- Gaffield, M.A., and Christie, J.M. (2017). Movement rate is encoded and influenced by widespread, coherent activity of cerebellar molecular layer interneurons. *Journal of Neuroscience* 37, 4751-4765.
- Georgopoulos, A.P., Kalaska, J.F., Caminiti, R., and Massey, J.T. (1983). Interruption of motor cortical discharge subserving aimed arm movements. *Exp Brain Res* 49, 327-340.
- Ghez, C., Gordon, J., and Ghilardi, M.F. (1995a). Impairments of reaching movements in patients without proprioception. II. Effects of visual information on accuracy. *J Neurophysiol* 73, 361-372.
- Ghez, C., Gordon, J., Ghilardi, M.F., and Sainburg, R. (1995b). Contributions of Vision and Proprioception to Accuracy in Limb Movements. In "Contributions of Vision and Proprioception to Accuracy in Limb Movements," in *The cognitive neurosciences*, M.S. Gazzaniga, ed. (Cambridge, MA, US: The MIT Press), pp. 549-564.
- Goard, M.J., Pho, G.N., Woodson, J., and Sur, M. (2016). Distinct roles of visual, parietal, and frontal motor cortices in memory-guided sensorimotor decisions. *Elife* 5.
- Guenther, F.H. (1995). Speech sound acquisition, coarticulation, and rate effects in a neural network model of speech production. *Psychol Rev* 102, 594-621.
- Harper, C.J., Swartz, S.M., and Brainerd, E.L. (2013). Specialized bat tongue is a hemodynamic nectar mop. *Proceedings of the National Academy of Sciences* 110, 8852-8857.

- Heath, M., and Westwood, D.A. (2003). Can a visual representation support the online control of memory-dependent reaching? Evident from a variable spatial mapping paradigm. *Motor Control* 7, 346-361.
- Heindorf, M., Arber, S., and Keller, G.B. (2018). Mouse Motor Cortex Coordinates the Behavioral Response to Unpredicted Sensory Feedback. *Neuron* 99, 1040-1054 e1045.
- Khan, M.A., and Franks, I.M. (2003). Online versus offline processing of visual feedback in the production of component submovements. *J Mot Behav* 35, 285-295.
- Kier, W.M., and Smith, K.K. (1985). Tongues, tentacles and trunks: the biomechanics of movement in muscular-hydrostats. *Zoological journal of the Linnean Society* 83, 307-324.
- Kim, J., Park, H., Bruce, J., Sutton, E., Rowles, D., Pucci, D., Holbrook, J., Minocha, J., Nardone, B., West, D., *et al.* (2013). The tongue enables computer and wheelchair control for people with spinal cord injury. *Sci Transl Med* 5, 213ra166.
- Komiyama, T., Sato, T.R., O'Connor, D.H., Zhang, Y.X., Huber, D., Hooks, B.M., Gabbito, M., and Svoboda, K. (2010). Learning-related fine-scale specificity imaged in motor cortex circuits of behaving mice. *Nature* 464, 1182-1186.
- McElvain, L.E., Friedman, B., Karten, H.J., Svoboda, K., Wang, F., Deschênes, M., and Kleinfeld, D. (2018). Circuits in the rodent brainstem that control whisking in concert with other orofacial motor actions. *Neuroscience* 368, 152-170.
- McIntyre, J., Stratta, F., and Lacquaniti, F. (1997). Viewer-centered frame of reference for pointing to memorized targets in three-dimensional space. *J Neurophysiol* 78, 1601-1618.
- Meyer, D.E., Abrams, R.A., Kornblum, S., Wright, C.E., and Keith Smith, J. (1988). Optimality in human motor performance: ideal control of rapid aimed movements. *Psychological review* 95, 340.
- Osborne, J.E., and Dudman, J.T. (2014). RIVETS: a mechanical system for in vivo and in vitro electrophysiology and imaging. *PLoS One* 9, e89007.
- Reis, P.M., Jung, S., Aristoff, J.M., and Stocker, R. (2010). How cats lap: water uptake by *Felis catus*. *Science* 330, 1231-1234.
- Rico-Guevara, A., and Rubega, M.A. (2011). The hummingbird tongue is a fluid trap, not a capillary tube. *Proceedings of the National Academy of Sciences* 108, 9356-9360.
- Rohrer, B., Fasoli, S., Krebs, H.I., Hughes, R., Volpe, B., Frontera, W.R., Stein, J., and Hogan, N. (2002). Movement smoothness changes during stroke recovery. *J Neurosci* 22, 8297-8304.

Ronneberger, O., Fischer, P., and Brox, T. (2015). U-net: Convolutional networks for biomedical image segmentation. *International Conference on Medical image computing and computer-assisted intervention*, 234-241.

Spijkers, W.A., and Lochner, P. (1994). Partial visual feedback and spatial end-point accuracy of discrete aiming movements. *J Mot Behav* 26, 283-295.

Svoboda, K., and Li, N. (2018). Neural mechanisms of movement planning: motor cortex and beyond. *Current opinion in neurobiology* 49, 33-41.

Welsh, J.P., Lang, E.J., Sugihara, I., and Llinás, R. (1995). Dynamic organization of motor control within the olivocerebellar system. *Nature* 374, 453.

APPENDIX

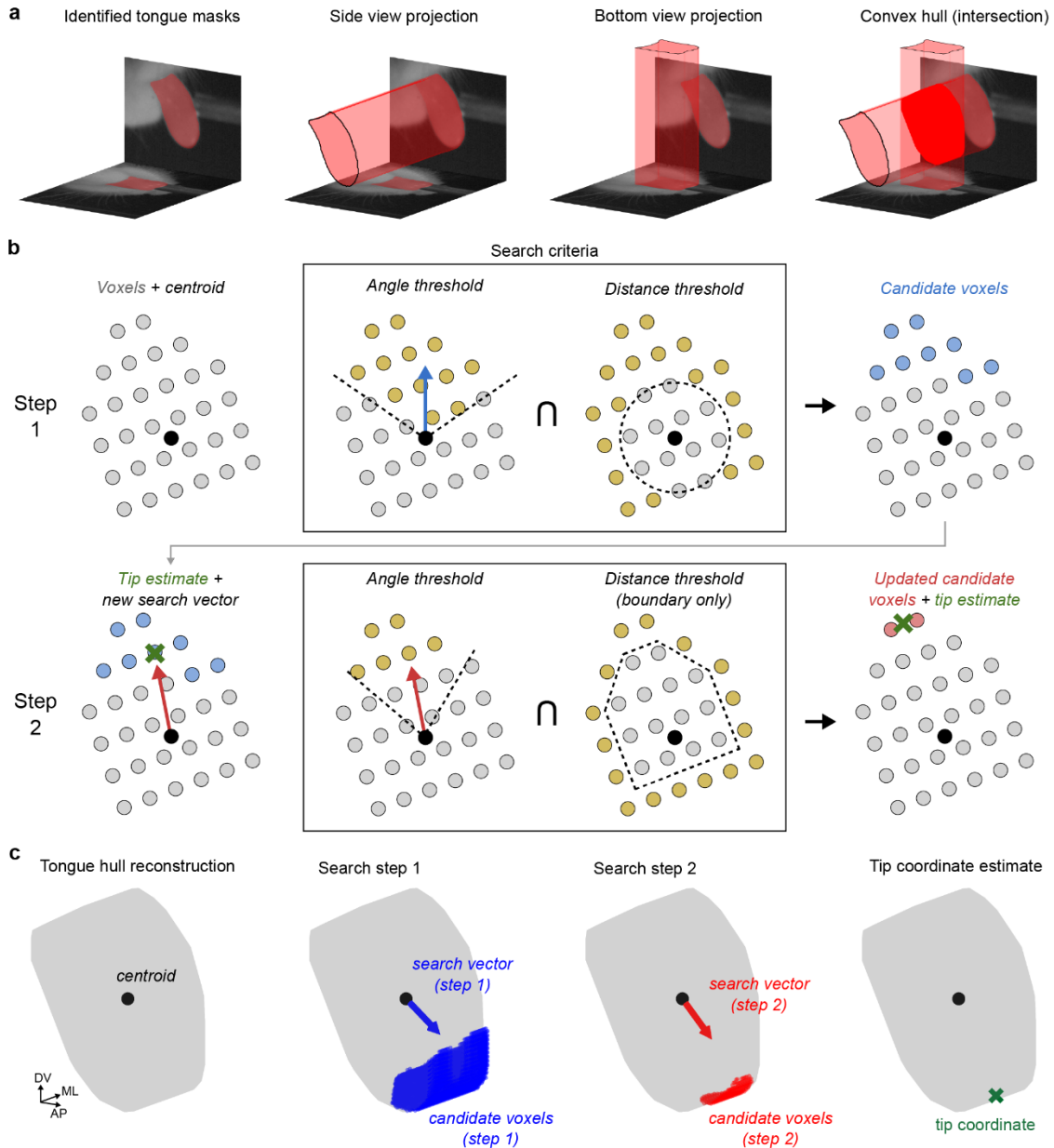


Figure 3.S1. Method for extracting 3D tongue tip kinematics.

(a) An example of the process used to generate a 3D voxel hull from the two views of the mouse tongue. The walls of the diagrams are stills taken from the high-speed video, with the segmented tongue mask highlighted in red. The final hull (rightmost diagram) is obtained by identifying the intersection of the projections of the side and bottom view tongue masks. (b) A 2D illustration of the tip coordinate search. With the voxels (gray circle) and centroid (black circle) identified, the first search step is performed, in which candidate voxels (blue) are found via the intersection of

voxels satisfying the two search criteria (yellow), namely thresholds on the maximum angle made with the search vector (blue arrow) and the minimum distance from the tongue centroid. These first candidate voxels are then used to generate a refined search vector (red arrow, second row) for the second step of the search. Using this refined search vector, a similar set of angle and distance thresholds are applied, to determine a refined set of candidate voxels, which are then averaged to determine the tip location. (c) Example of the tip search process with real data in 3D. The gray object is the 3D tongue hull, with the centroid labelled by a black circle. The first search step identifies a set of candidate voxels (blue) that are used to generate a refined search vector for the second search step (red). Using the second step candidate voxels, the tongue tip location is estimated (green 'x').

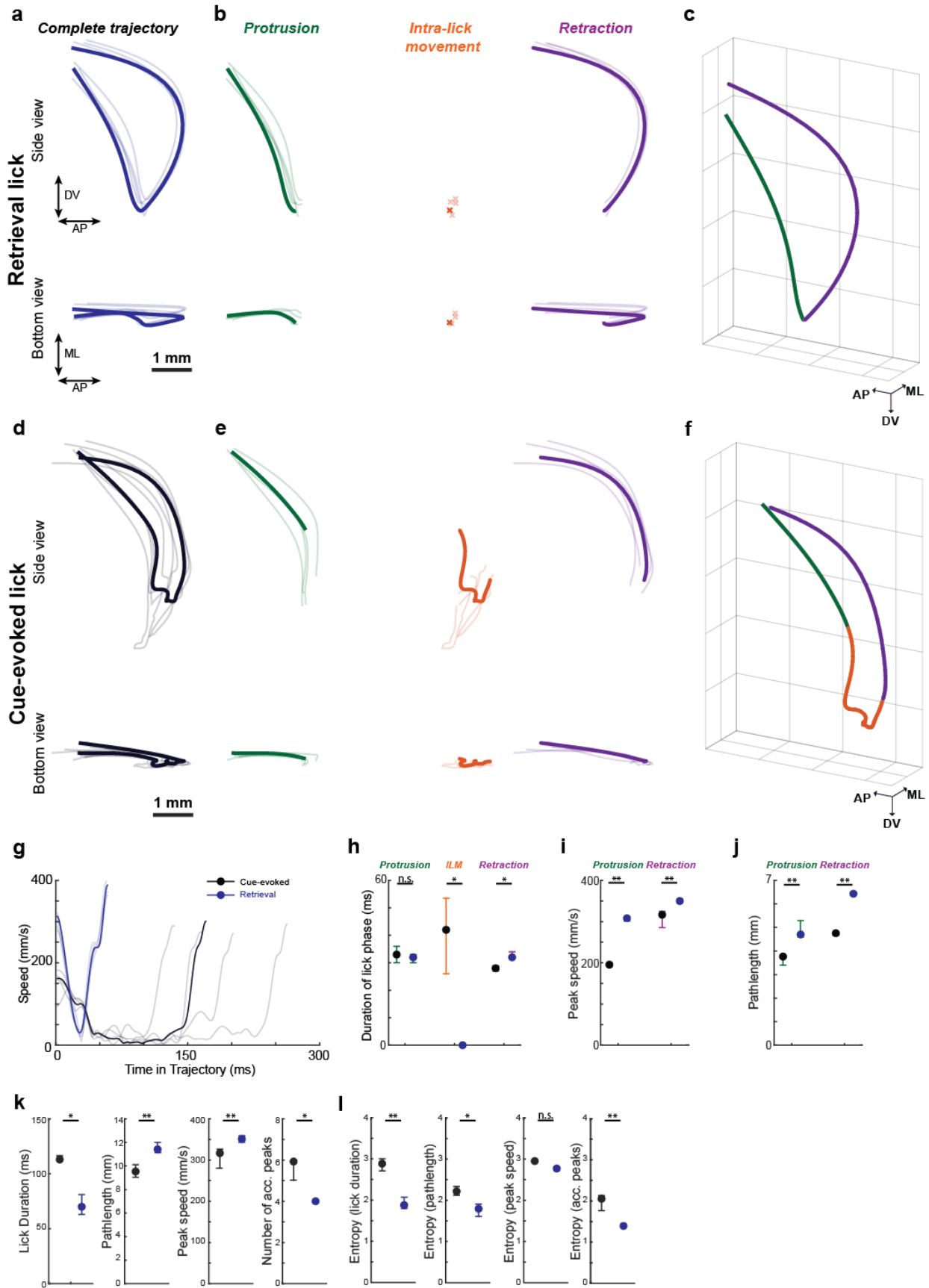


Figure 3.S2 Water retrieval and cue-evoked licks exhibit distinct kinematics

a-c) Water retrieval licks, defined as those initiated after spout contact.

a) Six overlaid tongue tip trajectories during retrieval licks. A single lick is bold for clarity. b) Protrusion, intra-lick, and retraction phases of the trajectories from (a) are separately plotted. Orange X symbols denote the absence of ILMs.

c) 3-D trajectory of the highlighted lick shown in A, with protrusion (green) and retraction (purple) lick phases indicated.

d-f) Data plotted as in (a-c) showing cue-evoked licks. Note the prominent ILMs.

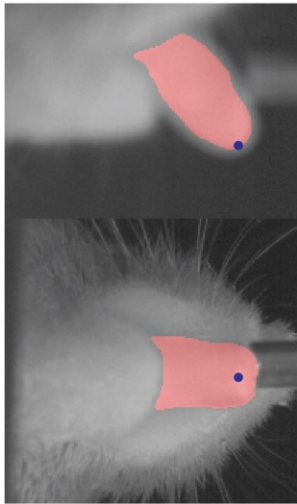
g) Speed versus time for the retrieval (blue) and cue-evoked (black) tongue trajectories shown in a,d.

h-j) Median durations (h), Peak speeds (i) and Pathlengths (j) of lick phases during cue-evoked (black) and retrieval (blue) licks. (Median \pm IQRs across 9 animals).

k-l) Kinematics (k) and entropy (l) of lick durations, pathlengths, peak speeds, and number of acceleration peaks (median \pm IQR across animals)

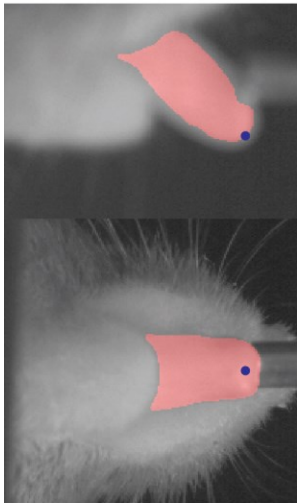
a

- Tongue tip at retraction onset

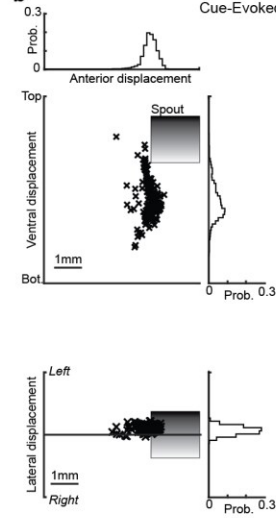


d

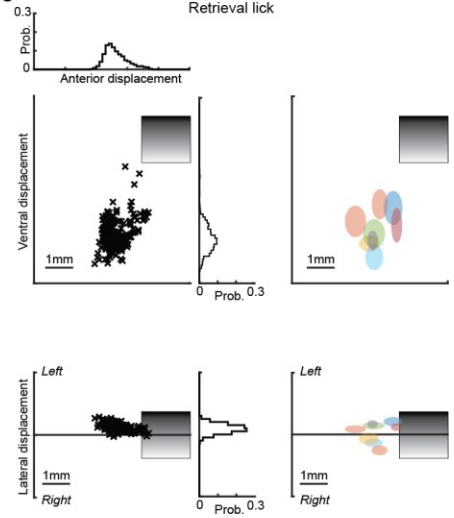
- Tongue tip at spout contact



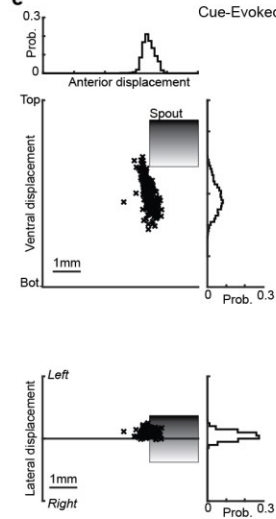
b Cue-Evoked lick



c Retrieval lick



e Cue-Evoked lick



f Retrieval lick

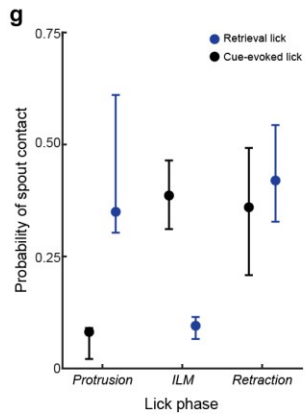
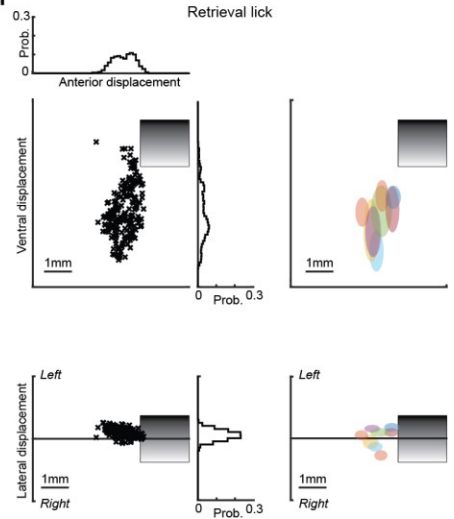


Figure 3.S3. Tongue tip positions at the moment of retraction onset and spout contact

- a) Side and bottom views of the tongue at the moment of retraction onset.
- b) Scatter plots of tongue tip positions at retraction onset for side (top) and bottom views (bottom) during successful cue-evoked licks. Note that for cue-evoked licks retraction onsets are identical positions as ILM offset. Probability distributions are projected along the axes at top and right (bin size, 120um). Right: 2D standard deviations of tongue tip positions at retraction onset for 9 mice (each mouse independently color-coded). Note that each mouse exhibits a ‘preferred’ target location for retraction onset.
- c) Data plotted as in (b) for retrieval licks.
- d-f) Data plotted as in (a-c) for tongue tip positions at the moment of spout contact
- g) Probability of spout contact as a function of the distinct lick phases for cue evoked and water retrieval licks (blue and black, respectively)

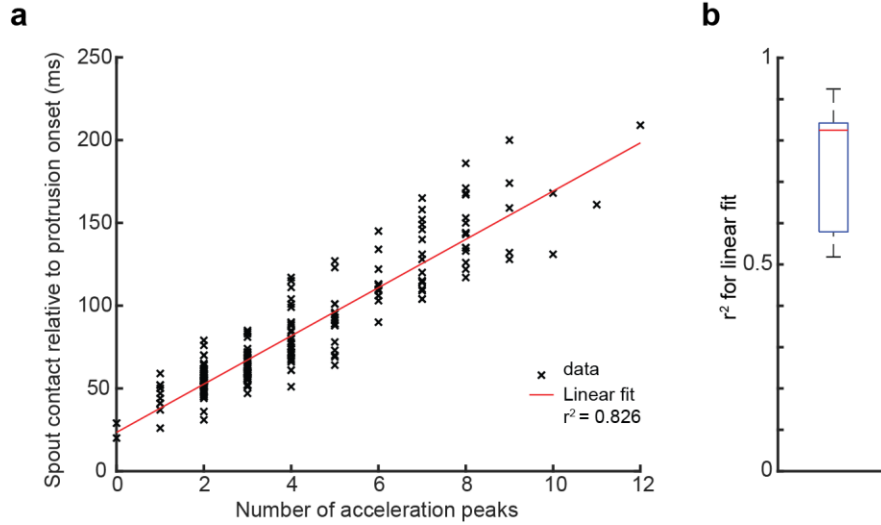


Figure 3.S4 . The number of acceleration peaks per lick predicts latency to spout contact

a) The latency to spout contact relative to protrusion onset is plotted against the number of acceleration peaks per lick from a single session. Red line, linear fit.

b) Boxplot showing r^2 for linear fits across 9 animals (red line: median; box edges: IQR; whiskers: 95% CI).

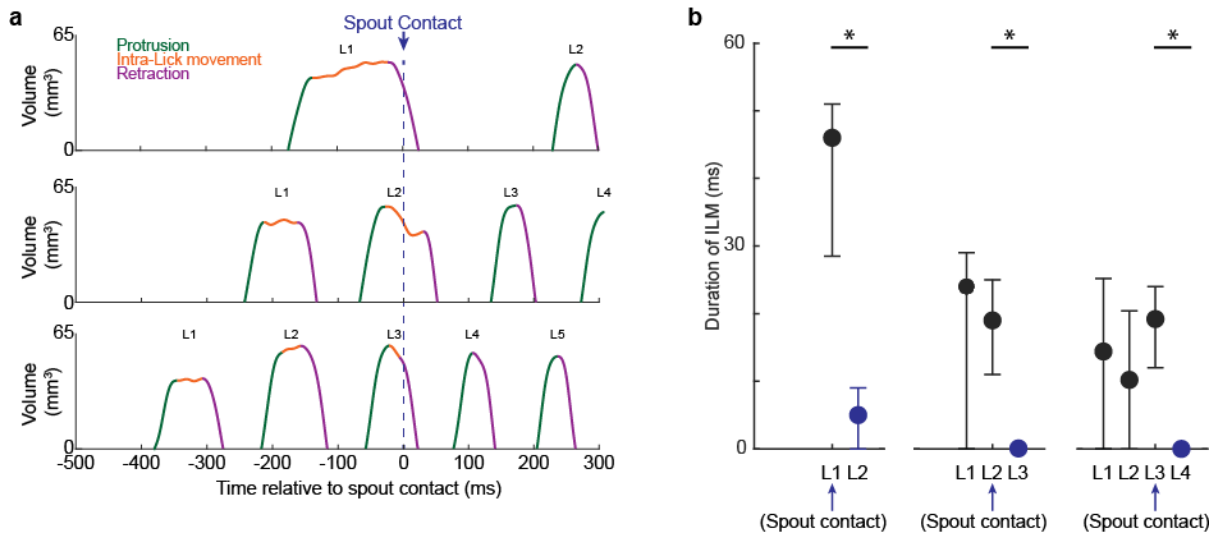


Figure 3.S5. Spout contact transforms the kinematics of subsequent licks.

a) Tongue volumes as a function of time during three trials where first spout contact occurred on the first, second, or third lick. Note that licks initiated before spout contact exhibited substantial ILMs, whereas those initiated after spout contact lacked ILMs.

b) Duration of the ILM lick phase as a function of lick number in cases where first spout contact happened on first, second, or third licks (median \pm IQR across animals $n=9$ (first), 9 (second) and 6 (third lick) animals). Spout contact reliably transformed the kinematics of subsequently initiated licks.

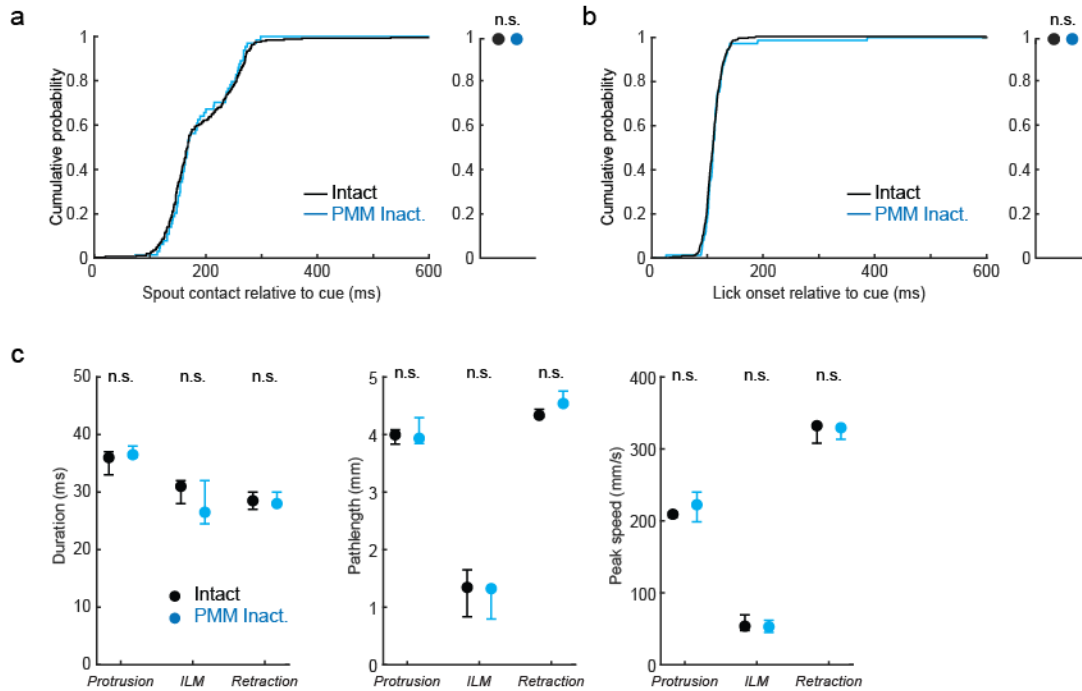


Figure 3.S6. Inactivation of PMM does not impact task performance or lick kinematics

a) Cumulative probability of tongue-spout contact relative to cue onset during laser-off and PMM-photoinactivated trials. Right, median \pm IQR probability of spout contact within a trial across mice (n = 9 mice).

b) Cumulative probability of lick protrusion onset relative to cue onset during laser-off and PMM-photoinactivated trials. Right, median \pm IQR probability of lick protrusion onset within a trial across mice (n = 9 mice).

c) Median durations, pathlengths, and peak speeds for all lick phases with PMM intact (black) and PMM inactivated (blue). (median \pm IQRs).

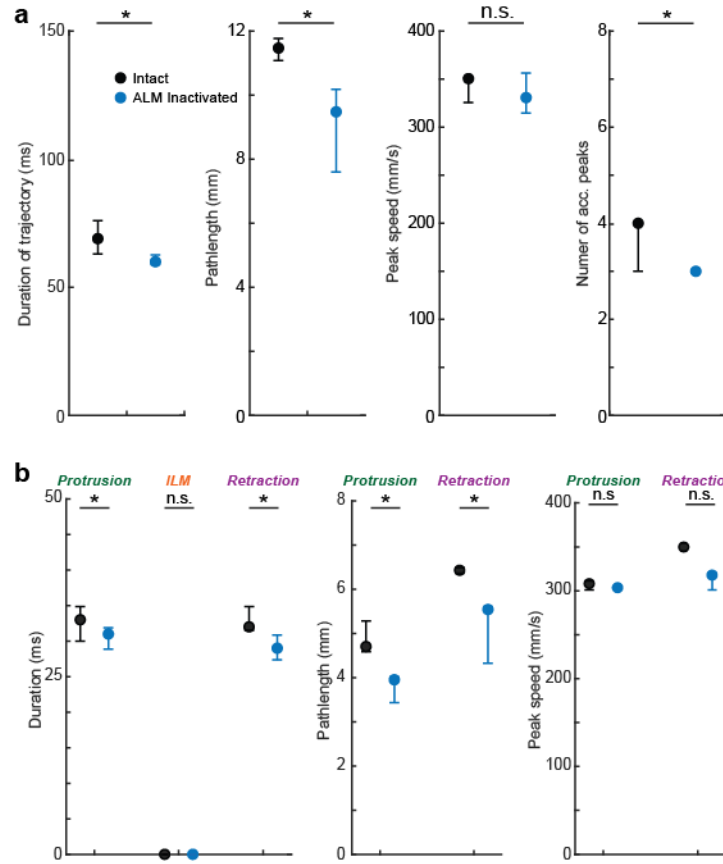


Figure 3.S7. ALM photoinhibition results in hypometric retrieval licks

a) Median durations, pathlengths, peak speeds and number of acceleration peaks during retrieval licks produced with ALM intact and inactivated (black and blue, respectively).

b) Median durations, pathlengths, and peak speeds for protrusion and retraction phases of retrieval licks with ALM intact (black) and ALM inactivated (blue). (median \pm IQRs). Note that these licks lacked ILMs ($n = 7$ animals)

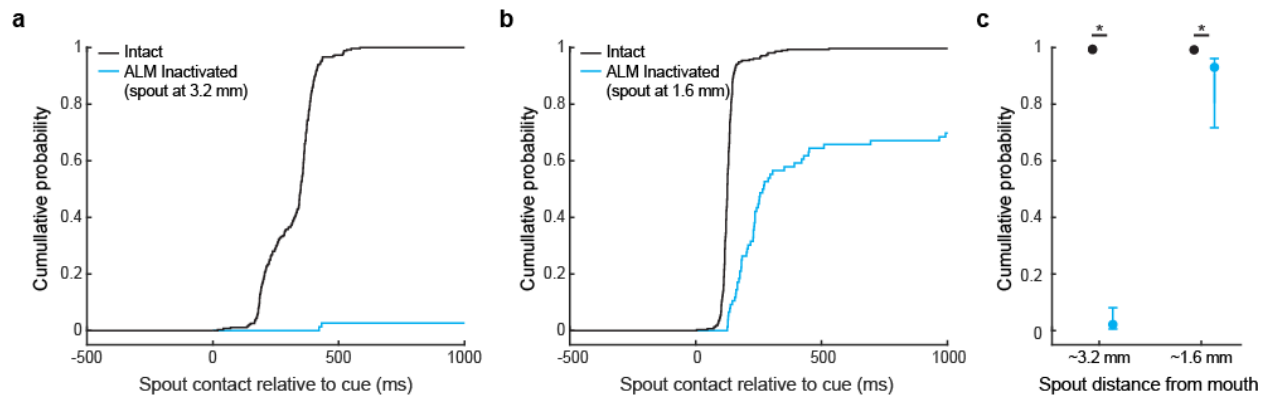


Figure 3.S8. Proximal spout placement rescues ALM inactivation-associated spout contact deficits

(a-b) Cumulative probability of spout contact relative to cue onset for ALM intact (black) and inactivated (blue) trials in sessions where the spout was 1.6 mm (a) and 3.2 mm (b) from the incisors. c) Median probability of spout contact across animals from spout-close and spout-far sessions.

Table 3.1. Kinematics of Cue Evoked and Water Retrieval Licks

Cue-evoked and water retrieval licks had distinct kinematics both at the complete trajectory level and when segmented into lick phases. * denotes a $p < 0.05$ for a Wilcoxon signed-rank test between cue-evoked and retrieval licks, $n = 9$ animals.

	Cue-Evoked Lick		Retrieval Lick	
	Median	IQR [25% 75%]	Median	IQR [25% 75%]
<i>Kinematics of complete lick trajectory</i>				
Acceleration peaks*	6	[5 6]	4	[4 4]
Duration* (s)	113	[112 115]	70	[69 76]
Peak Speed* (mm/s)	316.86	[276.40 317.28]	351.26	[350.49 353.90]
Pathlength* (mm)	9.53	[9.11 10.20]	11.41	[11.08 11.80]
<i>Entropy of complete lick trajectory</i>				
Acceleration peaks*	2.05	[1.54 2.19]	1.39	[1.28 1.52]
Duration*	2.88	[2.71 3.00]	1.88	[1.80 2.07]
Peak Speed	2.95	[2.93 2.98]	2.77	[2.76 2.81]
Pathlength*	2.22	[2.12 2.34]	1.80	[1.61 1.91]
<i>Kinematics by Lick Phase</i>				
Duration (ms)				
Protrusion	33	[30 36]	32	[30 33]
ILM*	42	[26 53.5]	0	[0 0]
Retraction*	28	[27 29]	32	[32 34]
Speed (mm/s)				
Protrusion*	195.45	[191.22 199.37]	308.12	[301.60 310.95]
Retraction*	316.61	[270.12 316.86]	349.86	[345.63 354.66]
Pathlength (mm)				
Protrusion*	3.77	[3.40 3.78]	4.70	[4.59 5.29]
Retraction*	4.76	[4.67 4.80]	6.43	[6.43 6.49]

Table 3.2. Kinematics of Cue Evoked Licks with ALM inactivation

ALM inactivation altered the kinematics of cue-evoked licks both at the complete trajectory level and when segmented into lick phases. * denotes a $p < 0.05$ for a Wilcoxon signed-rank test between cue-evoked and retrieval licks, $n = 9$ animals.

	Cue-Evoked Lick (Intact)		Cue-Evoked Lick (ALM Inactivated)	
	Median	IQR [25% 75%]	Median	IQR [25% 75%]
<i>Kinematics of complete lick trajectory</i>				
Acceleration peaks*	6	[5 6]	2	[2 3]
Duration* (ms)	113	[112 115]	51	[51 58]
Peak Speed (mm/s)	316.86	[257.10 329.98]	209.81	[209.81 301.67]
Pathlength* (mm)	9.53	[9.11 10.20]	5.99	[5.99 6.35]
<i>Entropy of complete lick trajectory</i>				
Acceleration peaks*	2.05	[1.54 2.16]	1.25	[1.12 1.59]
Duration*	2.88	[2.71 3.00]	1.94	[1.75 1.95]
Peak Speed	2.95	[2.85 3.04]	2.25	[1.60 2.58]
Pathlength*	2.22	[2.12 2.34]	2.71	[2.51 2.72]
<i>Kinematics by Lick Phase</i>				
Duration (ms)				
Protrusion*	33	[30 36]	23	[22 26]
ILM*	42	[26 53.50]	0	[0 0]
Retraction*	28	[27 29]	25	[24.5 26]
Speed (mm/s)				
Protrusion	195.45	[191.22 199.37]	191.54	[181.00 191.54]
Retraction*	316.61	[270.12 316.86]	250.81	[238.67 250.81]
Pathlength (mm)				
Protrusion*	3.77	[3.40 3.78]	2.74	[2.48 2.74]
Retraction*	4.76	[4.67 4.80]	3.24	[3.21 3.24]

Table 3.3. Kinematics of Cue Evoked Licks with PMM inactivation

PMM inactivation did not alter the kinematics of cue-evoked licks both at the complete trajectory level and when segmented into lick phases. * denotes a $p < 0.05$ for a Wilcoxon signed-rank test between cue-evoked and retrieval licks, $n = 9$ animals.

	Cue-Evoked Lick (Intact)		Cue-Evoked Lick (PMM Inactivated)	
	Median	IQR [25% 75%]	Median	IQR [25% 75%]
<i>Kinematics of complete lick trajectory</i>				
Acceleration peaks	5	[5 5]	6	[5 6]
Duration	98	[88 105.5]	91.50	[88.00 107.00]
Peak Speed	328.71	[309.43 332.95]	330.66	[314.07 334.24]
Pathlength	9.44	[9.15 9.60]	9.06	[9.03 10.11]
<i>Entropy of complete lick trajectory</i>				
Acceleration peaks	1.63	[1.44 1.86]	1.55	[1.46 1.90]
Duration*	2.41	[2.17 2.78]	2.26	[2.21 2.60]
Peak Speed*	3.13	[3.13 3.14]	2.76	[2.76 2.87]
Pathlength*	2.42	[2.37 2.58]	2.32	[2.04 2.41]
<i>Kinematics by Lick Phase</i>				
Duration (ms)				
Protrusion	36	[33 37]	36.5	[36 38]
ILM	31	[28 32]	26.5	[24.50 32]
Retraction	28.5	[27 30]	28	[28 30]
Peak Speed (mm/s)				
Protrusion	209.18	[204.81 211.98]	222.43	[198.60 240.12]
ILM	53.62	[47.45 69.40]	52.77	[44.91 61.80]
Retraction	332.29	[307.88 332.30]	329.47	[313.40 331.53]
Pathlength (mm)				
Protrusion	4.00	[3.83 4.08]	3.93	[3.84 4.29]
ILM	1.34	[0.83 1.65]	1.32	[0.79 1.35]
Retraction	4.33	[4.30 4.44]	4.54	[4.54 4.75]

Table 3.4. Kinematics of Retrieval Licks with ALM inactivation

ALM inactivation made the water-retrieval licks hypometric. * denotes a $p < 0.05$ for a Wilcoxon signed-rank test between cue-evoked and retrieval licks, $n = 9$ animals.

	Retrieval Lick (Intact)		Retrieval Lick (ALM Inactivated)	
	Median	IQR [25% 75%]	Median	IQR [25% 75%]
<i>Kinematics of complete lick trajectory</i>				
Acceleration peaks	4	[3 4]	3	[3 3]
Duration* (ms)	69	[63 76]	60	[59 62.0]
Peak Speed (mm/s)	350.54	[325.59 351.26]	330.76	[314.75 356.33]
Pathlength* (mm)	11.47	[11.08 11.77]	9.48	[7.60 10.18]
<i>Kinematics by Lick Phase</i>				
Duration (ms)				
Protrusion*	33	[30 35]	31	[29 32]
ILM	0	[0 0]	0	[0 0]
Retraction*	32	[32 35]	29	[27.50 31]
Peak Speed (mm/s)				
Protrusion	308.12	[301.60 310.95]	303.57	[303.57 303.57]
Retraction	349.86	[345.63 354.66]	317.87	[301.54 319.72]
Pathlength (mm)				
Protrusion*	4.70	[4.59 5.29]	3.95	[3.43 3.98]
Retraction*	6.43	[6.43 6.49]	5.54	[4.33 5.61]

CHAPTER 4

CONCLUSION

My dissertation research has focused on elucidating the neural circuits underlying the control of movement. I developed a suite of novel sensors, behavioral measurement platforms, and analytical tools for forelimb and tongue movements in mice to leverage the rapidly developing genetic toolkit for cell-type and projection specific neural perturbations and recordings (Gerfen et al., 2013).

To investigate the neural circuits underlying forelimb movements I developed a novel low-torque touch sensing joystick that can resolve a mouse forelimb kinematics with micron-millisecond spatiotemporal precision. I then integrated these joysticks in a computer controlled homecage system that can automatically train mice in closed loop to produce complex, directed center-out forelimb trajectories. The homecages were also modified to allow for behavior triggered optogenetics.

First, I trained mice to hold their forelimb still within a 2mm hold zone before reaching out to a spatial target. Holding still is not a passive behavior and often requires active control to maintain current limb position (Shadmehr, 2017). Given the joystick's compliance, holding still while applying a downward force created an inverted pendulum problem (Anderson, 1989; Bhounsule et al., 2015; Cabrera and Milton, 2002) for the mouse. Mice generated corrective micro movements (~20-100 μ m) while maintaining position. Stabilogram diffusion analysis of this movement suggested that mice used an active policy to maintain their position, similar to policies adopted by humans during upright standing (Peterka, 2002). Inactivation of contra lateral motor cortex did not alter the generation, direction or timing of these corrective movements for postural control. Inactivation of contra lateral motor cortex had a slight effect on reduced speed.

Second, after executing the ‘hold’, mice reached out in different directions. Contra lateral motor cortex inactivation reduced the peak trajectory speed and profoundly impacted the ability to reach out. At the trajectory level, neither reach direction nor variability were affected by cortical inactivation. At the primitive level, direction, tortuosity, acceleration patterns and probability of submovement overlap were also not significantly affected. Even primitive duration distributions, which provide proxies for the rate at which the CNS sends efferent movement initiation commands to the periphery, were not affected. These data provide convergent evidence for subcortical control of primitive generation and patterning in our task.

To determine if this observed reduction in gain due to loss of motor cortical drive was a general principle of the motor system I developed a second behavioral paradigm to investigate the neural mechanisms underlying precise lingual motor control. Using an artificial deep neural network called U-Net (Ronneberger et al., 2015) coupled with high speed videography (1 kHz) of the mouse tongue during a cued lick task (Gaffield and Christie, 2017) I was able to resolve the kinematics of lingual movements with decamicrosecond-millisecond spatiotemporal precision in 3D. Analysis of these kinematics revealed the presence of corrective movements as the tongue reached for the spout in response to a cue. Licks following the first spout contact were temporally stereotyped and on average did not contain corrective licks. Inactivation of a motor cortical area (ALM) led to specific deficits in these tongue kinematics, specifically eliminated the exploratory movements and reduced the amplitude of all other movements.

This combination of high precision forelimb and tongue kinematics with automated training, precise neural manipulation and recording presents a platform for the rapid dissection of the neural circuits and the identification of general principles underlying the neural control of movement.

An experimentally tractable paradigm for studying the neural control of movement across the entire motor control hierarchy.

The neural control of limb movements involves the coordination of neural circuits widely distributed across the brain and the spinal cord (Alstermark and Isa, 2012; Kiehn, 2016; Lemon, 2008). Accessing neural circuits in the spinal cord *in vivo* is challenging and when successful imposes strict biomechanical constraints on the limbs leading to severely constrained mechanics of movement. Studying the neural control of lingual kinematics has clear technical advantages. The neural circuitry involved in the production of lingual movements resides entirely in the brain (McElvain et al., 2018), enabling simultaneous access of the multiple neural circuits with modern silicon probes (Jun et al., 2017). With this platform, high density direct electrophysiological recordings from motor neurons can be performed while the effector is under measurement with decamicrosecond, millisecond scale precision during a skilled movement. To my knowledge, no other behavioral paradigm has this ability.

This technical advancement allows us to ask previously inaccessible questions about the biology of the control of movement in health and disease. There are at least three classes of questions that this paradigm can immediately shed light on, i) Description of the motor circuitry controlling the shape and configuration of the tongue. ii) Nature of the deficits in the neural firing patterns of the motor system due to movement disorders such as Parkinson's. And finally, (iii) mechanisms underlying the communication and interaction between brain regions.

Neural activity in the premotor neural circuits of the spinal cord, brainstem and the telencephalon during movement have received extensive attention. However, activity of the motor unit, consisting of the motor neuron and the muscle fibers it innervates, has been sparsely studied *in vivo* (Gorassini et al., 2000; Hoffer et al., 1987; O'Donovan et al., 1983). In these studies, the

motor neurons have been studied through inferring motor neuron firing patterns through single-unit electromyographic recordings with few simultaneously recordings. The study of the motor neurons in the vocal motor nuclei of vertebrates (Bass et al., 2008) provides extensive direct recordings but the behavior of the effector (i.e. the larynx, syrinx or the swim bladder) is inferred through the observed behavior (i.e. vocalizations). The neural activity in the vocal motor nuclei have been characterized due to their experimental accessibility, and the motor units have been recorded and studied in forelimb and the hindlimb because kinematics of the movements can be measured. Studying the neural control of lingual movements combines the advantages of these two approaches, the motor nucleus (nXII or hypoglossal nucleus) controlling the lingual movements is accessible to modern silicon probes and I have developed the infrastructure for precise measurement of the tongue movements, including its shape, as described in Chapter 3. With this paradigm we can now answer questions regarding the topography of motor neurons within the nucleus, the principles underlying their recruitment for types of movements (fast vs slow) (McLean et al., 2007) and how they are utilized for specifying the shape of the effector. The study of lingual kinematics is thus an excellent model for understanding the principles underlying the control of movement by motor neurons.

Movement disorders are characterized by abnormal kinematic signatures, such as a tremor (Parkinson's or Essential tremor), long lasting spasms (Dystonia) or rapid uncontrollable movements (such as Chorea). A combination of these kinematic signatures are used to identify and diagnose movement disorders. However, kinematics are inherently low dimensional, limiting the resolution of the phenotype of a movement disorder. The neural activity that leads to these abnormal movements is also insufficiently characterized. Direct recordings from motor and premotor neural circuits in an animal model for the movement disorder will provide insight into

the neural phenotypes associated with the loss of control. In addition to characterizing and comparing the atypical neural phenotypes to those in healthy animals (Goldberg et al., 2002), using genetic tools the role of the different neural populations in the generation/or modulation of this neural phenotype can be elaborated. Further, this phenotype can be used as a metric for the effectiveness of an intervention such as a novel drug.

A fundamental unsolved problem in the study of the nervous system is the mechanisms of communication and interaction between neural regions. The neural control of lingual movements provides a valuable model for these questions. Neural and genetic access to the motor neurons driving the muscles of the tongue (hypoglossal nucleus) gives us a direct measure for how neural activity is transformed to movement. Kinematic measurements paired with simultaneous neural recordings from the hypoglossal nucleus and the pre-motor structures that project to it will reveal the neural dynamics during skilled movement. Further, optogenetic perturbations can reveal the contribution of the pre-motor circuitry to the motor neurons. This process can be extended to enable the study and characterization of interactions between other brain areas such as the motor cortex and the medulla.

Control theoretic approach to understanding the neural computation underlying balance and posture.

In this thesis, I have assayed the effects of neural perturbation on lingual movements in the cued-lick task and forelimb movements in the hold and reach task. The focus has been on how the kinematic parameters (such as speed, acceleration, pathlength, direction and duration) are modified by this perturbation. This analysis, however, does not reveal the effects of neural perturbation on the control *policy*. A control policy goes beyond descriptions of individual kinematic parameters and provides a parsimonious mathematical framework for generation of movements. A control

policy accounts for both the temporal and spatial patterns of movements on a trial by trial basis. Determining the control policy for the movement under study requires an explicit knowledge of the specific goal the animal is trying to accomplish, making the modelling of even the simplest of reaching behaviors challenging (Scott, 2004).

The joystick forelimb paradigm can be leveraged to overcome the problems facing the modelling of behavior. With the joystick system Mice can be trained to ‘hold-still’, i.e. hold the joystick still within 400um for at least 400ms and the individual trajectories of mice forelimb movements during the ‘hold-still’ can be formulated as the control of an inverted pendulum, as in upright human standing (Peterka, 2002). Modelling a ‘hold-still’ behavior is simplified by assuming that the mouse is trying to hold the joystick still at the average of its trajectory, this assumption can be tested by measuring the average of the trajectory in discrete time bins. This analysis provides a trial-by-trial estimate of the control policy being employed by the mouse, and therefore can also be used to detect how this policy is affected by perturbation of different neural structures.

Fitting a control model to the observed joystick forelimb trajectory is not well constrained. A wide set of control parameters can be used to provide a good fit to the two dimensional data. To constrain the fitting process and identifying the relevant parameter regime requires identifying the transfer function of the system. The joystick design described in Chapter 2 cannot be perturbed or acted on in real time under experimenter control. The force experienced by the joystick relies on the distance to the base magnet, as demonstrated by the nearly linear force-distance profile (Figure 2.2E), this property can be exploited to provide experimenter controlled force/perturbations on the joystick. The joystick apparatus will have to be modified such that the position of the base magnet is no longer fixed, but is controllable on a millisecond timescale. This can be achieved by either

using a two axis platform or a pair of coupled linear drives (such as LM380 series from Faulhaber). The motion of the drives can be coupled to the joystick position, enabling real time control on the force on the joystick. A perturbation can then be generated with a short time scale, high amplitude modulation of the base magnet. In linear time invariant systems, the response to a single impulse is sufficient to determine the transfer function. Biological systems are unlikely to be as deterministic or linear, requiring a more sophisticated perturbation scheme (Peterka, 2002) that can estimate the transfer function on a non-linear stochastic system.

Studies of human standing with mechanical perturbations have estimated the control laws underlying the maintenance of posture, but they provide a limited understanding of how specific neural structures and circuits contribute to implementation of the control law. The genetic tools in mice, combined with a behavioral paradigm that is tractable for theoretical analysis provides an unprecedented opportunity to identify the neural circuits underlying the control of balance and posture.

A comparative approach to studying the neural control of movement

Neural perturbations of ALM during tongue movements and CFA during forelimb movements provide a comparative framework to identify general and effector specific principles for the cortical control of movement. Inactivation of motor cortex led to contracted movements in both lingual and forelimb movements, but to a loss of exploratory/corrective movements in tongue movements. These results establish that contraction of movements due to inactivation of motor cortex is a general principle across effectors and behavioral paradigms. These results are consistent with effects of motor cortical inactivations in Primates (Hoffman and Strick, 1995).

Inactivation of ALM during tongue movements, in the cued lick task, led to an additional deficit in generating exploratory and corrective movements. However, we cannot conclude that

this deficit was effector specific. In addition to the effector, the behavioral paradigms had substantial differences in the task structure. In the forelimb joystick paradigm the target was a direction not an endpoint, there was no somatosensory feedback on reaching the target, the task was not cued and the inactivations were performed after initiation of the movement.

To test if a lack of somatosensory feedback and a delay in inactivations during the planning phase of movements could explain the differences in the effects of cortical inactivation. The joystick task needs to be modified in the following ways to more closely match the cued-licking task. (i) The target is changed to an endpoint, this can be done by requiring the mouse to ‘hold’ in a target zone after performing a reach. (ii) Information about target acquisition is explicit i.e. there is a clear sensory feedback on reaching the target (either through an auditory cue, or a mechanical perturbation of the joystick), and (iii) introduce a cue and/or delay which provides a reference for the inactivations

REFERENCES

- Alstermark, B., and Isa, T. (2012). Circuits for Skilled Reaching and Grasping. *35*, 559-578.
- Anderson, C.W. (1989). Learning to control an inverted pendulum using neural networks. *IEEE Control Systems Magazine* 9, 31-37.
- Bass, A.H., Gilland, E.H., and Baker, R. (2008). Evolutionary origins for social vocalization in a vertebrate hindbrain-spinal compartment. *Science* 321, 417-421.
- Bhounsule, P.A., Ruina, A., and Stiesberg, G. (2015). Discrete-decision continuous-actuation control: balance of an inverted pendulum and pumping a pendulum swing. *Journal of Dynamic Systems, Measurement, and Control* 137, 051012.
- Cabrera, J.L., and Milton, J.G. (2002). On-off intermittency in a human balancing task. *Physical Review Letters* 89, 158702.
- Gaffield, M.A., and Christie, J.M. (2017). Movement rate is encoded and influenced by widespread, coherent activity of cerebellar molecular layer interneurons. *Journal of Neuroscience* 37, 4751-4765.
- Gerfen, C.R., Paletzki, R., and Heintz, N. (2013). GENSAT BAC cre-recombinase driver lines to study the functional organization of cerebral cortical and basal ganglia circuits. *Neuron* 80, 1368-1383.
- Goldberg, J.A., Boraud, T., Maraton, S., Haber, S.N., Vaadia, E., and Bergman, H. (2002). Enhanced Synchrony among Primary Motor Cortex Neurons in the 1-Methyl-4-Phenyl-1,2,3,6-Tetrahydropyridine Primate Model of Parkinson's Disease. *The Journal of Neuroscience* 22, 4639-4653.
- Gorassini, M., Eken, T., Bennett, D.J., Kiehn, O., and Hultborn, H. (2000). Activity of hindlimb motor units during locomotion in the conscious rat. *J Neurophysiol* 83, 2002-2011.
- Hoffer, J.A., Sugano, N., Loeb, G.E., Marks, W.B., O'Donovan, M.J., and Pratt, C.A. (1987). Cat hindlimb motoneurons during locomotion. II. Normal activity patterns. *J Neurophysiol* 57, 530-553.
- Hoffman, D.S., and Strick, P.L. (1995). Effects of a primary motor cortex lesion on step-tracking movements of the wrist. *J Neurophysiol* 73, 891-895.
- Jun, J.J., Steinmetz, N.A., Siegle, J.H., Denman, D.J., Bauza, M., Barbarits, B., Lee, A.K., Anastassiou, C.A., Andrei, A., Aydin, C., *et al.* (2017). Fully integrated silicon probes for high-density recording of neural activity. *Nature* 551, 232-236.
- Kiehn, O. (2016). Decoding the organization of spinal circuits that control locomotion. *Nat Rev Neurosci* 17, 224-238.

Lemon, R.N. (2008). Descending pathways in motor control. *Annu Rev Neurosci* 31, 195-218.

McElvain, L.E., Friedman, B., Karten, H.J., Svoboda, K., Wang, F., Deschênes, M., and Kleinfeld, D.J.N. (2018). Circuits in the rodent brainstem that control whisking in concert with other orofacial motor actions. *368*, 152-170.

McLean, D.L., Fan, J., Higashijima, S., Hale, M.E., and Fetcho, J.R. (2007). A topographic map of recruitment in spinal cord. *Nature* 446, 71-75.

O'Donovan, M.J., Hoffer, J.A., and Loeb, G.E. (1983). Physiological characterization of motor unit properties in intact cats. *J Neurosci Methods* 7, 137-149.

Peterka, R. (2002). Sensorimotor integration in human postural control. *Journal of neurophysiology* 88, 1097-1118.

Ronneberger, O., Fischer, P., and Brox, T. (2015). U-net: Convolutional networks for biomedical image segmentation. *International Conference on Medical image computing and computer-assisted intervention*, 234-241.

Scott, S.H. (2004). Optimal feedback control and the neural basis of volitional motor control. *Nat Rev Neurosci* 5, 532-546.